GRADUATE SCHOOL OF URBAN INNOVATION
YOKOHAMA NATIONAL UNIVERSITY

NUMERICAL SIMULATION AND ANALYSIS OF MECHANISMS AND FLUID DYNAMICS DRIVING MIXING AND SALT FLUXES IN COUPLED BRACKISH LAKES

By
MUCHEBVE EDWIN

A dissertation submitted in partial fulfilment of the requirements for the degree of

DOCTOR OF ENGINEERING

Academic Advisor
Professor Yoshiyuki Nakamura

March, 2017

In presenting this thesis in partial fulfillment of the requirements for an advanced degree at Yokohama National University I agree that the Library shall make it freely available for inspection. I further agree that permission for extensive copying of this thesis for scholarly purposes may be granted by my professor, or, in his absence, by the Director of Libraries. It is understood that any copying or publication of this thesis for financial gain shall not be allowed without my written permission.

DEDICATION

This thesis work is dedicated to my wife, Mary; daughter, Tinatsirei and son, Manatsu who have been a constant source of support and encouragement during the challenges of graduate school and life. I am truly thankful for having them in my life. This work is also dedicated to my parents, brothers and sisters, who have always loved me unconditionally and whose good examples have taught me to work hard for the things that I aspire to achieve.

ACKNOWLEDGEMENTS

I would like to express my sincere gratitude and appreciation to Professor Yoshiyuki Nakamura for his encouragement, guidance, and help through the doctorate studies, and particularly during the preparation and development of this research. The substantial patience and comments provided by Professor Nakamura on the dissertation are greatly appreciated.

I also would like to thank Professor Takayuki Suzuki for his support and teachings during my academic study.

I would like to thank the rest of the committee members, Professor Tatsuya Tsubaki, Professor Kimitoshi Hayano and Professor Hiroshi Katsuchi. I am indebted to Dr. Tetsunori Inoue (Port and Aiport Research Institute – PARI) and Dr. Yoji Tanaka (Tokyo City University) for making the STOC-LT (Ise Bay Simulator) code available and for providing the field observations data. I would also like to thank Dr. Hiroshi Kamiya of Shimane Prefectural Institute of Public Health and Environmental Science for providing data that was used in the research. I am also thankful to Dr. Hiroto Higa for his help with my research.

I also appreciate the help of the members of Estuarine and Coastal Engineering Lab: comments during lab seminars, help with Japanese and research

I also would like to thank my family; Mary Macheza, Tinatsirei and Manatsu for motivating me during the pursuit of my doctoral degree.

Endless thanks are extended to all my family and friends for their constant encouragement, support, and advice through my life. And most important, I thank God for giving me perseverance to achieve the fulfilment of my research.

Finally, financial support for my doctoral studies was provided by the Japanese Government (Monbukagakusho: MEXT) Scholarship (文部科学省奨学金).

DECLARATION

The version of section 2 has been presented at a conference and section 3 has been published in a journal.

1. Muchebve, E., Nakamura, Y., Suzuki, T., & Kamiya, H. (2016). Mechanisms Driving Water Exchange Processes and Circulation in Sakai Channel, Japan. In *The 12th International Symposium on Southeast Asian Water Environment (SEAWE12)* (pp. 88–95). Hanoi, Vietnam.
2. Muchebve, E., Nakamura, Y., Suzuki, T., & Kamiya, H. (2016). Analysis of the dynamic characteristics of seawater intrusion using partial wavelet coherence: a case study at Nakaura Watergate, Japan. *Stochastic Environmental Research and Risk Assessment*, *30*(8), 2143–2154. http://doi.org/10.1007/s00477-016-1336-1

ABSTRACT

Strong fluctuations in salinity levels in excess of the optimum values for bivalve *Corbicula japonica* habitat mainly during the summer period in coupled brackish lakes, Lake Shinji and Nakaumi. Water quality deterioration is evident during the summer period (salinity stratification, deepening of eutrophication, hypoxia, contamination). Unstable ecosystem dynamics, environmental state, productivity, especially clam *Corbicula japonica* farming. Understanding the variation of salinity is important for the maintenance of ecological health, and management of economy and society development in coastal regions. The dynamics of saltwater intrusion and mixing processes are not well understood. The study attempted to define the exchange and circulation processes, compute the salt flux at Nakaura Watergate and sections in the lakes, and eventually estimate the relative importance of the processes contributing to the salt balance. The study reveals, among other things, that river discharge, wind and atmospheric pressure are all important forcing mechanisms for circulation in Lakes Shinji and Nakaumi. River discharges of at least 100 m^3/s have a positive impact on outward flux of salt at Nakaura but promotes influx into Lake Shinji. Westerly winds of at least 5 m/s and pressure drop of about 10 hPa promotes overall influx of salt. Generally, the peaks of river flow, wind and atm. pressure coincide with each other and wavelet analysis can be used to determine the most significant forcing mechanism at any given time.

TABLE OF CONTENTS

TABLE OF FIGURES

LIST OF TABLES

1 INTRODUCTION

1.1 LAKES SHINJI AND NAKAUMI

1.1.1 Location and physical properties of the study area

Lakes Shinji and Nakaumi are coupled brackish lakes on the Japan Sea coast of Japan with surface areas of 79.2 km^2 and 97.7 km^2 respectively, Figure 1.1. Ohashi River (7.7km long) connects Lake Shinji to Lake Nakaumi which is connected with Japan Sea by the Sakai Channel (7.5km long). Fresh water is supplied from the Hii River on the west end of Lake Shinji. Saltwater is supplied through Sakai Channel on the eastern side of Lake Nakaumi and flows along the bottom of the lake to the mouth of R. Ohashi forming the hypolimnetic layer. The saltwater also intrudes into Lake Shinji and brackish water from Ohashi River flows into Lake Nakaumi forming the surface layer. As a result, Lake Shinji is a mesohaline lake with average salinity between 1 and 6 psu. Lake Nakaumi has a strongly differentiated two-layer system, salinity of the surface water is 14-20 psu and that of the bottom layer is 25-30 psu. Hence, these brackish lakes are stably stratified due to salinity (density) differences and density gradients have a large impact on water movement in this system (Okuda 2004).

1.1.2 Biochemical processes in the lakes

Lake Shinji and Lake Nakaumi were affected by the loss of seagrass (e.g. Zostera marina L.) and this resulted in the shifting chief primary producers from benthic macrophytes to phytoplankton (Yamamuro et al. 2006). Benthic fish and crustacean population decreased, however this led to the increase in bivalve population in the lakes.

The depletion of dissolved oxygen and subsequent release of sulphide is suspected to induce a sudden mortality of eelgrass and other seagrass species (Hiratsuka et al. 2007).

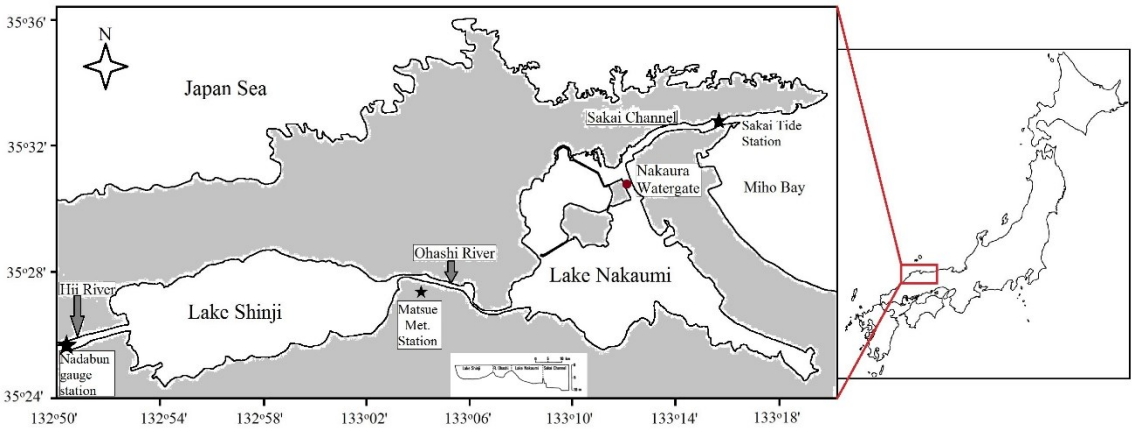

Figure 1.1 Map of the study area

Both Lakes Shinji and Nakaumi are densely populated by benthic filter-feeding bivalves; *Corbicula Japonica* (commercial fishery – *Shijimi*) and *Musculista Senhousia* (non-commercial fishery) respectively. The bivalves remove organic particulate matter and nutrients from the lakes, thereby controlling phytoplankton and detritus (Nakamura & Kerciku 2000; Nakata et al. 2000). The critical physiochemical factors necessary for successful establishment of bivalves in a water body are: salinity level, dissolved oxygen level, total sulphide, water velocity, mud content, water temperature, chlorinity level, pH level, and substrate availability (Yamamuro et al. 1990; Baba et al. 1999). *Musculista Senhousia* population in Lake Nakaumi recover quickly at the end of anoxia since they breed almost all year round (Yamamuro et al. 2006). Other shellfish e.g. cockles could not adapt to periodic anoxia experienced in the lake. Hydrogen sulphide (H_2S) released as a result of the depletion of dissolved oxygen (DO) from bottom waters is toxic to fish, crabs, oysters, shellfish and other aquatic life.

1.1.3 Saltwater intrusion into the lagoon system

The average water transport direction is from Lake Shinji to Lake Nakaumi, however, a reverse transport phenomenon often occurs a few days to a week. This phenomenon leads to high-salinity water mass intrusion upstream into Lake Shinji as sea surface level rise, except when episodic high fresh water discharge events occurred.

This is caused by meteorologically induced sea level variation which raise the water level in Lake Nakaumi (Nakata et al. 2000). High salinity in the bottom layer of Lake Nakaumi indicates seawater intrusion along the bottom into the lake and the very low surface layer salinity indicates a large amount of fresh water passing through the lake. The observed high salinity levels in Ohashi River coincided with the westerly wind maxima. The westerly wind forced the surface water current to the east in the surface, forcing a westward current in the bottom layer. This suggests that the wind-induced current is a possible mechanism for transportation of high salinity water from the open ocean into the bottom layer of the lagoon system (Nakata et al. 2000; Mizoyama et al. 2011).

High-salinity water mass entering Lake Shinji from Ohashi River form a fine salinity stratification in bottom of the lake (Mizoyama et al. 2011). The high salinity water intruding Ohashi River flows along a channel route at Lake Shinji junction and plunges into the bottom of the lake when it goes beyond the mound located in the entrance of Lake Shinji, and forms a layer (density stratification) maintaining high salinity without mixing. Layer forming the high salinity water moves slowly toward the centre of Lake Shinji on the smooth lake bottom topography as density current (Figure 1.2).

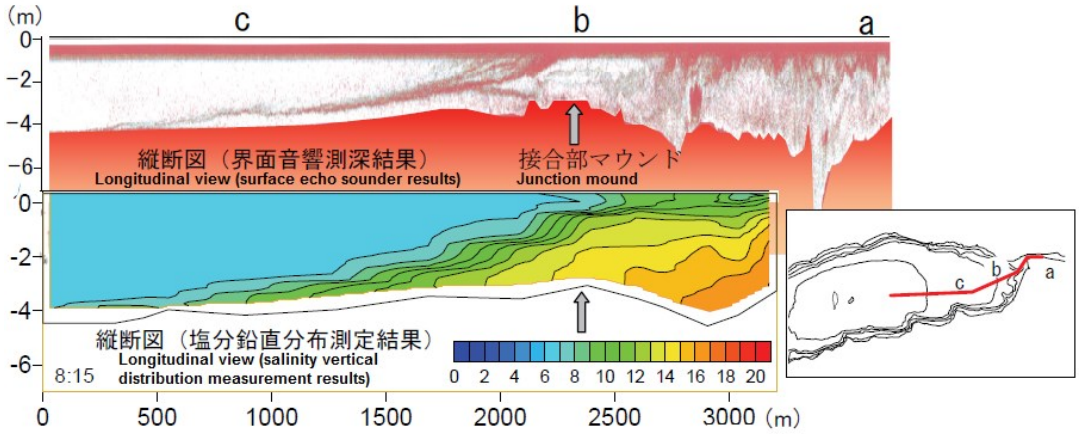

Figure 1.2 Observations of high-salinity water mass that has entered the Lake Shinji beyond the junction mound (2002.8.22) (Mizoyama et al. 2011)

High-salinity water observed in the bottom layer (+30 cm from the bottom of the lake) at the Central Observatory of Lake Shinji, disappear from the bottom layer at the centre of the lake when disturbed by the wind of above 10m/s. It was also revealed that at Shinji Lake mid-lake station, sometimes high-salinity water is stagnant in the bottom layer (Mizoyama et al. 2011). At the centre of the lake, high salinities of about 15psu are observed between late November and early December as a result of high-salinity water that entered from Ohashi River. After this, salinity of the bottom layer fell gradually to nearly 5 psu.

Looking at the change in the shape of the salinity stratification, formed in the bottom of Lake Shinji, high-salinity water mass of salt approximately 15psu was observed around the middle of the lake on early December, and after 3 days, it was observed closer to the west coast (Figure 1.3). In addition, the salinity near the centre of the lake dropped to 5psu, along with the movement of high-salinity water mass. Mizoyama et al., 2011 observed that the salinity stratification in Lake Shinji is unstable and disappears in the presence of 10m/s wind. Under the influence of the wind force less than 10m/s, the lake

bottom plain of Lake Shinji moves whilst maintaining stratification. However, the migration of high-salinity water mass to shallow water less than 4m deep was not observed. Even with limited amount of high-salinity water entering from Ohashi River, disturbance in the bottom of the lake is unlikely to occur due to its smooth lake bottom topography, hence salinity stratification is maintained (Mizoyama et al. 2011).

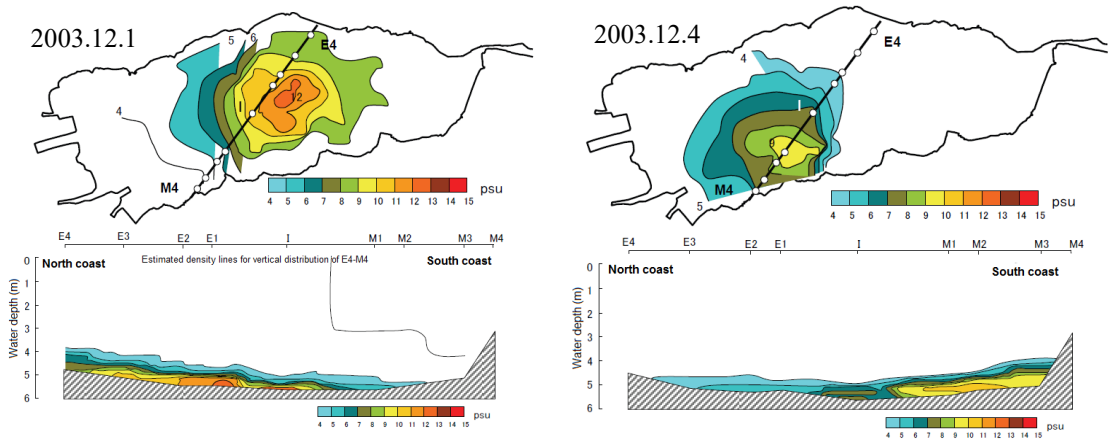

Figure 1.3 Observation of salinity stratification in Lake Shinji (Mizoyama et al. 2011)

1.1.4 Dissolved oxygen depletion in the lakes

Density stratification results in the formation of oxygen-depleted water in the bottom layer during summer. Salinity stratification of the lake bottom, as well as the associated changes in the salinity of the entire Lake Shinji water, inhibits oxygen supply, leading to poor oxygenation in the bottom layer, below the stratification. It is, therefore, important to consider the dynamics of saltwater intrusion in this water environment.

Yamamuro et al, 2011, the observed that the August 2005 dissolved oxygen in the bottom layer generally decreases, however there are some dissolved oxygen increases suggesting oxygen supply to the stratified bottom by wind despite the inflow of high salt water. The also observed high-salinity water at the centre of Lake Shinji, at water depth

greater than 4m, and anoxic water at water depth greater than 5m (Yamamuro et al. 2011). It has been observed that, sometimes the concentration of dissolved oxygen in the bottom layer was not below 2*mg/l*, despite significant high salinity water intrusion. On other occasions, the dissolved oxygen it will be below 2*mg/l,* in response to high salinity water intrusion. A possible reason for the fluctuation of the dissolved oxygen in the bottom layer, could be the relocation of the water mass (stratified/mixed) as a result of wind action (Yamamuro et al. 2011).

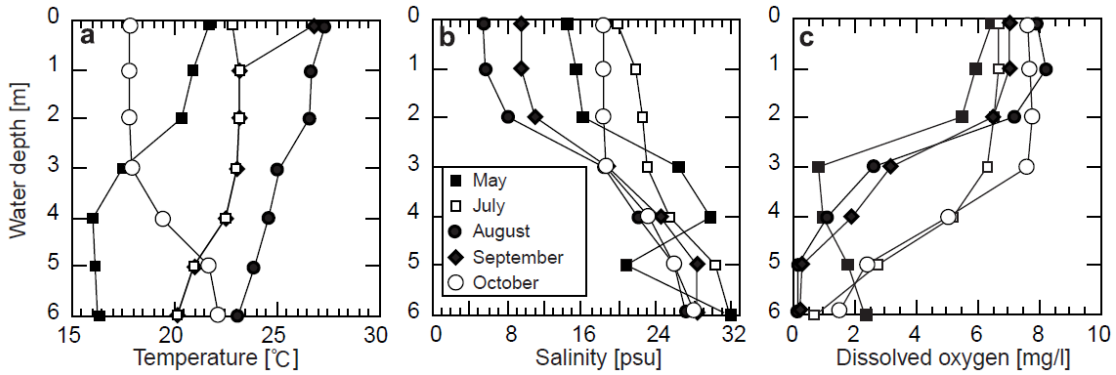

Figure 1.4 Vertical distribution of water temperature, salinity and dissolved oxygen in the southern part of Lake Nakaumi, May to October 2003 (Sakai et al. 2004)

The hypolimnion of Lake Nakaumi becomes anoxic from April to October across most of the lake. A rapid decline in DO concentration in the bottom water is observed starting April and becomes close to anoxic in early May (Figure 1.4). Previous study by Nakata et al, 2000 shows the appearance of oxygen-depleted water at the east end of Lake Nakaumi in late April which extended to the central part of the lake and then further northward with time (Figure 1.5). In Lake Shinji, the same data shows the formation of oxygen-depleted water in the south-western part of the lake in July (Nakata et al. 2000).

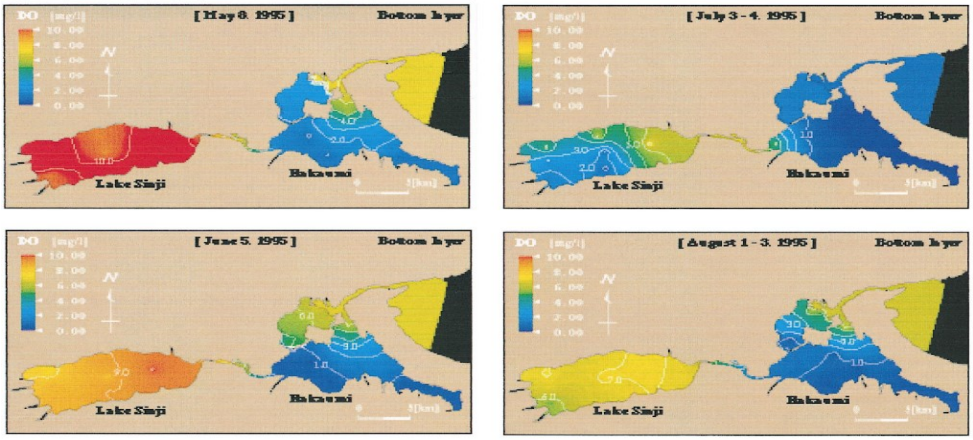

Figure 1.5 The appearance of oxygen-depleted water in Lakes Shinji and Nakaumi (Nakata et al. 2000)

1.2 BIVALVE *CORBICULA JAPONICA* FISHERIES IN LAKE SHINJI AND THE IMPACTS OF SALINITY

The brackish water bivalve *Corbicula japonica* is an important commercial species in Japan. It is found throughout the country and the major fisheries grounds in the Shimane Prefecture are located in Lake Shinji. More than 90% of fisheries products that harvested in Lake Shinji in a year is *Corbicula japonica*. *Corbicula japonica* is a representative aquatic product of Lake Shinji (Shinjiko Fisheries Cooperative Association n.d.). *Corbicula japonica* yields in Lake Shinji has been on the decline in recent years due to unfavourable habitat conditions (Figure 1.6).

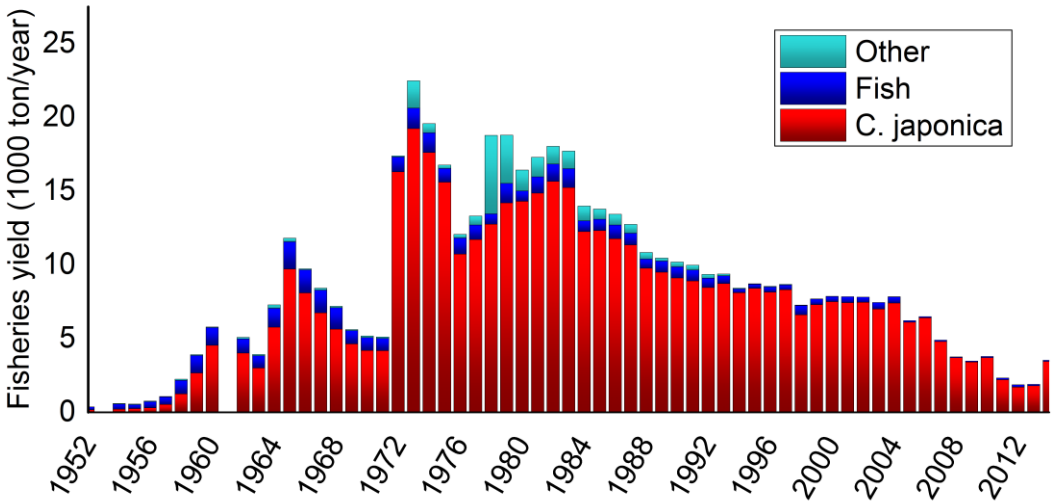

Figure 1.6 Long-term variations of fisheries yield in Lake Shinji (Shinjiko Fisheries Cooperative Association n.d.)

The Lake Shinji is well mixed with low salinity which is stable at approximately 5 PSU. Salinity stratification occasionally develops in the bottom layer after saline water intrusion, however it can be destroyed under high wind velocity condition. This is because the lake is far from the Japan Sea whose tidal range is small; hence tidal waters have limited effect on its salinity. On the other hand, salinity in Lake Nakaumi dramatically fluctuates and it has two layers (approximately 10 PSU at the surface and 25 PSU at the bottom). The Lake is near the Japan Sea and the salinity, especially in the bottom layer is affected by tidal waters. Therefore, bivalves and other benthic fauna inhabiting Lake Nakaumi are exposed to high and fluctuating salinity all the time unlike those in Lake Shinji. Salinity levels in the Lakes Shinji and Nakaumi vary from day to day depending on meteorological and hydrological conditions as well as tidal range.

Figure 1.7 show that in Lake Shinji *Corbicula japonica* populates shallow areas mainly less than 3 m covered with sandy sediment. The shallow areas generally have well

oxygenated water and salinity is low. Within littoral benthic region of the lake, the bivalve population density can be up to 3,800 individuals per m^2 (Nakamura & Kerciku 2000).

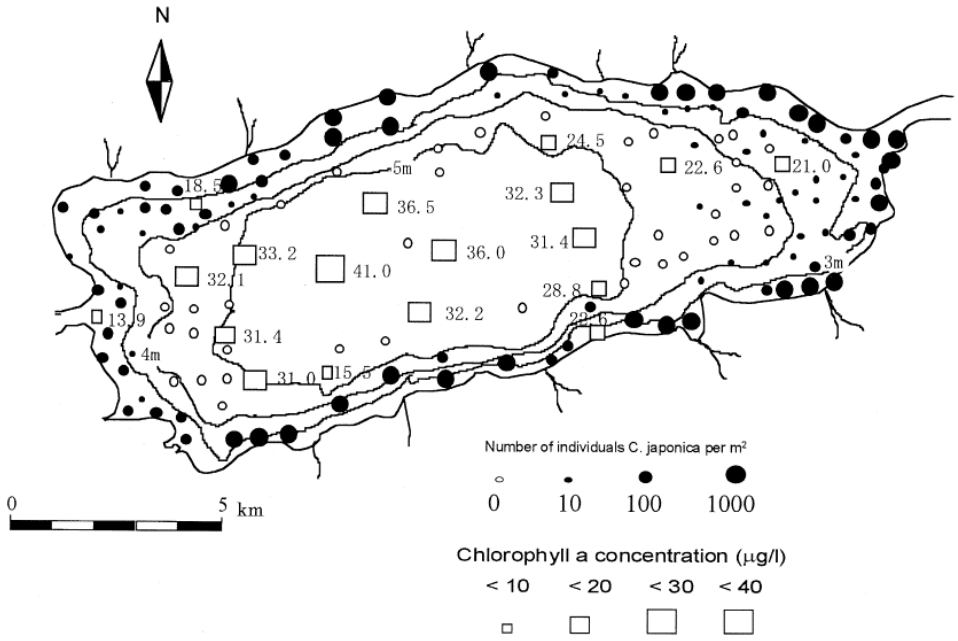

Figure 1.7 Distributions of population density of *Corbicula japonica* and chlorophyll-a in surface water in Lake Shinji (Nakamura & Kerciku 2000)

The limiting effect of salinity on the spawning, larval development and survival of *Corbicula japonica* is S-shaped characterized by three ranges: lethal, limiting and non-limiting (Figure 1.8) (Yamamuro et al. 1990; Baba 2006). The maximum spawning probability is reached within the larval development limiting salinity range (Figure 1.8). *Corbicula japonica* is spawned at *blastula* stage and needs high salinity for the development to D-shaped veliger (Baba 2006).

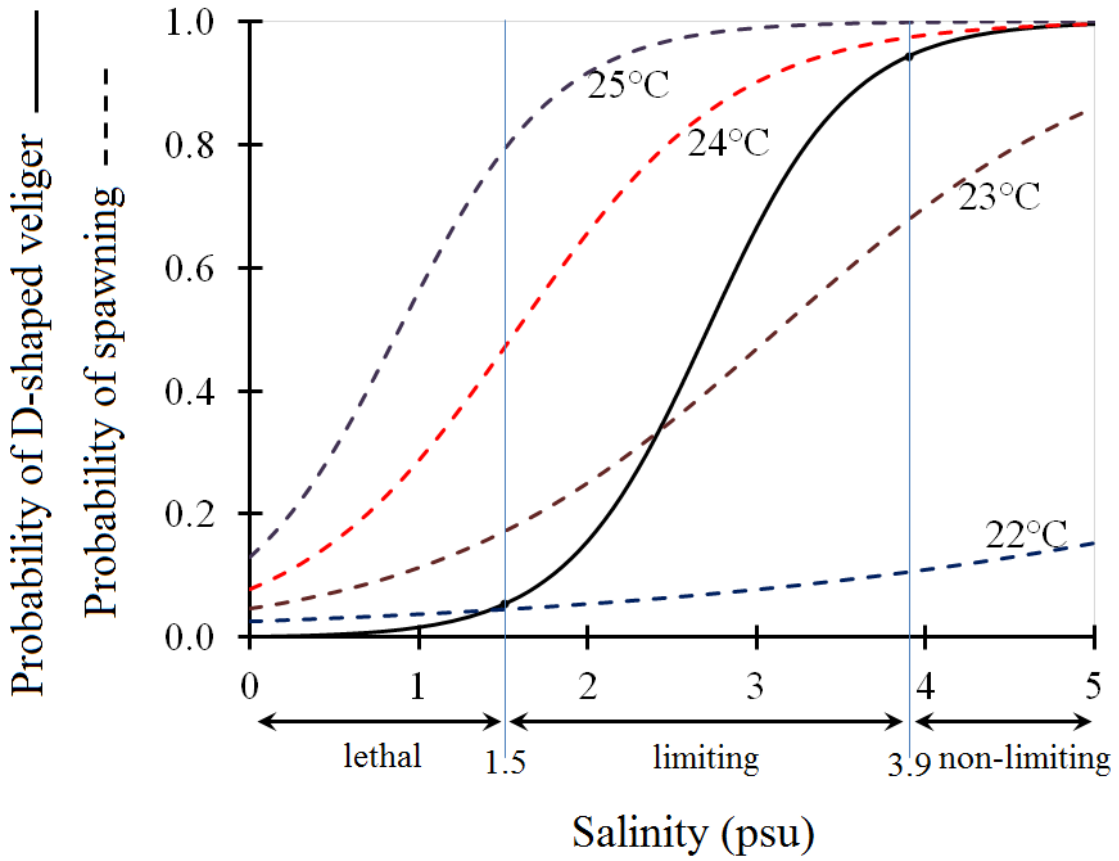

Figure 1.8 Relationships between salinity and the probability of the *Corbicula japonica* D-shaped veliger 24 hours after spawning and relationships among salinity, temperature and the spawning probability (Baba 2006)

It has been suggested that the early stage *Corbicula japonica* planktonic larvae gather in the high salinity zone where sufficient salinity exists for the larval development (Figure 1.9) (Baba 2006). The later stage planktonic larvae prefer lower salinity than early stage larvae, so they migrate upwards looking for the favourable sediments for settlement. After failing the find favourable sediments, the planktonic phase is postponed and the larvae floats to the lake surface where they grow up to 200 μm. The large planktonic larvae (shell length 170 – 200 μm) at the lake surface have greater chance of being transported to the favourable habitat on the peripheral (and/or shallow) areas due to wind stress (Baba 2006).

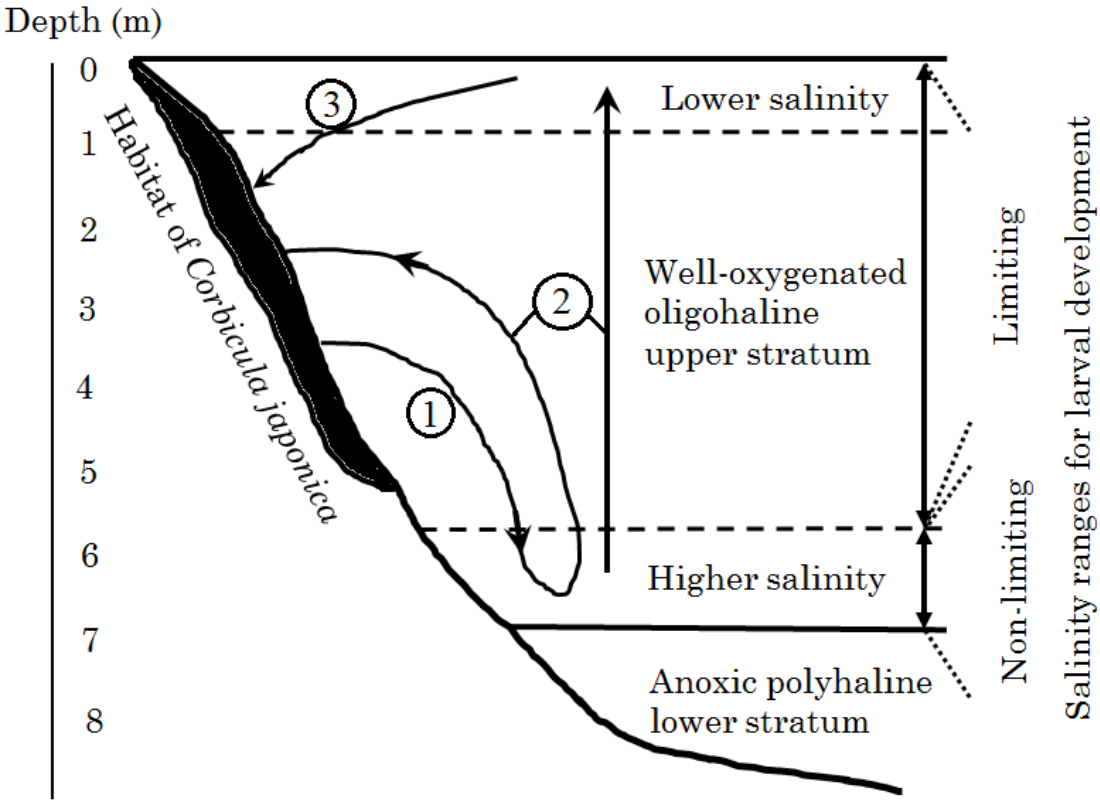

Figure 1.9 Salinity ranges for *Corbicula japonica* larval development. After spawning Corbicula japonica: 1. The early stage planktonic larvae assemble the higher salinity zone, to gain sufficient salinity for the larval development. 2. The later stage planktonic larvae migrate upward looking for conducive sediments to settle on. Or after failing to find favorable sediments, larvae proceed to the surface, the planktonic phase is postponed and the larvae grows to 200 µm. 3. At the surface the bigger planktonic larvae has a better chance of being transported to a conducive habitats and once they found them, the larvae settle. (Baba 2006)

1.3 MOTIVATION TO STUDYING MIXING AND SALT FLUX PROCESSES

Seawater intrusion/stratification and the presence of hypoxic conditions are common phenomena found in estuarine systems – thereby modifying their ecosystems. In Lakes Shinji and Nakaumi, hypoxia is often correlated with the occurrence of salinity-induced density stratification of the water column. The dynamics of saltwater intrusion and mixing processes are not clearly acknowledged.

Various studies (experiments and numerical models) have been conducted to understand the physical, chemical and biological processes in Lakes Shinji and Nakaumi (Yamamuro & Koike 1993; Yamamuro & Koike 1994; Nakamura & Kerciku 2000; Nakamura et al. 1997; Mizoyama et al. 2011; Sakai et al. 2004; Sakai et al. 2012; Nakata et al. 2000; Hiratsuka et al. 2007). Numerical models attempted to synthesize the information and understand the role of each process in the long term, but many failed to clearly reproduce observed dynamics of saltwater intrusion. To the best the author's knowledge no study exists which compute salt flux in the two lakes.

1.4 SCOPE AND OBJECTIVES

A brackish lake can be defined as an enclosed coastal water body with restricted communication to the open sea and an inflow of freshwater which measurably dilutes the seawater. The water at any point of the lake consists of a mixture of freshwater and seawater with proportions, and therefore the density of water varies with position. This internal distribution of density defines brackish lakes and estuaries. For this reason, the Lakes Shinji and Nakaumi are considered as a coupled brackish lake system influenced by both river discharge and the intrusion of sea salts.

The density distribution gives rise to pressure gradients which tend to produce a circulation in which water moves seaward in an upper layer and upstream (or landward) in a lower layer. Estuarine circulation includes this convective movement and the net movement that is needed to remove excess freshwater that may be added. The circulation can also be influenced by tides, gravitational circulation, wind and atmospheric pressure. Gravitational circulation tends to reduce convective circulation. Strong tidal currents,

river discharge or wind can generate turbulence, promoting vertical mixing and thus reducing gravitational circulation.

This study attempts to analyse the salinity and velocity distributions observed at Nakaura Watergate and simulated in Lakes Shinji and Nakaumi. The objectives are to define the exchange and circulation processes, to compute the salt flux at Nakaura Watergate and sections in the lakes, and to estimate the relative importance of the processes contributing to the salt balance. Horizontal and vertical dispersion coefficients will also be estimated.

2 MECHANISMS DRIVING WATER EXCHANGE PROCESSES AND CIRCULATION IN SAKAI CHANNEL, JAPAN

2.1 INTRODUCTION

Two main processes ,tidal pumping/trapping and steady baroclinic flows, drive water exchange between the sea and estuarine lagoons (Pereira & Lessa 2009). Water exchange process is crucial for understanding of ecosystems and management of water quality in brackish water lakes (Mizoyama et al. 2011). Current flow stratification and vertical gradients of salinity in the water column leads to circulation within an estuarine lagoon and between the estuarine lagoon and the sea. The mechanisms that drive tidal and subtidal circulation are influenced by river discharge, water balance, winds and sea-level oscillations (tidal and subtidal), hence may vary with season. Therefore, there may exist alternating retention, import or export of suspended matter and solutes dependent on the time of the year and tidal conditions.

The coupled estuarine lagoons, Lakes Shinji and Nakaumi, are located in the western Japan Sea coast. Lake Shinji has an average depth of 4.5m, surface area of 80km^2 and volume of 0.366km^3. Lake Nakaumi has an average depth of 5.4m, surface area of 86.2km^2 and volume of 0.47km^3. Hii River, at the western part of Lake Shinji, supply most of the fresh water into this lagoon system. The two lakes are connected by the Ohashi River (length: 7.3). Sakai Channel (length: 7.5 km, average width: 0.42 km, average depth: 10m) connects Lake Nakaumi to the Japan Sea. Consequently, this lagoon system has different salinities ranging from mesohaline to polyhaline within a distance of just 30 km. Lake Shinji is a mesohaline lake with average salinity between 1 and 6 psu, although

sometimes saline water intrudes forming a thin layer on the bottom. Seawater from the Japan Sea enters Lake Nakaumi along the bottom of the lake to the mouth of Ohashi River forming the hypolimnetic layer. Brackish water from Lake Shinji flows into Lake Nakaumi through Ohashi River forming the surface layer. This result in the formation of a strongly differentiated two-layer system in Lake Nakaumi, with salinity of the surface water being 14-20 psu and that of the bottom layer 25-30 psu. These brackish lakes are considered stably stratified due to salinity (density) differences, and density gradients have a large impact on water movement in this system (Okuda 2004).

Geographical characteristics of Sakai Channel limits water exchange between Lake Nakaumi and Miho Bay. The construction of Nakaura Watergate near the entrance of Sakai Channel in 1974 and construction of a Moriyama dike which encloses the northwest Lake Nakaumi (called Honjo District) in 1981 further inhibited water exchange (Uye et al. 2000). Tidal amplitude on the Japan Sea is small; hence, astronomical tides are not considered an effective water exchange mechanism. Meteorologically (atmospheric pressure) induced sea surface variation (MISSV) and large periodic river discharge are considered effective water exchange mechanism between the Miho Bay and Lakes Nakaumi (Nakata et al. 2000). Other potential water exchange mechanism are gravity-induced overturn, or wind-induced overturn (Nakata et al. 2000). However, as far as we know, the main forcing mechanism driving the water exchange between this system and the Japan Sea is unclear.

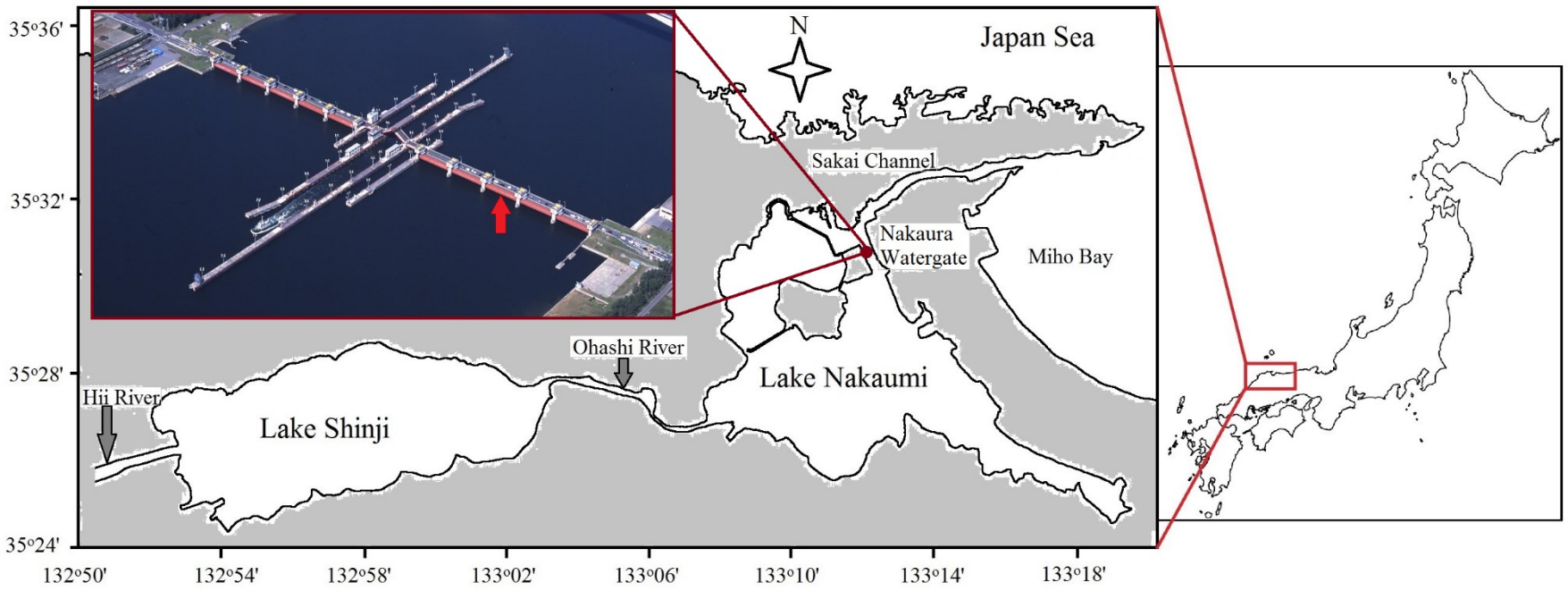

Figure 2.1 Location Lakes Shinji and Nakaumi, and Nakaura Watergate monitoring station (insert). Red arrow indicates the middle eastern side floodgate, the location of sampling and measurement equipment.

This chapter analyses existing sets of hydrodynamic data collected at Nakaura Watergate covering the summer and winter seasons of 2001. The study seeks to improve the understanding of the flow structure in the Sakai Channel and the potential for exchange of suspended matter and solutes between the Japan Sea and Lake Nakaumi.

2.2 MATERIALS AND METHODS

2.2.1 Data measurements

All the data used in this study, unless otherwise stated, was collected by Shimane Prefectural Institute of Public Health and Environmental Science (SPIPHES) at Nakaura Watergate water quality monitoring station, Sakai Channel (insert, Figure 2.1). Continuous monitoring of water level, current velocity, temperature, salinity and dissolved oxygen was done over a period of six years (February 1998 to March 2004). The process was controlled by a computerized telemetry system, which transmitted the measurement results once day to the SPIPHES's main computer. Although data was downloaded regularly, equipment malfunction resulted in several data losses. The hydrodynamic data for the summer period (May – August 2001) and winter period (mid-November 2001 – February 2002) is used in this analysis. Continuous measurements of hydrodynamic and water quality data in the Sakai Channel before the construction of the water gate and after its removal do not exist

The orientation of Nakaura Watergate was in the east-west direction and the direction of flow at this location is almost south–north, that is, ebb tidal current is northwards and flood tidal current southwards. Nakaura Watergate (width 414m, height 6.8m) had a total of 13 floodgates; three at the centre, and five floodgates on each side

(each 32m long). On the western pile of the middle east-side floodgate (indicated by red arrow, Figure 2.1), submerged water pumps were installed for water sampling at depths of 1, 3, 4 and 6m from the bottom. The water was pumped to acrylic boxes in the floodgate control building, where water temperature, electrical conductivity and dissolved oxygen were measured every thirty minutes using custom-made sensors (Alec Electronics Co., Ltd.). Salinity was calculated from electrical conductivity measured at Nakaura Watergate. Acoustic Doppler Profiler (Nortek ADP) was installed in the centre of the 3rd floodgate on the eastern side of the Nakaura Watergate (indicated by red arrow, Figure 2.1), at the bottom of the lake. Current velocity measurements were taken every hour at depth intervals of 0.5 m, from 1 m to 6 m above the bottom. Along-channel current vector component is used in this study. Positive along-channel velocities were ebb directed (northward flow), whilst negative values were associated with southward (flood) flow.

2.2.2 Data analysis

2.2.2.1 Water level

Water level was monitored at Nakaura Watergate by SPIPHES. Harmonic analysis of two 90-day data set, summer (22 May to 19 August 2001) and winter (15 November 2001 to 12 February 2002), was performed using the MATLAB program T_TIDE_V1.3 (Pawlowicz et al. 2002). 35 constituents were used in the harmonic analysis to obtain amplitude and phase. The tidal ranges and tidal asymmetry, as well as the power spectral density were determined from the same data. A Fourier low-pass filter, with a cut-off period of 33 hours was applied to the times series to remove low frequency fluctuations from tidal oscillations.

Tidal asymmetry was determined from skewness, the normalized sample skewness of the tidal elevation time derivative ($\zeta' = \partial\zeta/\partial t$). The skewness reveals the duration asymmetry in the rise ($\zeta' > 0$) and fall ($\zeta' < 0$) of water level.

$$\gamma = \frac{n\sqrt{n-1}}{n-2} \frac{\sum_{t=1}^{n}(\zeta_t' - \overline{\zeta'})^3}{(\sum_{t=1}^{n}(\zeta_t' - \overline{\zeta'})^2)^{3/2}} \quad (2\text{-}1)$$

The summation is for *n* observations from time t = 1 to t = *n*. $\gamma < 0$ indicates shorter duration for ebb-tide and $\gamma > 0$, shorter duration for floodtide. A time series skewness was produced by using a short 25-hour window. The skewness is affected by the chosen length of the window or the starting point relative to tidal stage. A window length equal to an integer multiple of the mean lunar day (24.84 hours) or an integer multiple of 25 hours (for observations comprised of hourly samples), will minimise the sensitivity of skewness to the starting point (Nidzieko 2010). A long window length averages spring-neap changes in asymmetry.

2.2.2.2 Current velocity

Current data during the same summer period (22 May to 19 August 2001) and winter period (15 November 2001 to 12 February 2002) was also analysed. Fourier low-pass filter was used to separate subtidal components (periods > 33 hours) from tidal and above components (periods < 33 hours) in all time-series. Astronomical tidal constituents were calculated using the MATLAB program T_TIDE_V1.3 (Pawlowicz et al. 2002). The calculated residual current is the sub-tidal flow separated from the tidal current using T_TIDE_V1.3 harmonic analysis program. Maximum ebb and flood current velocities for each tidal cycle (25-hour window) were extraction from the tidal current time series.

The tidal current asymmetry was then investigated through the calculation of the natural logarithm of ratio of maximum absolute flood-velocity over maximum ebb-velocity (Pereira & Lessa 2009; Lessa & Masselink 1995). The natural logarithm of this ratio provides an equal distribution of both positive (stronger flood) and negative (stronger ebb) asymmetries, enabling the graphical interpretation.

$$current\ ratio = \log_e \frac{|V_{max-flood}|}{V_{max-ebb}} \quad (2\text{-}2)$$

2.2.3 Salt and Nutrient Transport and Vertical Stability

2.2.3.1 Salt and nutrient transport theory.

Instantaneous advective mass transport properties (M_p, $kgm^{-1}s^{-1}$) per unit width of a section, normal to the longitudinal flow of the channel, is given by the following expression (Vaz et al. 2012; Moser et al. 2005):

$$M_p = \int_0^h VPdz = \overline{VP} \cdot h \quad (2\text{-}3)$$

where ρ is the density, V is the longitudinal velocity component and salinity, and P is the property (dissolved oxygen, ammonium, nitrite, nitrate, and dissolved inorganic nitrogen (DIN)) concentration. The upper bar denotes averaging over the total depth of the water column, h.

For the instantaneous advective salt transport (M_s, $kgm^{-1}s^{-1}$) calculation, equation (2-3) is multiplied by density, since salinity is a dimensionless property.

$$M_s = \int_0^h \rho V S dz = \overline{\rho V S} \cdot h \tag{2-4}$$

where ρ is the density, and S is the longitudinal salinity.

The non-tidal transport properties (T_p) over one or more tidal cycles (T) is given by

$$T_p = \frac{1}{T} \int_0^T M_p dt = \langle \overline{VP} \cdot h \rangle \tag{2-5}$$

The non-tidal salt transport (T_s) is given by

$$T_s = \frac{1}{T} \int_0^T M_s dt = \bar{\rho} \langle \overline{VS} \cdot h \rangle \tag{2-6}$$

where the mean density $\bar{\rho}$ is assumed to be constant and the angle brackets denote averaging over one or more tidal cycles. The time interval T is a multiple integer of the tidal period.

The correlations between fluctuating property concentration (salinity and nutrients) and velocity at a given point may be obtained through the decomposition of the instantaneous property concentration and velocity profiles into their mean, tidal, steady and deviation terms (Vaz et al. 2012). For a laterally homogeneous channel or when the property concentration transport is calculated per unit width of a section perpendicular to the mean flow at time t, these profiles may be written as,

$$V(x,z,t) = V_a(x) + V_t(x,t) + V_s(x,z) + V'(x,z,t) \quad (2\text{-}7)$$

$$P(x,z,t) = P_a(x) + P_t(x,t) + P_s(x,z) + P'(x,z,t) \quad (2\text{-}8)$$

where the mean component $V_a = \langle \bar{V} \rangle$, the tidal (barotropic) component $V_t = \bar{V} - V_a$, the steady (steady-state depth-varying baroclinic vertical velocity) component $V_s = \langle V \rangle - V_a$, and the deviation component $V' = V - (V_a + V_t + V_s)$. Similar expressions are valid in the P_a, P_t, P_s and P' computation.

The local depth *h(x,t)* at the anchor station varies with the tidal height and may be decomposed into two components (Vaz et al. 2012):

$$h(x,t) = h_a + h_t(x,t) \quad (2\text{-}9)$$

where $h_a = \langle h \rangle$ is the time-average water depth and $h_t(x,t)$ is the tidal height.

Substituting equations (2-7), (2-8) and (2-9) into equation (2-6), and neglecting terms with no physical expression, the advective salt transport under steady-state conditions was decomposed into seven terms (Vaz et al. 2012). Therefore, the mass transport properties, per unit width, during a tidal cycle is given by:

$$T_p = \underbrace{V_a h_a P_a}_{(a)} + \underbrace{V_t h_t P_a}_{(b)} + \underbrace{h_a \langle V_t P_t \rangle}_{(c)} + \underbrace{h_a \overline{V_s P_s}}_{(d)} + \underbrace{h_a \langle \overline{V'P'} \rangle}_{(e)} + \underbrace{\langle V_t P_t h_t \rangle}_{(f)} + \underbrace{V_a \langle P_t h_t \rangle}_{(g)} \quad (2\text{-}10)$$

For the salt transport calculation, equation ((2-10) was multiplied by depth averaged density $\bar{\rho}$, since salinity is a dimensionless property.

The terms (a) to (g) in equation (2-10) are related to certain physical mechanisms, and are listed in Table 2-1 (Vaz et al. 2012). The terms (a) and (b) represent the seaward salt advection by the mean current and Stokes wave transport. When taken together, they account for the transport of mean salinity by freshwater discharge, flushing the salt from the estuary thereby increasing the frontal gradient between the river and ocean (Vaz et al. 2012; Hunkins 1981). The terms (c) to (g) represent landward dispersion of salt through mixing by various processes, decreasing the frontal gradient. Term (d), the correlation between tidal salinity and current, transports freshwater downstream and salt upstream which in mixed and partially mixed estuaries does so through dispersion. When acting in the same direction of (a) and (b) this term increases frontal gradient, resulting into convective overturning conversely (Vaz et al. 2012; Hunkins 1981)

Table 2-1 Physical processes related with the terms of equation (2-10).

Term	Physical processes
(a)	Freshwater discharge or residual velocity
(b)	Stokes drift or progressive tidal wave transport
(c)	Topographic trapping
(d)	Gravitational circulation, bathymetric tidal pumping, steady wind effect
(e)	Tidal shear and unsteady wind effect
(f)	Tide dispersion via triple correlation
(g)	Net advection of cross correlation between salt and tide
	Source: (Vaz et al. 2012)

Under steady conditions, there is no net transport and the sum of the right hand side terms of equation (2-10) should be zero. Equations (2-6) and (2-10) are distinct mathematical expressions of the same quantity. Therefore, in order to check the

computational procedure and if the neglected terms are in fact small, a comparison of the net salt transport results computed using both equations will be used.

2.2.3.2 Density of water

The density of water was calculated using the following approximate density formula (Klinger n.d.):

$$\rho = 999.83 + 0.808S - \alpha(T)T - \gamma(T)(35 - S)T \quad (2\text{-}11)$$

$$\alpha = 0.0708(1 + 0.068T) \quad (2\text{-}12)$$

$$\gamma = 0.003(1 - 0.012T) \quad (2\text{-}13)$$

where T is temperature in °C and S is salinity in PSU.

2.2.3.3 Water column stability

The layer Richardson number was used to investigate the water column stability during a tidal cycle (Vaz et al. 2012).

$$Ri_L = \frac{gh\Delta\rho}{\overline{U}^2\bar{\rho}} \quad (2\text{-}14)$$

where, $h = h(\mathrm{t})$ is the local depth, $\Delta\rho$ is the difference between the bottom and surface density and $\overline{U} = \overline{U}(\mathrm{t})$ is the depth averaged velocity.

2.3 RESULTS AND DISCUSSION

2.3.1 Water Level

Water level at Nakaura Watergate reveals that the tides in Sakai Channel are mixed, but mainly semidiurnal, with a form factor, *F* of 1.24, and 1.14 during 2001 summer and 2001/2 winter, respectively. Form factor, *F* is computed with equation (2-15). This means M2 and S2 are the dominant surface tides in Sakai Channel. M_2 amplitude is 6.5 cm, and 7.08 cm, and phase is 76.54°, and 92.67° during summer 2001, and winter 2001/2, respectively (Table 2-2).

$$F = \frac{O_1 + K_1}{M_2 + S_2} \tag{2-15}$$

where the symbols of the constituents indicate their respective amplitudes

Table 2-2 Harmonic constituents of tide with 95% confidence limits at Nakaura Watergate.

	Season	**Summer**					**Winter**				
	Tide	O1	K1	N2	M2	S2	O1	K1	N2	M2	S2
Surface elevation	Amplitude (cm)	4.8	5.4	1.7	6.5	1.7	4.6	5.9	1.6	7.1	2.1
	Phase	314.2	358.1	53.7	76.5	118.3	315	350.9	78.4	92.7	127.4

Water level recorded at Nakaura Watergate shows higher water level during the summer season (May to August 2001) than the winter season (mid-November 2001 – mid-February 2002) (Figure 2.2). This is partly due to high precipitation during the summer period. Thermal expansion of sea water and atmospheric pressure also contributes to seasonal variation in water level. The mean water level was 7.37 m, and 7.03 m during summer season 2001, and winter season 2001/02, respectively. The water

level mostly varied between 6.6 m and 7.7 m in summer, and 6.6 m and 7.5 m in winter (Figure 2.2). The maximum surface elevation reached due to astronomical signal was 0.33 m, and 0.22 m during summer and winter, respectively (Figure 2.3 and Figure 2.4). Variance analysis of the synthesized and measured water levels shows that the astronomical tides accounts for less than 28% of the observed water surface elevation at Nakaura Watergate (Table 2-3). This implies that the astronomical tide plays a minor role in the tidal oscillations and the subtidal oscillations seem to play a pivotal role. The maximum subtidal surface elevation reached was 0.22, and 0.32 during summer and winter, respectively (Figure 2.3 and Figure 2.4). The period of subtidal oscillations ranged from 3 days to 6 days (Figure 2.5).

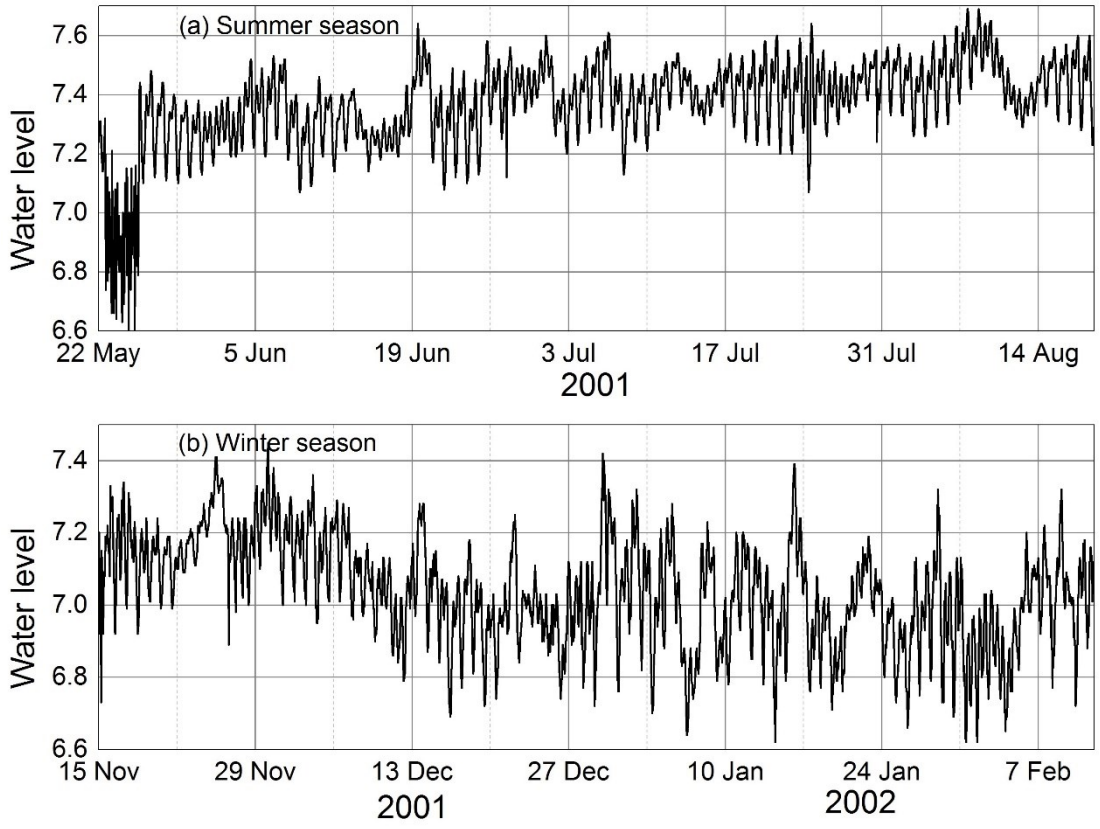

Figure 2.2 The water level during summer (a) and winter (b) seasons

Table 2-3 Ratio of variance residual after synthesis and original variance

Parameter	percent of var residual after synthesis/var original	
	summer (wet) season	winter (dry) season
Surface level	72.55%	73.33%
velocity_1.0m	19.10%	23.41%
velocity_1.5m	18.63%	22.50%
velocity_2.0m	17.49%	21.44%
velocity_2.5m	15.99%	20.12%
velocity_3.0m	15.19%	18.72%
velocity_3.5m	15.21%	16.74%
velocity_4.0m	16.09%	14.72%
velocity_4.5m	15.64%	13.07%
velocity_5.0m	15.04%	12.36%
velocity_5.5m	16.20%	12.63%
velocity_6.0m	13.65%	13.68%

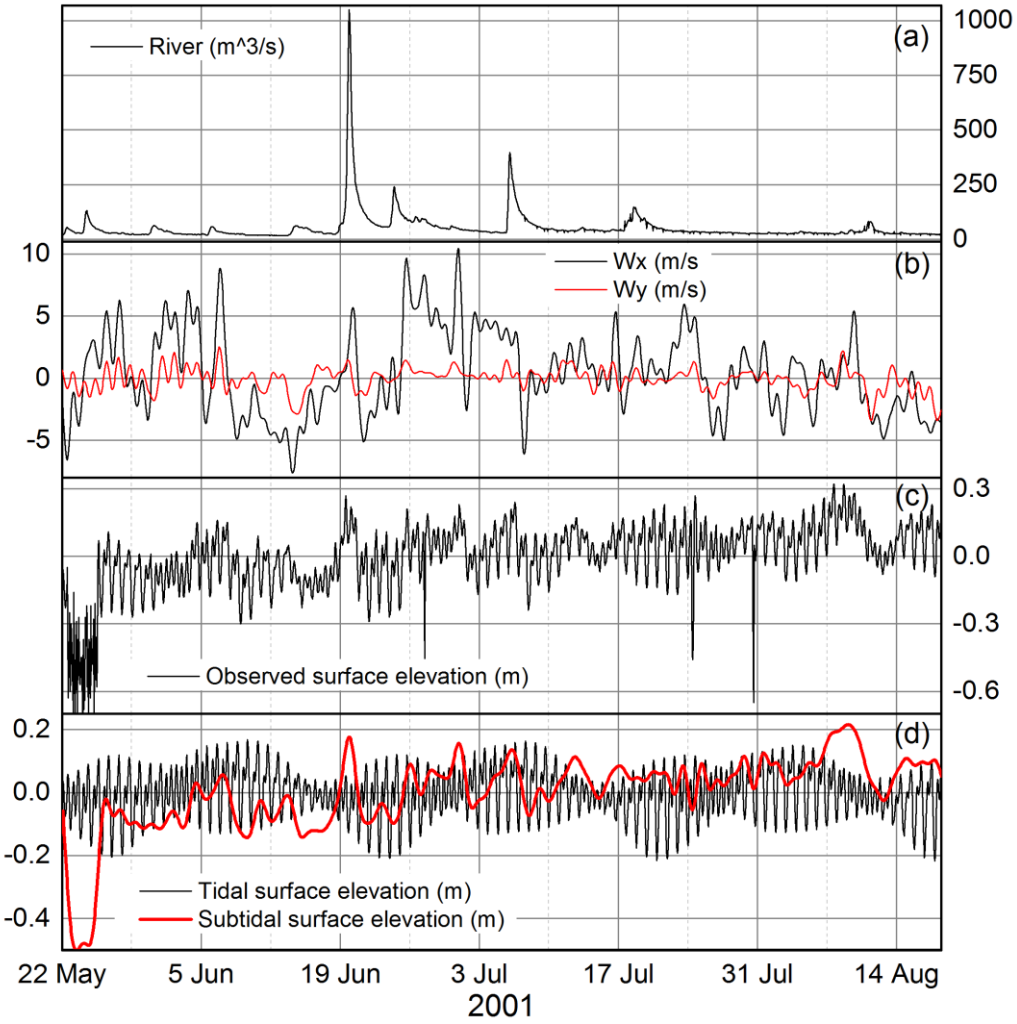

Figure 2.3 River discharge (a), low-pass filtered wind (b), observed surface elevation (c) and decomposed surface elevations (astronomical signal and the low-pass filtered signal) during summer period

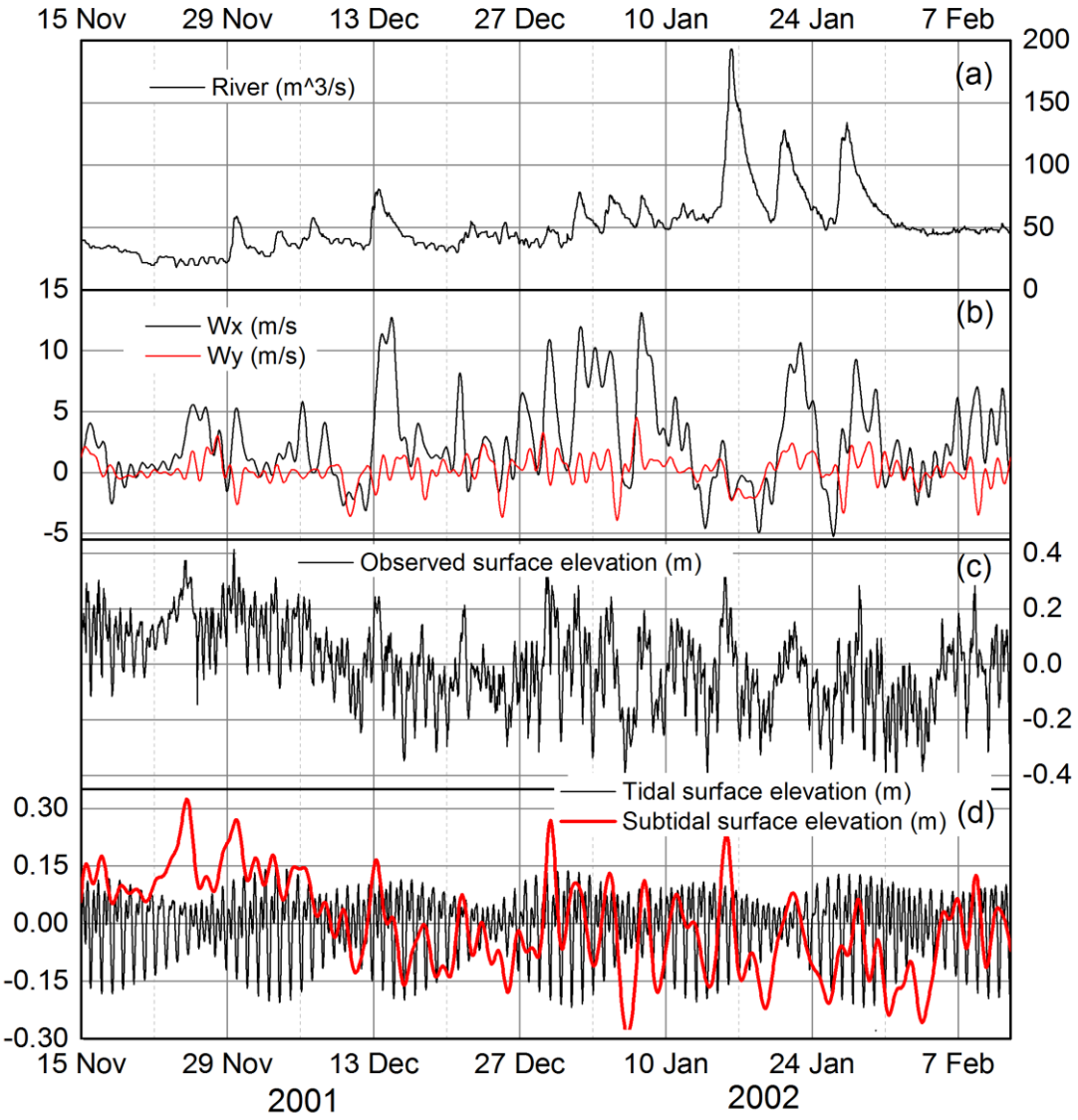

Figure 2.4 River discharge (a), low-pass filtered wind (b), observed surface elevation (c) and decomposed surface elevations (astronomical signal and the low-pass filtered signal) during winter period

Generally, the tide along Sakai Channel has a shorter falling water duration. The mean asymmetry over the duration of the observations was -0.36, and -0.73 for summer and winter season, respectively. Figure 2.6(b) shows the plot of the time-varying running-skewness computed with a 25-hour window length. The results distribution shows that majority of the skewness is negative (shorter duration for ebb tide), with shortest durations occurring during spring tides in winter. The skewness of the rising/falling tides

increased from spring to neap, different flooding rates may cause this phenomenon. Large distortions during neap tides may be a result of a slow rate of comparatively sufficient flood (Pereira & Lessa 2009). If the same volume of water flows in either direction during a tidal cycle, the shorter duration of the ebbing tide must result in faster velocities and ebb-dominant transport of suspended mater and solutes (Lessa & Masselink 1995). Ebb-tidal current dominance was observed almost throughout the lunar cycle, but mainly during the spring tides.

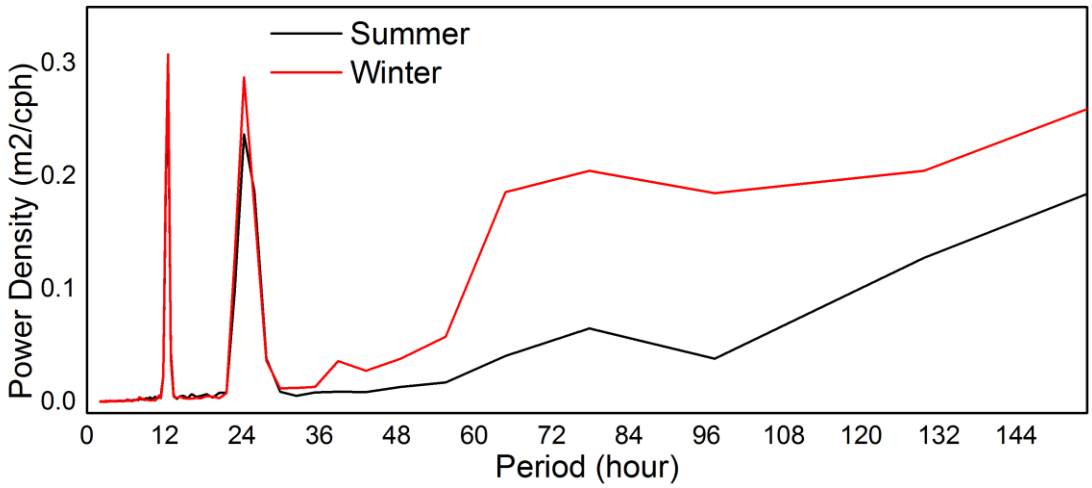

Figure 2.5 The spectral estimates of the water level time series

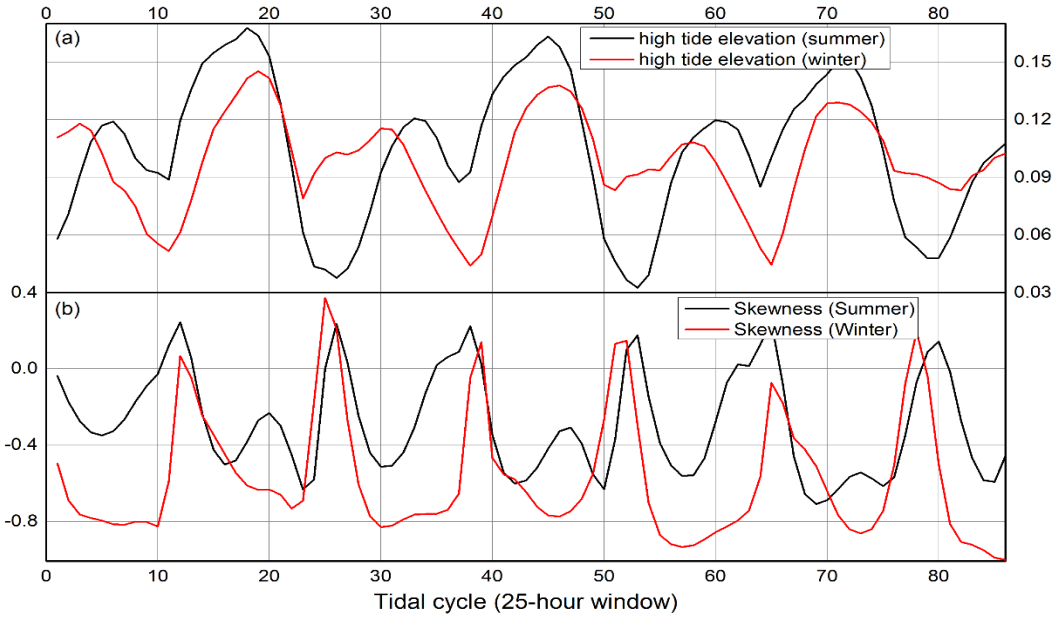

Figure 2.6 The high tide elevation (a) and the 25-hour skewness computed with equation (2-1) (b)

2.3.2 Current velocity

Figure 2.7 show the temporal evolution of vertical profile of the longitudinal component of current velocity measured at Nakaura Watergate. Positive values are ebb directed whilst negative values are flood directed.

Current velocity reveals that tides in Sakai Channel are mixed and mainly semidiurnal with a summer season form factor, F of 0.85, 0.73 and 0.52 in the bottom, middle and surface layers, respectively. The winter season form factor was 0.84, 0.59 and 0.6 in the bottom, middle and surface layers, respectively. The dominant tidal currents in the Sakai Channel are the two primary semidiurnal constituents M2 and S2 and the two

diurnal constituents O1 and K1 (Table 2-4 and Table 2-5). The M2 is the dominant semidiurnal constituent, with current amplitude at least 3 times larger than S2.

Figure 2.8 and Figure 2.9 show temporal variation of the depth averaged current velocity along the channel (decomposed into tidal and subtidal components) and the predicted velocity (from harmonic analysis) for the summer and winter period. Generally, the maximum current velocities were associated with the ebb tide, reaching 0.74 m/s and 0.65 m/s during summer and winter, respectively. Maximum neap tides current velocities were about half those during spring tides.

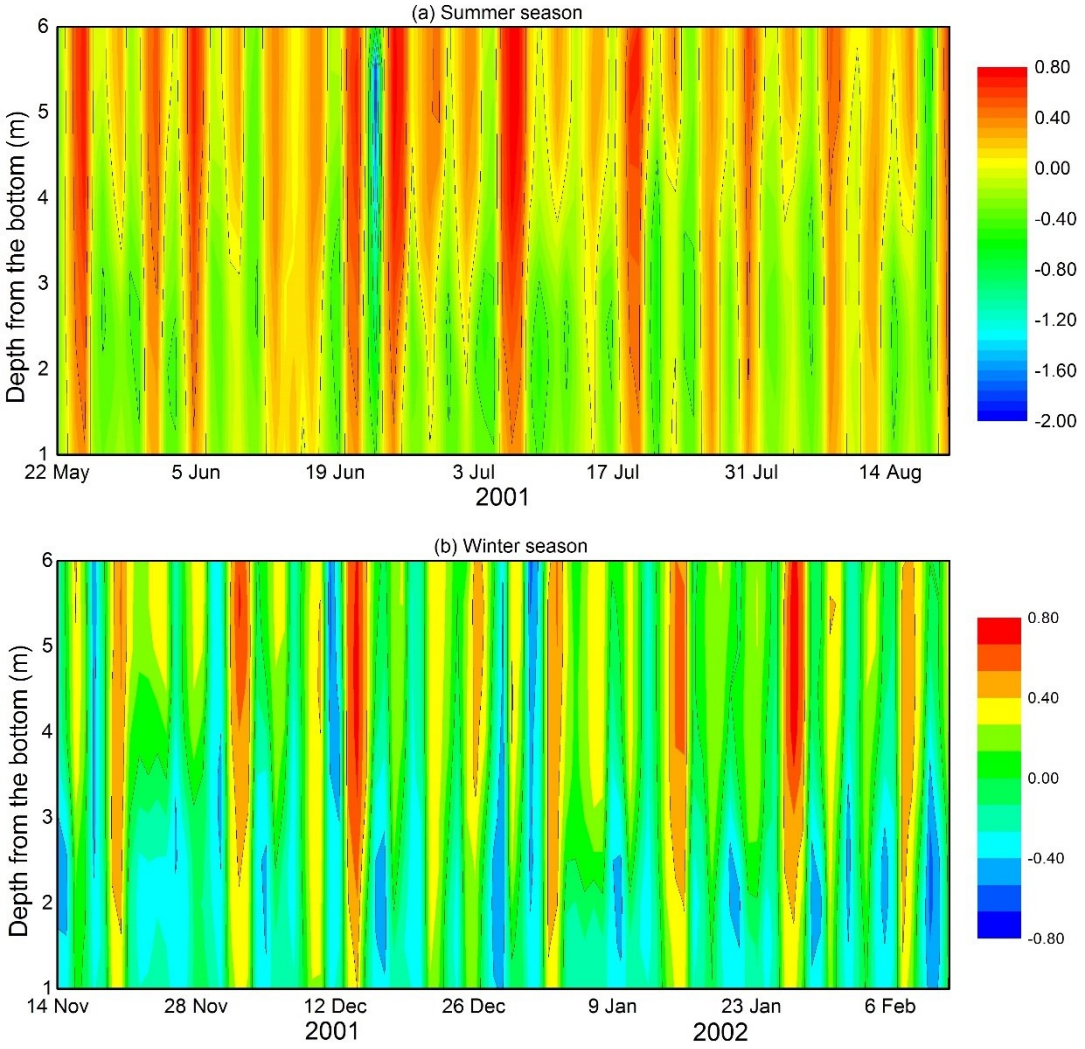

Figure 2.7 Vertical profile of water flow velocity as a function of depth and time for summer (a) and winter (b) seasons

Table 2-4 Harmonic constituents of tidal current with 95% confidence limits at Nakaura Watergate.

	Bottom layer		**Middle layer**		**Surface layer**	
Tide	Current amplitude (cm/s)	phase	Current amplitude (cm/s)	phase	Current amplitude (cm/s)	phase
MM	3.53	274.03	–	–	–	–
2Q1	1.60	6.15	–	–	–	–
Q1	2.31	77.60	2.29	42.87	2.43	27.63
O1	9.72	83.41	11.77	71.66	10.20	50.84
NO1	1.80	6.32	–	–	1.27	50.20
K1	14.25	117.50	17.66	119.77	10.91	98.96
OO1	1.02	154.73	1.64	180.17	–	–
MU2	1.72	85.75	2.39	87.16	–	–
N2	5.09	190.47	7.11	193.72	8.14	185.52
M2	21.73	193.24	30.56	201.42	31.01	194.2
L2	1.71	182.82	1.40	197.14	1.57	177.69
S2	6.56	217.31	9.49	220.54	9.69	224.51
SK3	–	–	1.43	163.54	1.1	165.23
MN4	–	–	1.14	218.62	1.78	237.68
M4	–	–	2.05	243.04	3.65	265.42
2MK5	1.70	339.70	1.36	40.52	–	–

–: insignificant constituents or current less than 1 cm/s

Table 2-5 Tidal current constituents with 95% confidence limits during winter season at Nakaura Watergate.

	Bottom layer		**Middle layer**		**Surface layer**	
Tide	Current amplitude (cm/s)	phase	Current amplitude (cm/s)	phase	Current amplitude (cm/s)	phase
2Q1	1.76	354.84	–	–	–	–
Q1	1.8	65.66	1.22	28.83	2.26	11.99
O1	10.09	87.77	10.17	68.01	8.42	40.4
K1	13.67	130.36	14.78	109.87	14.31	87.4
OO1	–	–	1.31	98.79	–	–
MU2	1.5	50.49	1.5	98.5	1.56	148.14
N2	4.22	185.31	6.96	186.42	6.98	187.05
M2	22.01	196.93	32.97	196.33	29.09	188.18
S2	6.3	220.06	9.52	222.38	9.09	226.47
MK3	2.02	322.56	1.28	119.45	3.05	91.04
SK3	–	–	1.13	172.13	1.2	135.51
MN4	–	–	1.1	200.5	1.68	215.79
M4	1.36	21.13	2.04	225.78	3.09	238.66
MS4	–	–	1.24	206.94	1.18	265.73
2MK5	2.08	341.98	–	–	1.24	142.14
M6	1.11	77.42	–	–	–	–

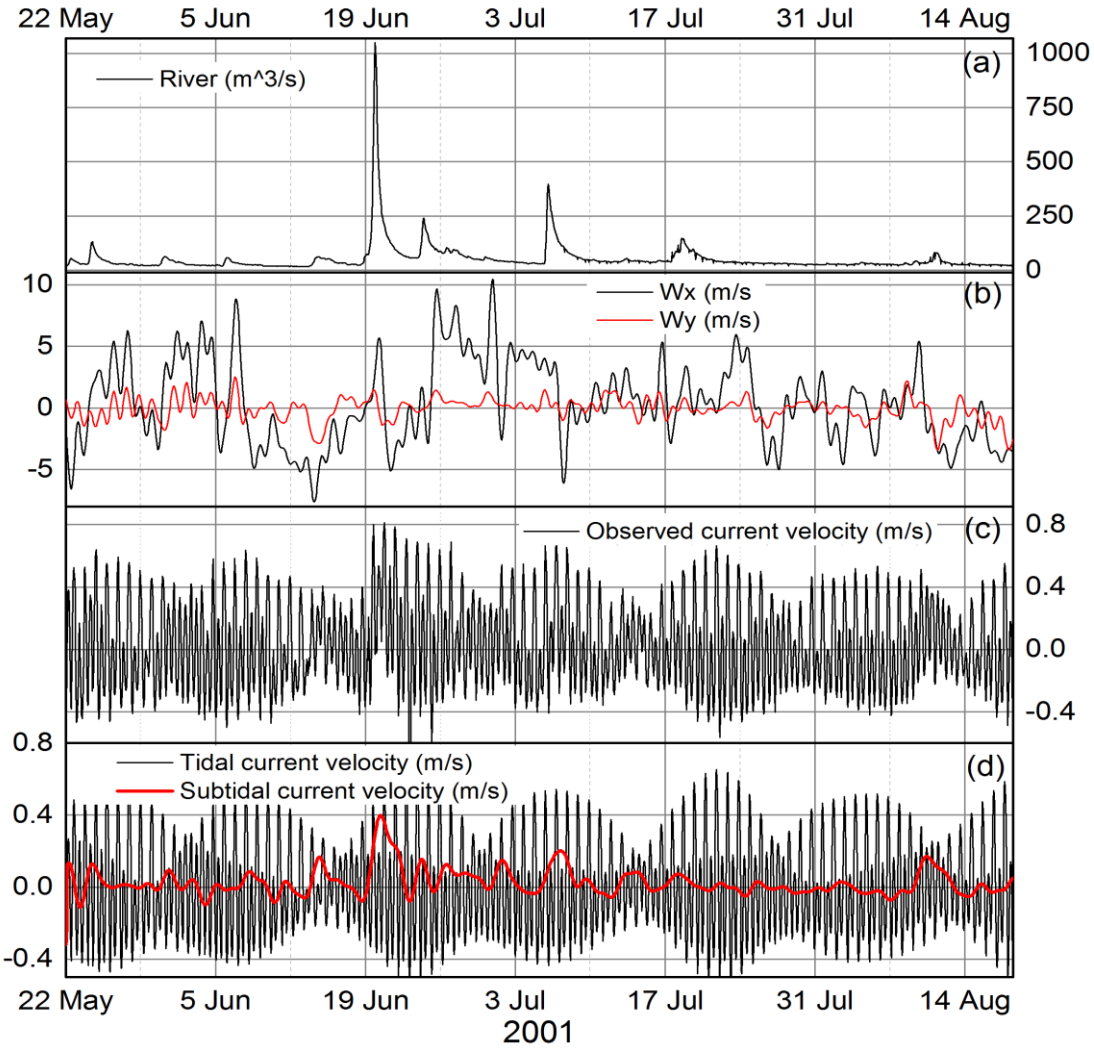

Figure 2.8 River discharge (a), wind speed (b), Variation of the depth averaged current velocity along the channel (c) (decomposed into tidal (black) and subtidal (red) components (d)) for summer season. Ebb (flood) current is positive (negative).

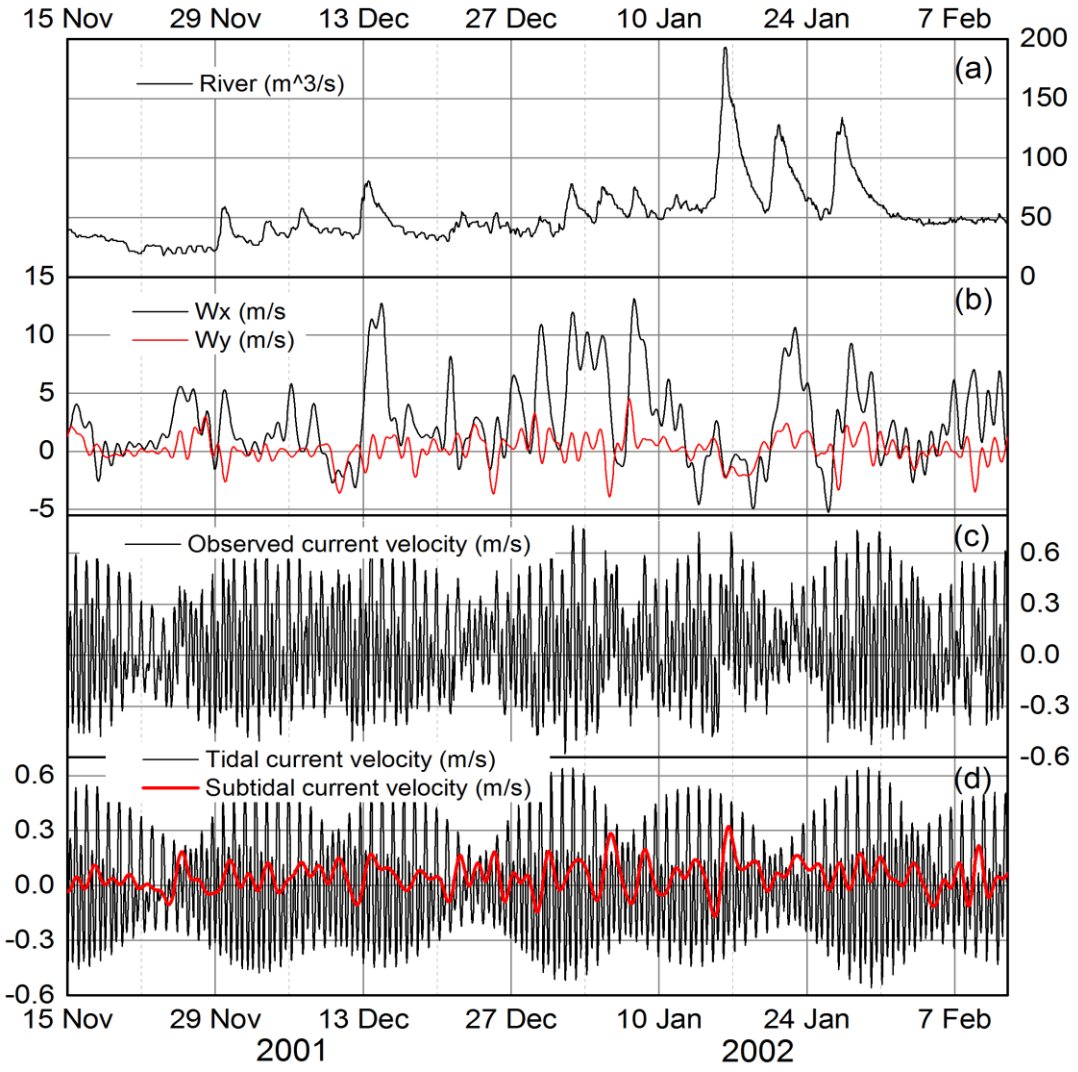

Figure 2.9 River discharge (a), wind speed (b), Variation of the depth averaged current velocity along the channel (c) (decomposed into tidal (black) and subtidal (red) components (d)) for winter season. Ebb (flood) current is positive (negative).

The water surface elevation at high tide tends to regulate the peak ebb and flood tidal current velocities. Although the observed data shows the existence of this phenomena, it does not show a clear trend as the case with predicted water surface elevation at high tide and current velocities. Figure 2.10 show the natural logarithm of the ratio of maximum flood-velocity to maximum ebb-velocity for each tidal cycle, plotted with high tide elevation. The calculated water surface elevation at high tide seems to

regulate the calculated peak ebb and flood tidal current velocities. The variations occur in the water column, however it can be seen that on average, ebb dominate during spring tides and flood dominate during neap tides. The duration of ebb dominance is longer than that of flood dominance.

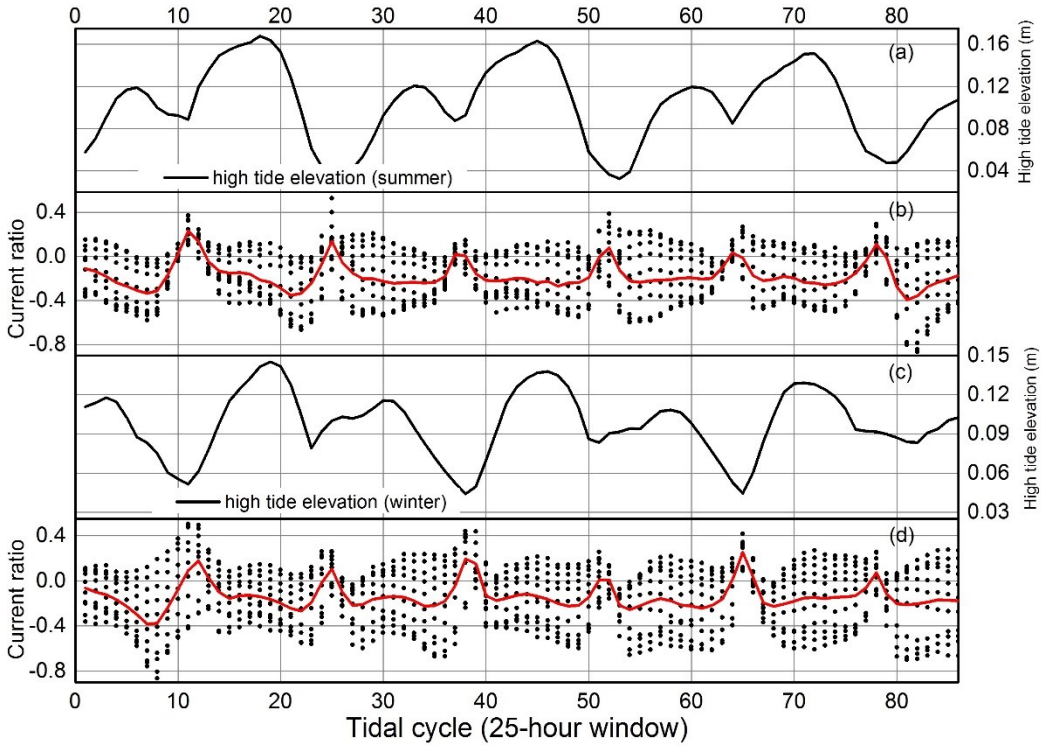

Figure 2.10 Variation of the calculated high water elevation in summer (a) and winter (c), and the mean natural log ratio of the maximum flood and maximum ebb current velocity for the water column (black dots) for summer (b) and winter (d). The red line indicates the mean water column current ratio. NB: a ratio of 0.69 (–0.69) means that the flooding (ebbing) tide is twice as fast as the ebbing (flooding) tide.

Contrary to water surface elevation, currents in Sakai Channel were closely related to the astronomical tides. Variance analysis of the synthesized current velocity field after harmonic analysis shows that the astronomical tides accounts for more than 80% of the current velocity variance during the summer season and more than 75% during winter season. Subtidal circulation accounts for less than 25% of current variance, with frequencies of 5 to 8 days during summer and around 3 days in winter (Table 2-3) (Figure

2.11). The correlation between observed and predicted tidal currents during summer and winter averaged 0.92 and 0.91, respectively

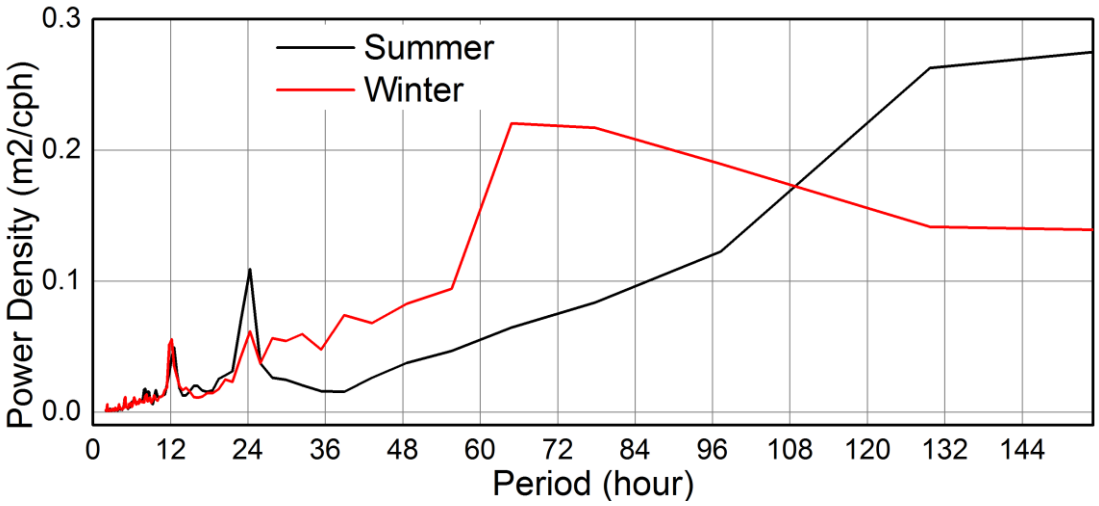

Figure 2.11 Energy density distribution of the current velocity time series after the removal of tidal energy.

On average, the magnitude of the ebb subtidal (low-pass filtered) currents were about 49% of the ebb tidal currents in both summer and winter seasons (Table 2-6). The ratio of the magnitude of the subtidal and tidal flood currents was 39% and 56% during summer and winter seasons, respectively. However, during the winter season at the surface layer, the magnitude of the flood subtidal currents was more than that of the tidal currents by about 28%. Subtidal flow in the Sakai Channel circulation is mainly stratified, with ebb currents dominating the surface and flood currents the bottom (Figure 2.12), indicating typical gravitational estuarine circulation. The typical gravitational estuarine circulation exists in both summer and winter seasons, as indicated by the calculated residual currents, whose magnitude varied between 0.09 m/s and 0.18 m/s (Figure 2.13). Gravitational circulation is strong during the summer season, due to high rainfall. Since

subtidal flow in Sakai Channel is stratified, the net transport of materials depends on the vertical concentration distribution.

The analysis of Figure 2.12 indicates the existence of other circulation modes. Occasional unidirectional inflows and outflows could be seen. As an example, around 21 and 22 June there was unidirectional flow towards the Japan Sea and the around 23 and 24 June almost a reverse (towards Lake Nakaumi) unidirectional flow occurred. Unidirectional flow is mainly ebbing flow.

Table 2-6 Ratio of magnitude of subtidal currents to that of tidal currents

	summer		**winter**	
Depth from the bottom	Ebb	Flood	Ebb	Flood
1.0m	43.4%	68.2%	25.2%	80.4%
1.5m	42.8%	64.8%	28.6%	74.4%
2.0m	40.3%	59.5%	27.1%	65.3%
2.5m	35.3%	50.3%	29.8%	52.1%
3.0m	32.4%	38.8%	36.7%	36.5%
3.5m	35.5%	26.1%	44.8%	26.3%
4.0m	41.4%	16.4%	57.6%	21.1%
4.5m	51.8%	14.0%	67.8%	20.4%
5.0m	65.1%	27.9%	73.8%	21.1%
5.5m	72.9%	28.4%	77.6%	86.7%
6.0m	79.5%	28.7%	76.7%	127.9%
Average	49.1%	38.5%	49.6%	55.6%

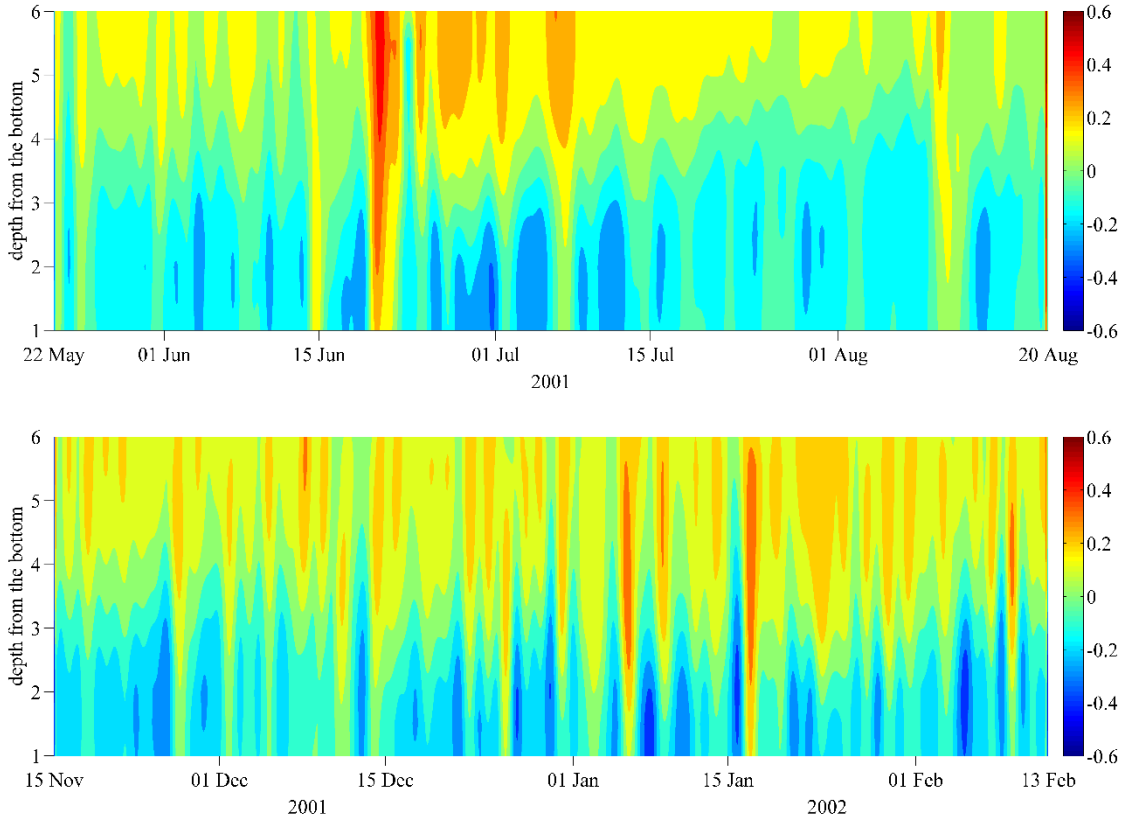

Figure 2.12 Low-pass filtered current field in the water column

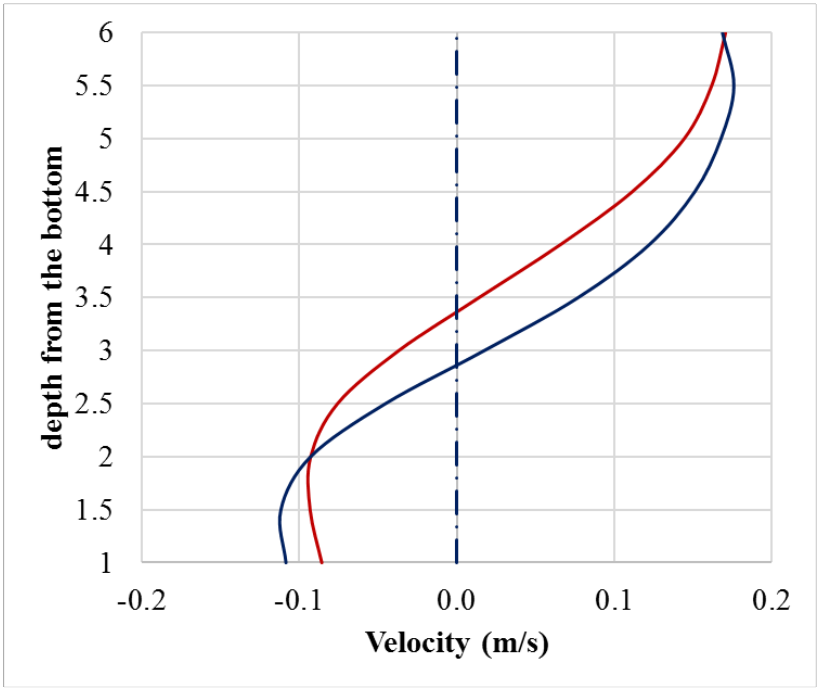

Figure 2.13 Residual current velocity in the water column in summer (red line) and winter (dark blue line)

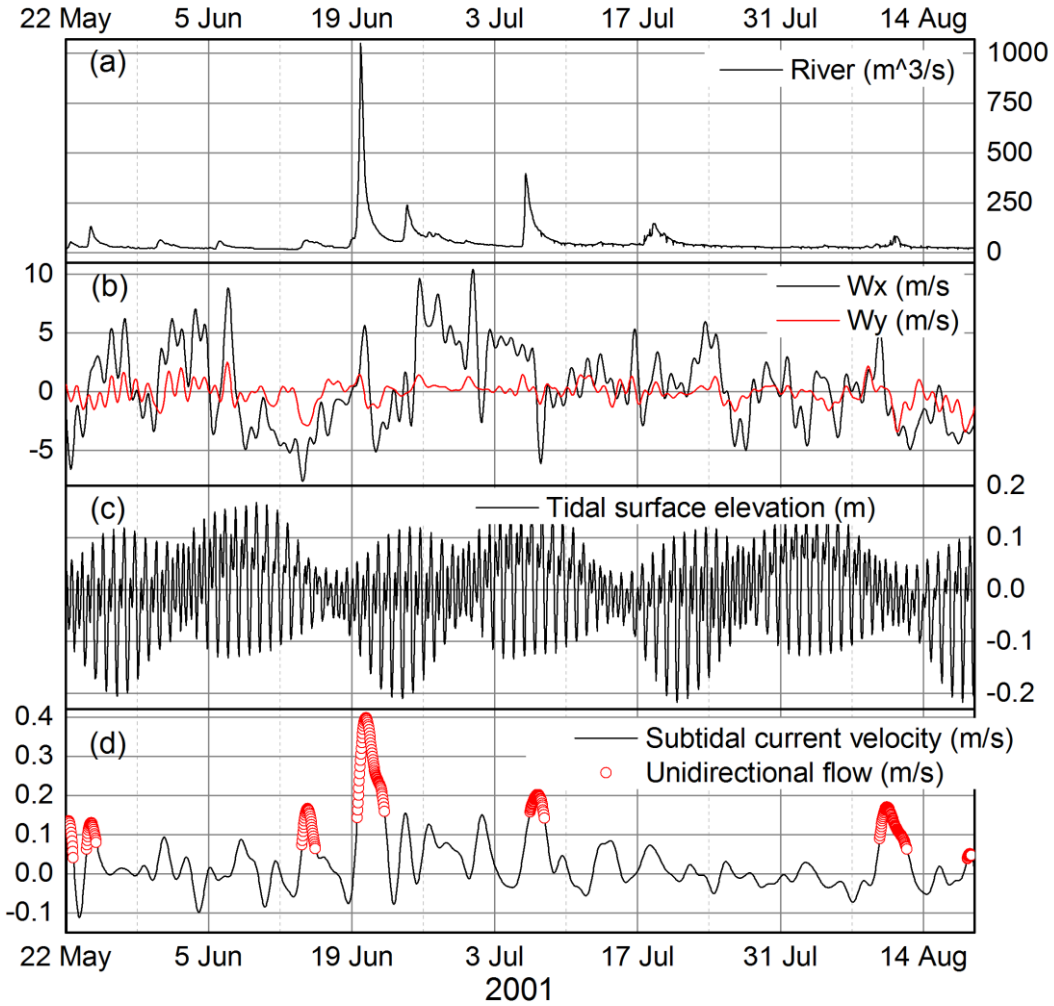

Figure 2.14 (a) River discharge, (b) wind speed, (c) surface elavation and (d) unidirectional subtidal flow occurrences (red circles), & depth averaged subtidal flow (black line), during summer of 2001

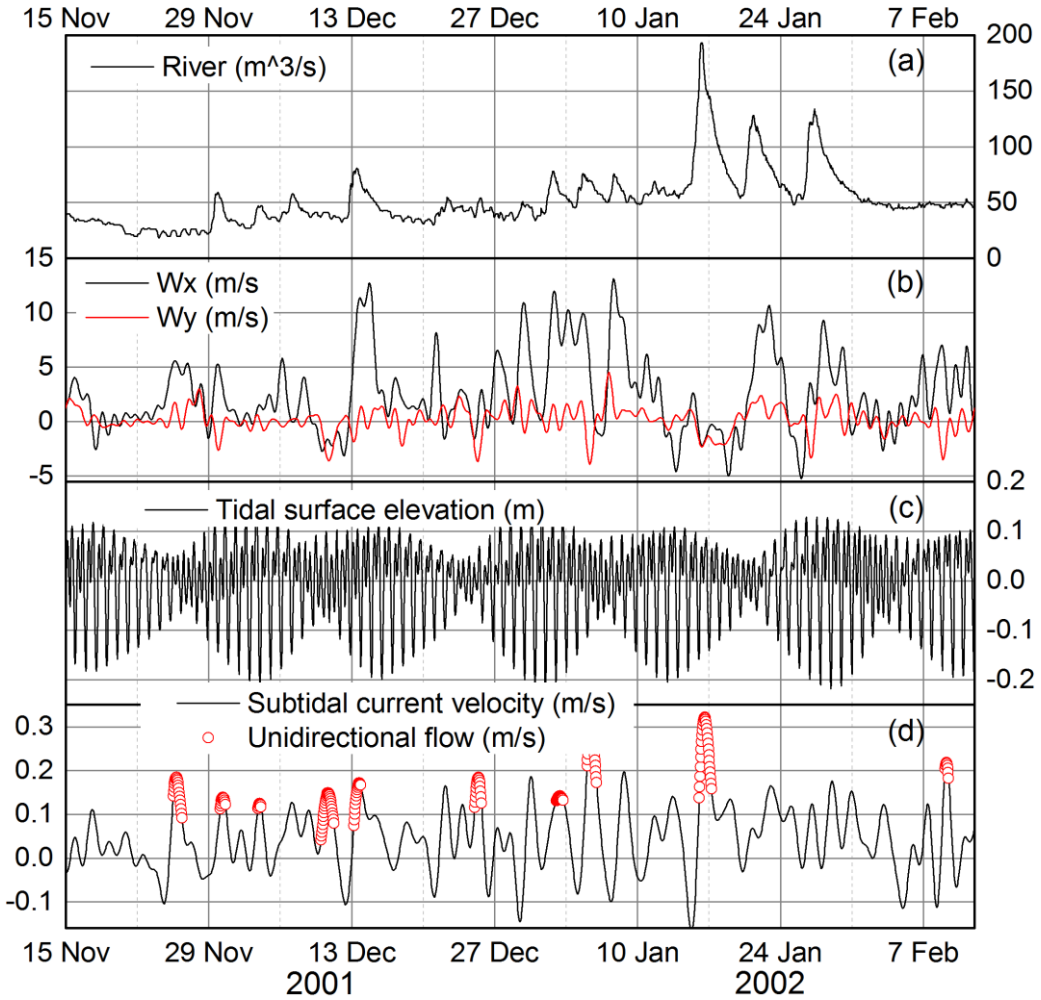

Figure 2.15 (a) River discharge, (b) wind speed, (c) surface elavation and (d) unidirectional subtidal flow occurrences (red circles), & depth averaged subtidal flow (black line), during winter of 2001/2

Figure 2.14 and Figure 2.15 shows occurrences of unidirectional subtidal flows, plotted with depth-averaged subtidal flow and predicted surface elevation (left y-axis) and river discharge (right y-axis). Non-stratified (unidirectional) ebb directed subtidal flow sporadically occurred mainly during neap tides in both summer and winter seasons. This is evident from Figure 2.12, Figure 2.14 and Figure 2.15, indicating the existence of other circulation modes. The longest duration of unidirectional flow towards the Japan Sea was about 65 hours during summer coinciding with highest river discharge around June 19th, and neap tides and increased river flow around August 9th. In winter

unidirectional flow occur for durations less than 30 hours and some coincide with increased river flows. Therefore, seaward subtidal circulation in the Sakai Channel is partly due to river discharge induced baroclinic circulation. Unidirectional flood directed subtidal flows are almost non-existent, hence tidal pumping and/or wind may not be strong enough to reverse the flow throughout the water column.

2.3.3 Water quality properties

Figure 2.16 shows the spread of temperature and salinity. The vertical salinity distribution is almost the same for summer and winter seasons. However, temperature distribution changes with seasons as expected. During summer, the surface layer is characterised by lower salinity and higher temperature, whereas the bottom layer has higher salinity and lower temperature. In winter, opposite is true for temperature, the surface layer has lower salinity and temperature and the bottom layer, higher salinity and temperature. Mean surface layer temperature values during summer and winter seasons were 25°C and 8°C, respectively. The bottom layer had mean temperature values of 22°C and 13°C in summer and winter, respectively (Figure 2.18). The vertical salinity gradient was generally high (Figure 2.17). Mean salinity values, both in summer and winter seasons, were 15 PSU and 30 PSU at the surface and bottom, respectively. Surface layer salinity was mainly clustered between 10 PSU and 24 PSU during summer and 5 and 23 PSU in winter. The bottom layer salinity ranged between 15 PSU and 33 PSU (summer season) and between 21 PSU and 33 PSU (winter season). Bottom layer salinity showed consistent higher values (>30 PSU), both in the summer and in the winter seasons regardless of the tidal cycle or river discharge (Figure 2.17). This reveals consistent presence of seawater.

Figure 2.17 show the temporal evolution of vertical profiles of the salinity measured at Nakaura Watergate. Density stratification is observed throughout the analysis period. Figure 2.18 show thermal stratification during summer period (May, June, July and August) and winter period (November, December, January & February). During spring and fall the water column is thermally well mixed. The density profiles in Figure 2.19 shows that the mean density at the bottom was always higher than at the surface. Mean density values at these respective layers were 1020.28 kg/m^3 and 1006.56 kg/m^3 in summer season and 1021.77 kg/m^3 and 1010.37 kg/m^3 in winter season.

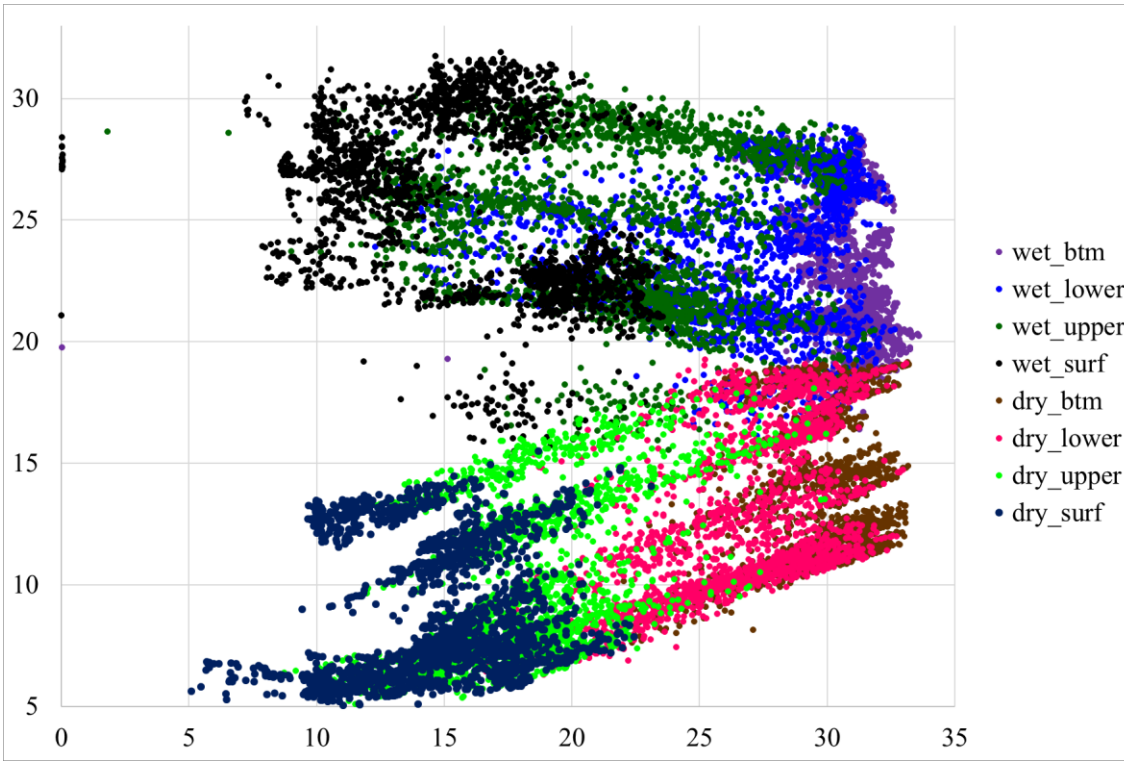

Figure 2.16 Temperature and salinity pairs measured at Nakaura Watergate monitoring station. Summer (winter) season clusters in the upper (lower) part of the diagram.

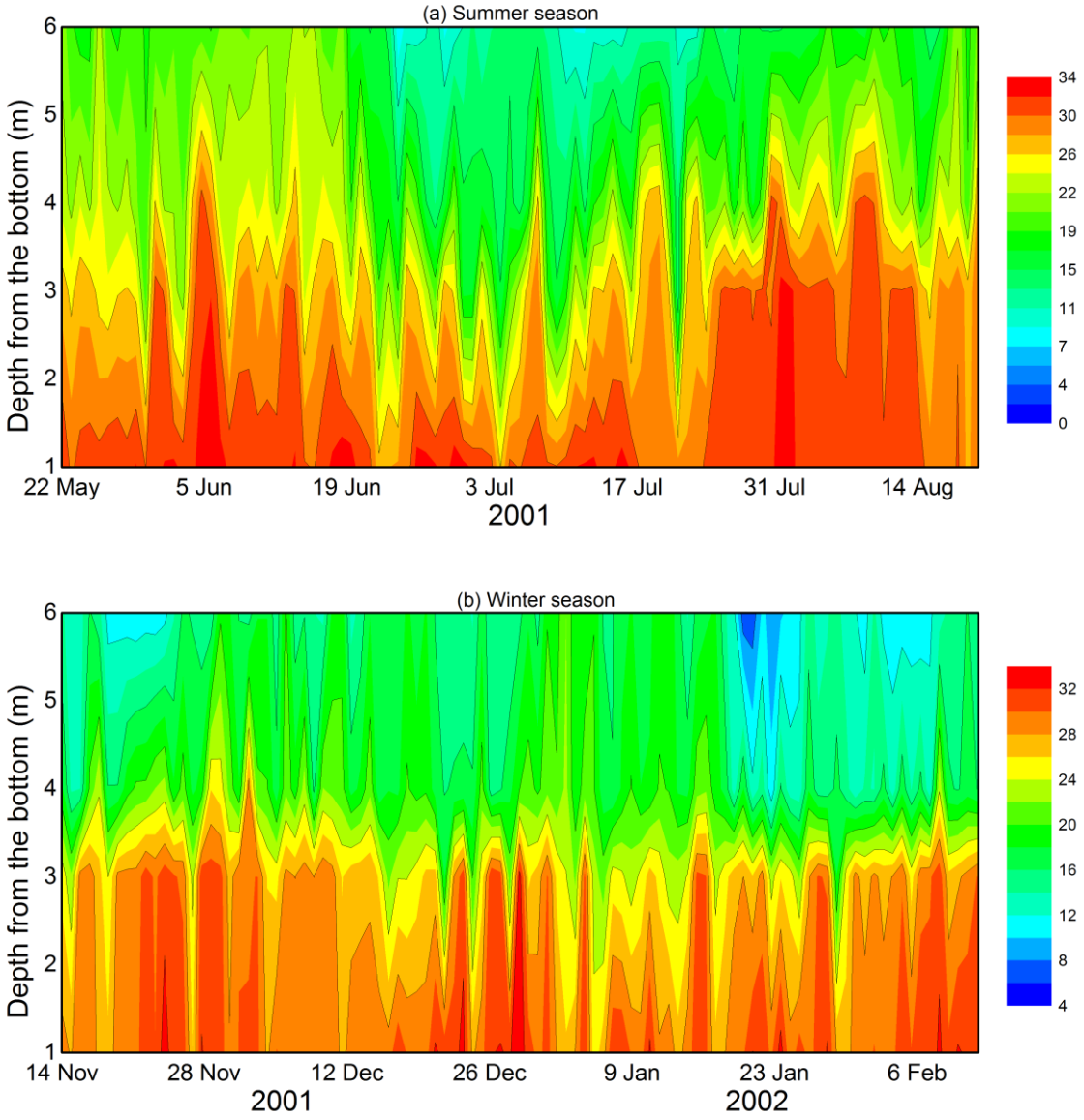

Figure 2.17 Vertical profile of salinity as a function of depth and time

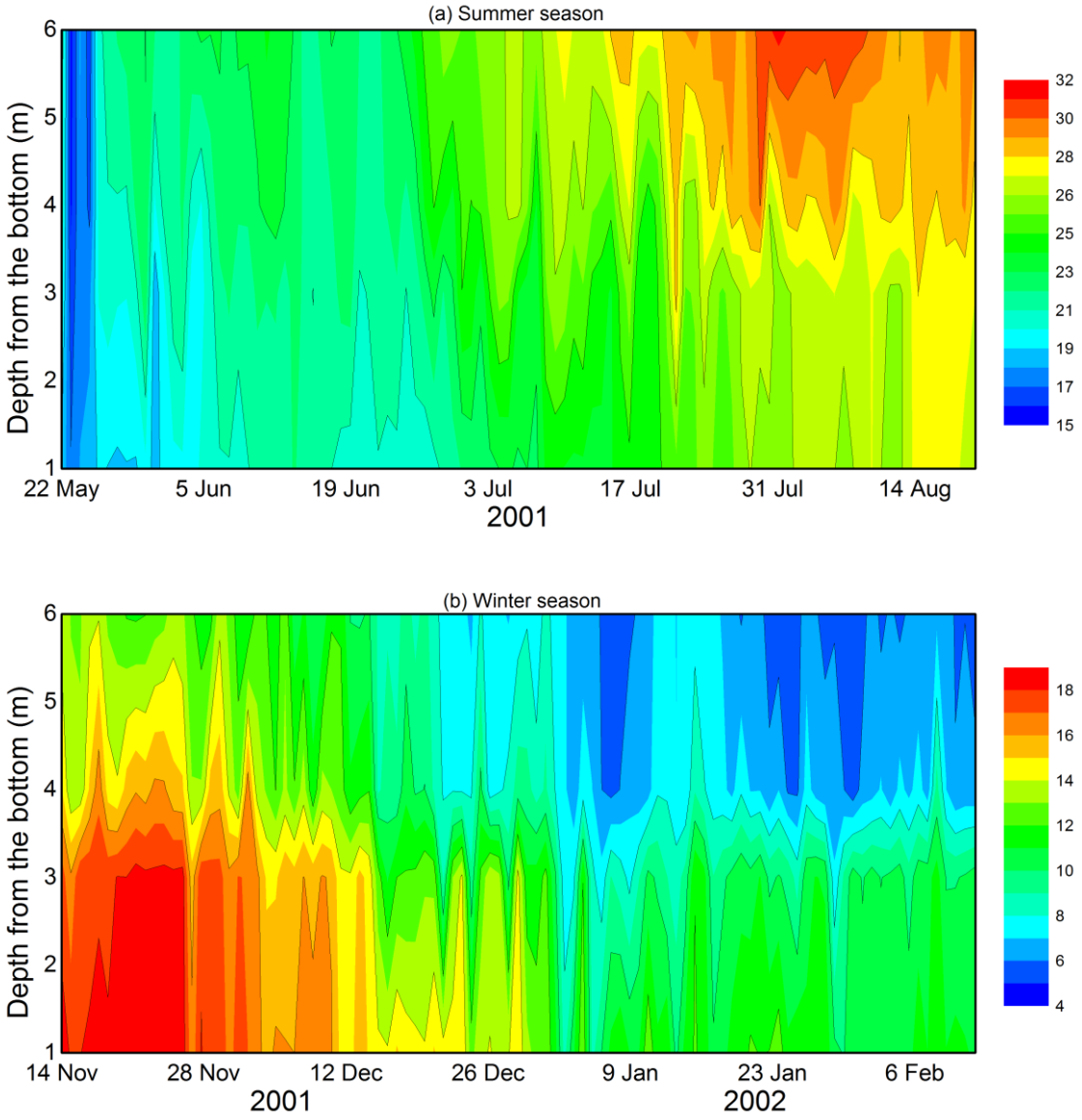

Figure 2.18 Vertical profile of water temperature as a function of depth and time

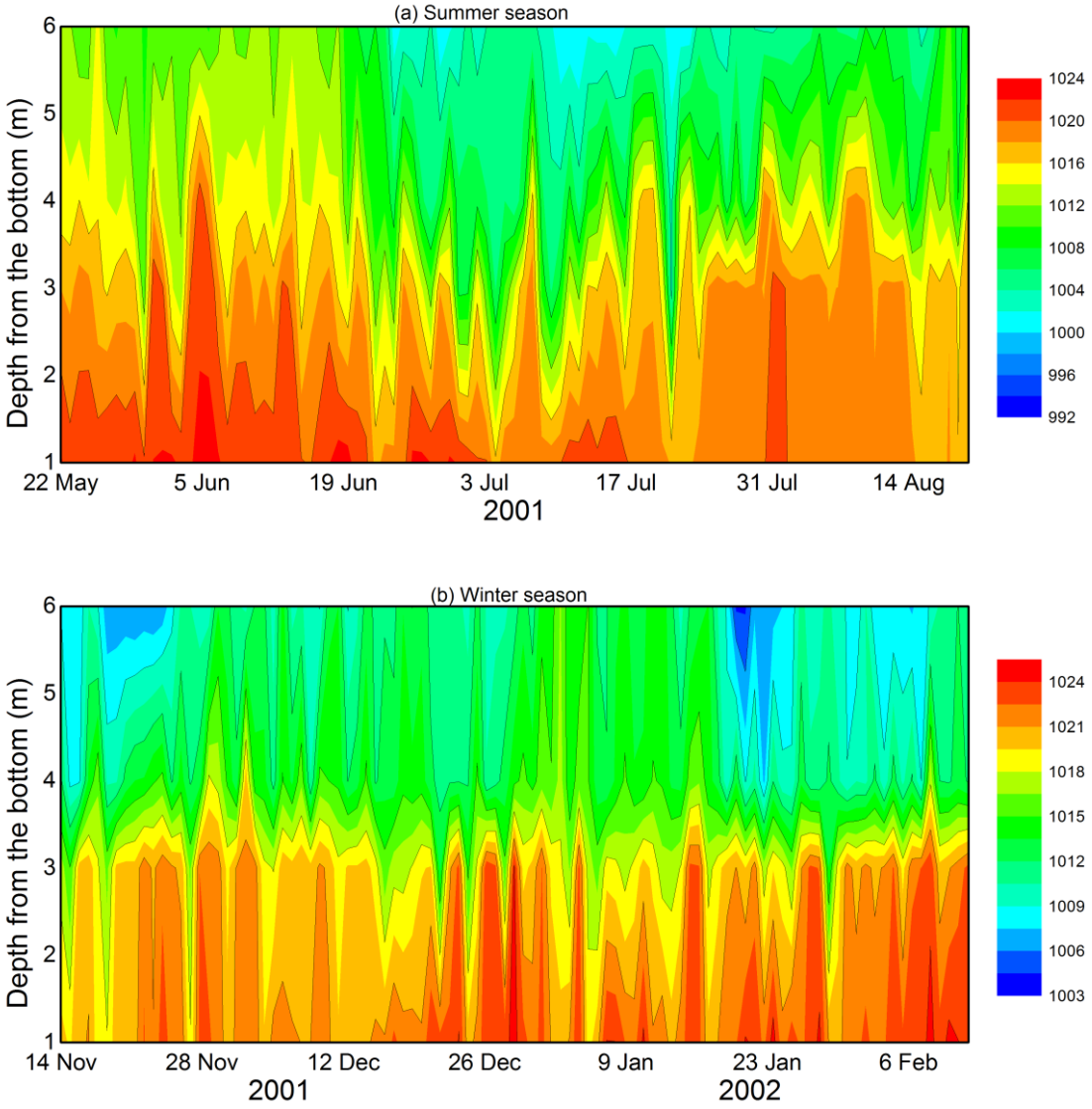

Figure 2.19 Vertical profile of calculated density as a function of depth and time

2.3.4 Salt Flux

The salt flux method presented in section 2.2.3 was used to compute the contributions of terms of equation (2-10) at Nakaura Watergate. Table 2-7 and Table 2-8 shows the mean and total salt flux obtained using equation (2-10), respectively. The results show that term (a) is the main contributor to the salt transport. The sum of all term

over the whole period is positive indicating a seaward (advective) salt transport mostly due to the tidally-averaged velocity induced by the river discharge.

Table 2-7 Mean salt flux at Nakaura Watergate (kg/m/s).

Term	Physical processes	Mean – influx	Mean – out flux	Mean	Standard Deviation
(a)	Freshwater discharge or residual velocity	-7651.83	12140.45	5039.54	13552.31
(b)	Stokes drift or progressive tidal wave transport	-450.05	326.85	-154.70	628.01
(c)	Topographic trapping	-556.60	864.76	426.68	941.75
(d)	Gravitational circulation, bathymetric tidal pumping, steady wind effect	-3849.11	937.44	-3732.60	2447.39
(e)	Tidal shear and unsteady wind effect	-132.26	108.26	-20.19	164.15
(f)	Tide dispersion via triple correlation	-6.80	5.28	-1.85	9.17
(g)	Net advection of cross correlation between salt and tide	-2.01	2.95	0.91	5.21
∑(a)-(g)		-9201.74	12038.16	1557.81	14397.48

Freshwater discharge or residual velocity, term (a) accounts for 39% and 91% of salinity flux into and out of Lake Nakaumi, respectively. Term (a) transport salinity out of Lake Nakaumi at an average rate of 12200 kg/m/s and into the lake at an average rate of 7650 kg/m/s. Stokes drift or progressive tidal wave transport, term (b) accounts for transport of salinity into and out of Lake Nakaumi at an average rate of 450 kg/m/s and 330 kg/m/s, respectively. Topographic trapping, term (c), accounts for 2.4% and 7% of salt flux in and out of Lake Nakaumi, respectively. Gravitational circulation, bathymetric tidal pumping, steady wind effect, term (d) transported an average of 3850 kg/m/s of salinity into Lake Nakaumi and 900 kg/m/s out of the lake. The average transport direction due to term (d) is into Lake Nakaumi at an average of 3740 kg/m/s. Tidal shear and unsteady wind effect contribution to salinity transport into and out of Lake Nakaumi

is about 1% and 0.6%, respectively. The average quantity being transported either direction is about 100 kg/m/s. Transport of salinity due to tide dispersion via triple correlation or net advection of cross correlation between salt and tide is negligible, less than 10 kg/m/s either direction.

Table 2-8 Total salt flux at Nakaura Watergate (kg/m/s).

Term	total influx		total out flux		Net flux
(a)	-6.77E+07	39.07%	1.92E+08	90.69%	1.24E+08
(b)	-6.87E+06	3.97%	3.06E+06	1.45%	-3.81E+06
(c)	-4.22E+06	2.44%	1.47E+07	6.97%	1.05E+07
(d)	-9.26E+07	53.45%	5.62E+05	0.27%	-9.20E+07
(e)	-1.74E+06	1.00%	1.24E+06	0.59%	-4.98E+05
(f)	-9.88E+04	0.06%	5.33E+04	0.03%	-4.55E+04
(g)	-2.04E+04	0.01%	4.28E+04	0.02%	2.25E+04
Σ(a)-(g)	-1.73E+08		2.12E+08		3.84E+07

Figure 2.20 and Figure 2.21 show salt transport plotted with river discharge, wind and atmospheric pressure during the summer of 2002 and 2003. Term (a) transport salt seaward under the influence of high river discharge, and generally westerly winds, e.g. around mid-July 2003 (Figure 2.21). The landward transport of salinity due to term (a) is mainly driven by easterly wind and atmospheric pressure drop, e.g. around September 1, 2002 (Figure 2.20). Term (b) alternates between positive (seaward) and negative (landward) transport of salt. In Sakai Channel, there is a progressive tidal wave component, though small, propagating back and forth. Term (b), the Stokes drift, is higher during the spring tides than in the neap tides. The tidal trapping, term (c) mainly contributes to the seaward salt transport. If the phase difference between the tidal (barotropic) components of current velocity, V_t and salinity, S_t is larger than 90°, term

(c) is seaward, a phenomena observed in two-layered estuaries with higher longitudinal salinity gradients in the in the upper layer than lower layer (Vaz et al. 2012). This leads to reduced tidal salinity oscillation in the lower layer with near bottom tidal current leading upper layer tidal current.

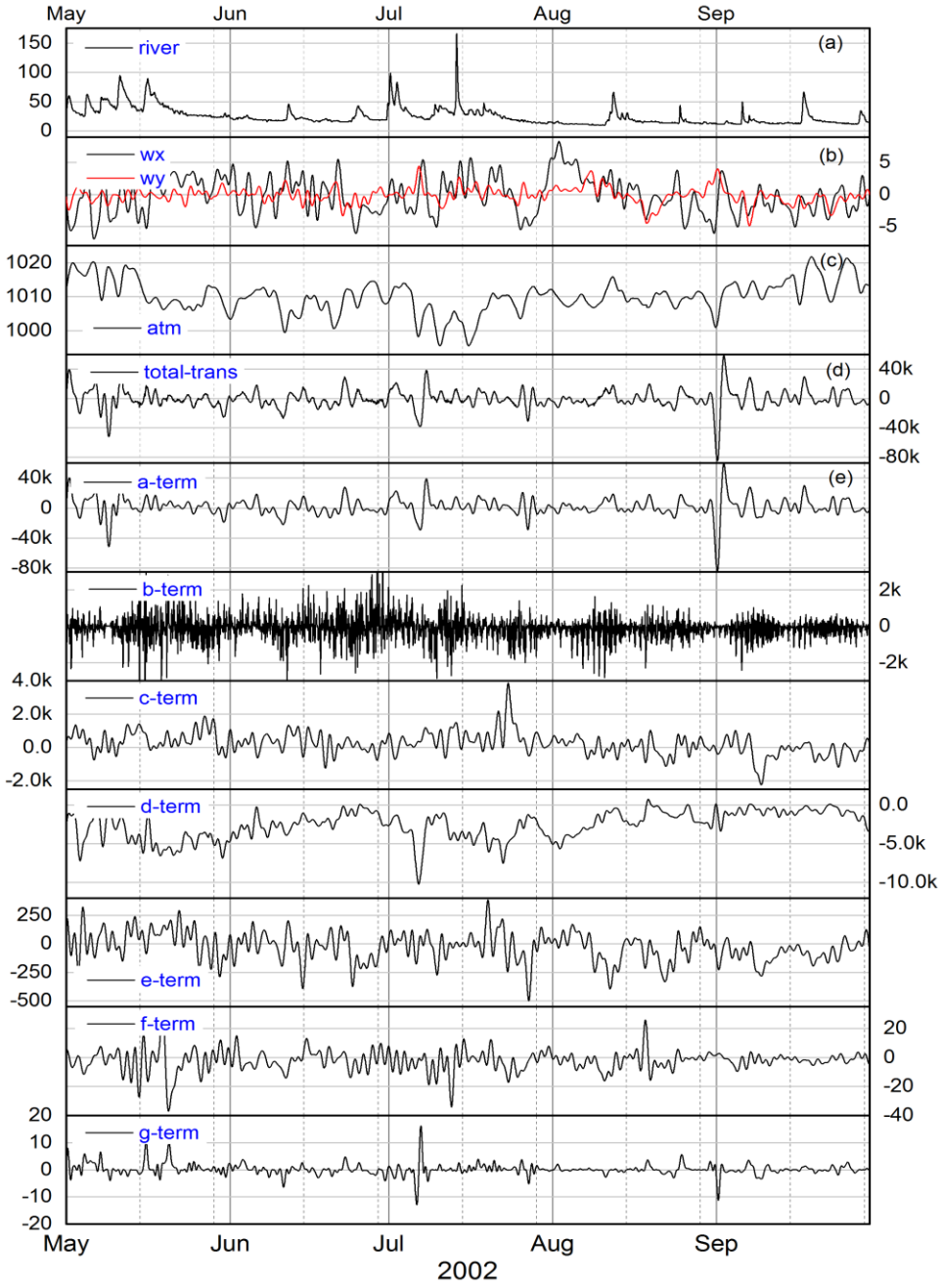

Figure 2.20 (a) River discharge, (b) wind speed, (c) atmspheric pressure, (d) total salt transport and (e) salt transport due to terms (a) – (g) during summer of 2002

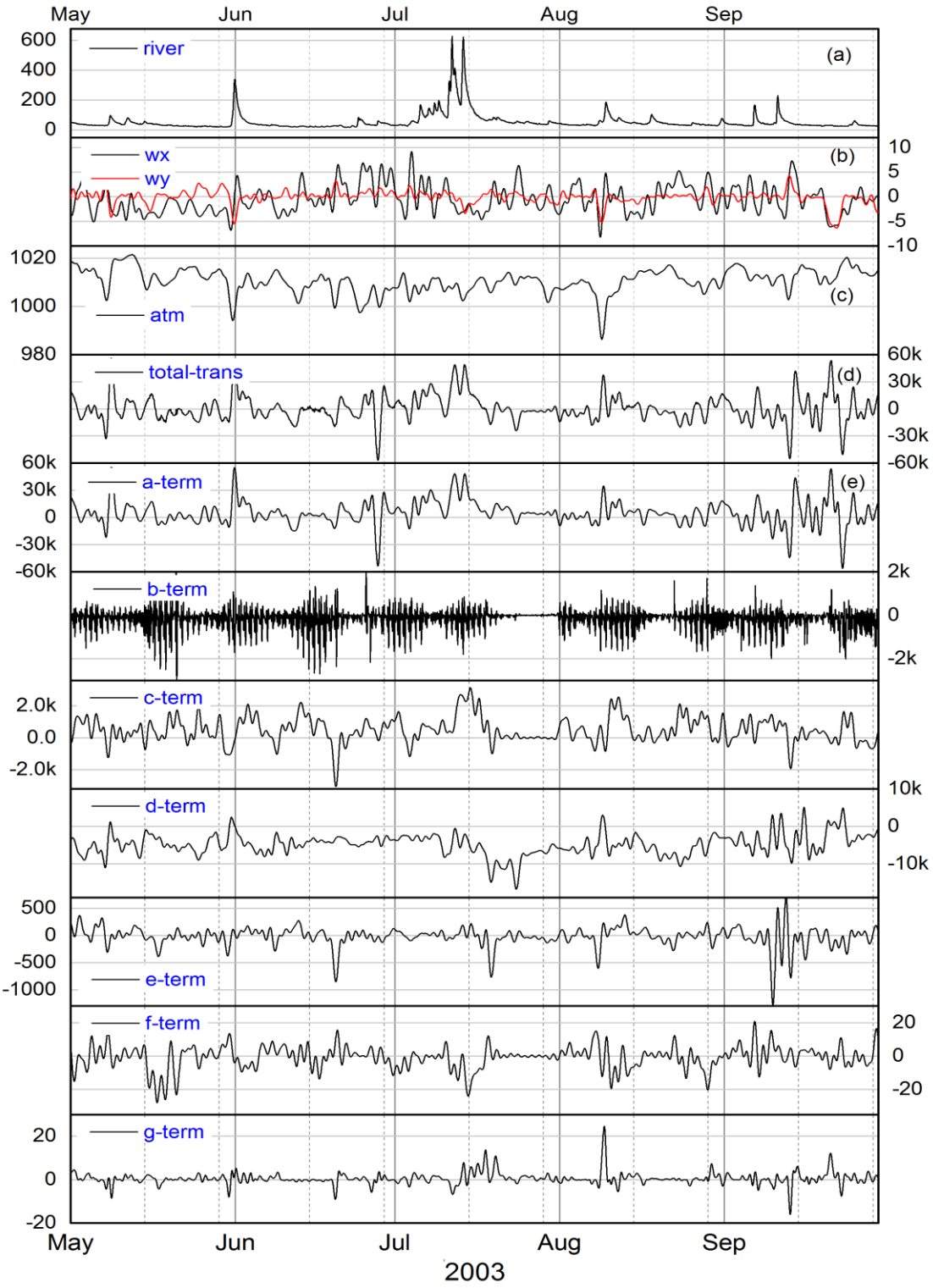

Figure 2.21 (a) River discharge, (b) wind speed, (c) atmspheric pressure, (d) total salt transport and (e) salt transport due to terms (a) – (g) during summer of 2003

2.4 CONCLUSIONS

Sakai Channel is a partially stratified channel, with large freshwater input from Hii River generating gravitational circulation along the channel, strengthened during the summer season. Seaward-directed subtidal flows occur in upper part (about 60%) of the water column. Although the subtidal flow is stratified, the flow sometimes became unidirectional mainly towards the Japan Sea due to a combination of increased river discharge and other factors such as increased turbulent mixing and weaker density gradients. The tidal period in this channel is asymmetrical, with the ebb period shorter than the flood period. The speed of the ebb current is thus higher than that of the flood current. The ebbing current dominate the current field. This may lead to a heavy downstream transport of suspended matter and solutes. Generally, materials in the lower half of the water column are transported into Lake Nakaumi and may remain there as the flows are stratified. A numerical simulation of whole system may shed light on other important circulation patterns.

Freshwater discharge or residual velocity transport almost all salt out of Lake Nakaumi at 5000 kg/m/s. Gravitational circulation, bathymetric tidal pumping, steady wind effect is responsible for more than half of the salt being transported into Lake Nakaumi at a rate of 3700 kg/m/s. There is net removal of salinity from Nakaumi (1550 kg/m/s). Freshwater discharge or residual velocity transport almost all salt out of Lake Nakaumi and a significant quantity into the lake

3 CHARACTERISTICS OF SALINITY FLUX

3.1 INTRODUCTION

Saline water intrusion process plays an important role in the ecosystems of estuaries and brackish water lakes. Salinity level and its fluctuation control dominant species in the pelagic and benthic ecosystems and thus alter structures of ecosystem. Saline water intrusion also affects water quality variations through formation of density stratification. Water exchange process is crucial for understanding of ecosystems and management of water quality in brackish water lakes. Water exchange between the Japan Sea and the couple brackish lake system of Lakes Shinji and Nakaumi, results in density stratification and hence the formation of oxygen-depleted water in the bottom layer during summer. The Sakai Channel is a major outlet of this coupled lake system, and seawater intrusion in this channel has seriously affected the habitat of aquatic species. During the summer, the vertical salinity gradient increases leading to anoxic bottom waters. Previous studies found that meteorologically induced sea surface variation (MISSV) and large periodic river discharge to be effective water exchange mechanism between the Japan Sea and Lakes Nakaumi and Shinji (Nakata et al. 2000). Tidal amplitude on the Japan Sea is small; hence, astronomical tides are not considered an effective water exchange mechanism. Meteorological forcing variables, e.g. atmospheric pressure and wind stress are also potential seawater intrusion mechanism. Salinity variation in Lakes Shinji and Nakaumi exhibits high correlations with the sea surface variation and river discharge (Nakata et al. 2000). However, the dynamic characteristic of salinity intrusion, and the effects of tide, river discharge and meteorological forcing variables on the salinity flux are unclear.

Wavelet analysis has been applied to the marine science, meteorological and hydrological fields so as to analyse non-stationary time series water quality data as well as meteorological data (Liu et al. 2014; Parmar & Bhardwaj 2013; Ng & Chan 2012; Zhang et al. 2009; Somoza et al. 2013; Ideião & Santos 2005; Sovi et al. 2012; Briciu 2014; Torrence & Compo 1998). Wavelet analysis has already been used to study salinity intrusion and river water quality parameters (Liu et al. 2014; Parmar & Bhardwaj 2013). However, most authors who applied wavelet analysis to study geophysical processes rely on univariate and bivariate wavelet analysis. Since salinity intrusion is influenced by more than one variable, the assessment of its association with any of the variables requires the consideration of its interaction with other variables. However, to the best of our knowledge, specifically about salinity intrusion dynamics, there is no previous work, which applied multivariate wavelet analysis. In order to assess the relationship between two-time series, it is important to remove the influence of other time series. Partial wavelet coherence (PWC) and partial phase-difference (PPD) enable the elimination of the influence of other time series, giving a clear estimation of the relationship between two-time series of interest.

Therefore, in order to understand the non-linear characteristics of salinity intrusion in Sakai Channel and quantify the relationships between river discharge, tide and meteorological forcing variables and salinity intrusion, this study applied the recent wavelet analysis techniques – PWC and PPD – to study the effects of river discharge, tide level and meteorological forcing variables on the salinity flux. Continuous Wavelet Transform (CWT) was used to analyse the period characteristics of tide level, river discharge, meteorological forcing variables and salinity flux.

3.2 MATERIALS AND METHODS

3.2.1 Study area

Lakes Shinji and Nakaumi form a coupled brackish lake system in the western part of Japan. Lake Shinji has an average depth of 4.5m, surface area of 80km^2 and volume of 0.366km^3. Lake Nakaumi has an average depth of 5.4m, surface area of 86.2km^2 and volume of 0.47km^3. The Ohashi River (7.0km long) connects the two lakes and the Sakai Channel (7.5km long) connects Lake Nakaumi to the Japan Sea. The Hii River at the west end of Lake Shinji supplies this coupled brackish lake system with most of its fresh water. Lake Shinji is a mesohaline lake with average salinity between 1 and 6 psu. Lake Nakaumi has a strongly differentiated two-layer system, salinity of the surface water is 14-20 psu and that of the bottom layer is 25-30 psu. Salinity in this lake system shows a seasonal variation, a marked horizontal gradient as well as vertical stratification mainly in Lake Nakaumi (Uye et al. 2000). Hence, these brackish lakes are stably stratified due to salinity (density) differences and density gradients have a large impact on water movement in this system (Okuda 2004; Mizoyama et al. 2011).

Seawater from the Japan Sea, through Sakai Channel, enters Lake Nakaumi along the bottom of the lake to the mouth of Ohashi River forming the bottom layer. Brackish water from Lake Shinji flows into Lake Nakaumi through Ohashi River forming the surface layer. Bottom layer high salinity water in Nakaumi is driven by the internal waves towards the lake coast and upstream into Ohashi River and Lake Shinji. The effect of wind stress on internal oscillation is greater than that of astronomical tides. However, at Nakaura Watergate, due to the orientation of the channel, the predominantly westerly winds have less effect (Fujii & Okuda 2004).

The average water transport direction in Ohashi River is eastward, from Lake Shinji to Lake Nakaumi. This eastward water transport approximately equals the freshwater inflow into Lake Shinji, mainly from the Hii River (Nakata et al. 2000). The westward water transport, mainly driven by MISSV, occurred often with the time scale over a few days to a week, contributing to the exchange of water between the two lakes (Nakata et al. 2000). The salinity in Ohashi River, between Lakes Shinji and Nakaumi, vary acutely as a result of water moving back and forth with tides, freshwater input and other physical factors (Uye et al. 2000).

3.2.2 Observations

Salinity and current velocity data used in the study was collected at Nakaura Watergate monitoring station (insert, Figure 2.1). Nakaura Watergate (width 414m, depth 6.8m) had five floodgates on the east and on the west (each 32m wide), and three floodgates at the centre. On the western pile of the 3rd east side floodgate (indicated by red arrow, Figure 2.1), submerged water pumps were installed for water sampling at 1, 2, 4 and 6m from the bottom and the water pumped to acrylic boxes in the floodgate administration building, where water temperature, electrical conductivity and dissolved oxygen were measured every thirty minutes using custom-made sensors (Alec Electronics Co., Ltd.). Salinity was then calculated from electrical conductivity. Acoustic Doppler Profiler (Nortek ADP) was also installed in the centre of the 3rd floodgate on the eastern side of the Nakaura Watergate (indicated by red arrow, Figure 2.1), near the bottom. Current velocity measurements were taken every half hour at depth intervals of 0.5 m, from 1 m to 6 m above the bottom. Along-channel current vector component is used in this study. Positive along-channel velocities were ebb directed (northward flow), whilst

negative values were associated with southward (flood) flow. The orientation of Nakaura Watergate was in the east-west direction and the direction of flow at this location is almost south–north, that is, ebb tidal current is northwards and flood tidal current southwards.

Continuous measurements of salinity over a period of six years (February 1998 to March 2004) is available, although there are periods with missing data. Long-term continuous measurements of hydrodynamic and water quality data in the Sakai Channel before the construction of Nakaura Watergate and after its removal do not exist. Salinity, water temperature, current velocity and water level data during the summer of 2002 (June to September 2002) was used to calculate salinity flux per unit width in this study. High saline water intrusion during the summer season is important for water quality deterioration; as it directly cause salinity stratification and enhance oxygen depletion in the bottom layer (Nakata et al. 2000). Also this the period has least missing data. The salinity, water temperature, current velocity and water level data was averaged to one-hour intervals to match the intervals of the meteorological data used in the analysis. One-hour interval meteorological data (atmospheric pressure, wind speed and direction) was collected at Matsue Meteorological Station (available on Japan Meteorological Agency website, http://www.jma.go.jp/jma/index.html). The wind was treated as a mathematical vector, and the mathematical convention for the direction was used, i.e., wind direction was converted from "meteorological direction" to "math direction". The wind vector was resolved into its *x* and *y* components. Wind from the west positive W_x, and from the south a positive W_y. Tidal data used in the study was recorded at Sakai Tide Station maintained by Japan Meteorological Agency (http://jdoss1.jodc.go.jp/cgi-bin/1997/tide_data?MA53). River discharge was recorded in Hii River at Nadabun

gauging station (available on Japan's water information system website, http://www1.river.go.jp/).

3.2.3 Methodology

3.2.3.1 Salinity Transport

Instantaneous advective salt transport (M_s, $\mathrm{kgm^{-1}s^{-1}}$) per unit width of a section, normal to the longitudinal flow of the channel, is given by the following expression (Vaz et al. 2012; Moser et al. 2005):

$$M_s = \int_0^h \rho V S dz = \overline{\rho V S} \cdot h \tag{2-4}$$

where ρ is the density, V is the longitudinal velocity component, and S is the longitudinal salinity. The upper bar denotes averaging over the total depth of the water column, h.

The density of water was calculated using the following approximate density formula neglecting pressure (shallow lake) (Klinger n.d.):

$$\rho = 999.83 + 0.808S - \alpha(T)T - \gamma(T)(35 - S)T \tag{2-11}$$

$$\alpha = 0.0708(1 + 0.068T) \tag{2-12}$$

$$\gamma = 0.003(1 - 0.012T) \tag{2-13}$$

where T is temperature in °C and S is salinity in PSU.

3.2.3.2 Continuous Wavelet Transform (CWT)

CWT decomposes a time series into a time-frequency space and determines both the dominant modes of variability and their variation with time (Torrence & Compo 1998). The wavelet is applied as a bandpass filter to the time, stretching it in time by varying its scale(s) and normalizing it to have unit energy (Grinsted et al. 2004; Zhang et al. 2009).

A wavelet $\psi(t)$ is a function that oscillates around the *t*-axis and looses strength as it moves away from the centre, behaving like a small wave (Torrence & Compo 1998). Beginning with a mother wavelet ψ, a family of "daughter wavelet", $\psi(\tau, s)$ is computed by scaling and translating ψ:

$$\psi_{\tau,s}(t) = \frac{1}{\sqrt{|s|}}\psi\left(\frac{t-\tau}{s}\right);\ s, \tau \in \mathbb{R}; s \neq 0 \qquad (3\text{-}1)$$

where $\psi(t)$: mother wavelet, $\psi_{\tau,s}(t)$: daughter wavelet, *t*: a non-dimensional "time" parameter, *s*: a scaling or dilation factor that controls the width of the wavelet, τ: a translation parameter controlling the location of the wavelet.

This study used the Morlet wavelet, which consists of a plane wave modulated by a Gaussian or in other words, a complex exponential function multiplied by a Gaussian window. Hence represents the best compromise between frequency and time localization. A complex wavelet is essential for this study, as it yields a complex transform, with information on both the amplitude and phase, crucial to study the synchronization of oscillations between different time-series (Sousa 2014; Aguiar-Conraria & Soares 2014). Morlet wavelet is defined as:

$$\psi_0(t) = \pi^{-1/4} e^{i\omega_0 t} e^{-t^2/2} \quad (3\text{-}2)$$

where $\psi_0(t)$: the Morlet wavelet, ω_0: wavenumber, gives the number of oscillations within the wavelet itself

CWT of a time series $x(t) \in L^2(\mathbb{R})$, with respect to the wavelet ψ is a function of two variables, $W_{x;\psi}(\tau, s)$:

$$W_{x;\psi}(\tau, s) = \int_{-\infty}^{\infty} x(t) \frac{1}{\sqrt{|s|}} \psi^* \left(\frac{t-\tau}{s}\right) dt \quad (3\text{-}3)$$

where $W_{x;\psi}(\tau, s)$: CWT of a time series $x(t)$, $L^2(\mathbb{R})$: denotes the set of square integrable functions, i.e. the set of functions defined on the real line and satisfying $\int_{-\infty}^{\infty} |x(t)|^2 dt < \infty$, ψ^*: complex conjugation of ψ

3.2.3.3 Partial wavelet coherence

CWT is increasingly being used in the analysis of marine sciences time series data. However, most of the CWT analysis has been limited to univariate and bivariate analysis, i.e., the wavelet power spectrum, the wavelet coherency and the wavelet phase-difference (Aguiar-Conraria & Soares 2014). Wavelet analysis tools have already been extended to allow for multivariate analyses (Ng & Chan 2012; Aguiar-Conraria & Soares 2014). PWC and PPD are the examples of recent wavelet analysis techniques. The PWC technique is similar to partial correlation and it identifies the resulting wavelet coherence between two time series after eliminating the influence of their common dependence (Ng & Chan 2012). The applicability of PWC to geophysics was demonstrated during the study of the

‘‘stand-alone’’ relationship between the “ratio of number of typhoons to number of tropical cyclones” and “large-scale atmospheric factors” after removing the effect of El Nino–Southern Oscillation (ENSO) (Ng & Chan 2012).

The squared multiple wavelet coherence ($R^2_{1(23\ldots p)}$) between the series x_1 and all the other series $x_2,\ldots, x_\mathrm{p}$ is given by the formula

$$R^2_{1(23\ldots p)} = 1 - \frac{C^d}{C^d_{11}} \tag{3-4}$$

where C: denote the $p \times p$ matrix of all the complex wavelet coherencies ϱ_{ij}, i.e. $\mathrm{C} = \left(\varrho_{ij}\right)_{i,j=1}^{p}$, $C^d = \det C$

The complex partial wavelet coherence ($\varrho_{1j.q_j}$) of x_1 and x_j $(2 \le j \le p)$ allowing for all the other series is given by

$$\varrho_{1j.q_j} = -\frac{C^d_{j1}}{\sqrt{C^d_{11}}\sqrt{C^d_{jj}}} \tag{3-5}$$

The partial wavelet coherence ($R_{1j.q_j}$) of x_1 and x_j allowing for all the other series, is defined as the absolute value of equation (3-5), i.e.

$$R_{1j.q_j} = \frac{\left|C^d_{j1}\right|}{\sqrt{C^d_{11}C^d_{jj}}} \tag{3-6}$$

and the *squared partial wavelet coherence* of x_1 and x_j allowing for all the other series, is simply the square of $R_{1j.q_j}$.

The partial phase-delay (phase-difference) of x_1 and x_j, given all the other series is defined as the angle of $\varrho_{1j.q_j}$. A complex wavelet function contains information about both the amplitude and the phase, making makes it suitable to capture oscillatory behaviour. Complex partial wavelet coherence, $\varrho_{1j.q_j}$ considered can be separated into its real part, $\Re\left(\varrho_{1j.q_j}\right)$ and imaginary part, $\Im\left(\varrho_{1j.q_j}\right)$ or in its amplitude, $\left|\varrho_{1j.q_j}\right|$, and phase angle $\phi_{1j.q_j}$. The phase-difference, $\phi_{1j.q_j}$

$$\phi_{1j.q_j} = Arctan\left(\frac{\Im\left(\varrho_{1j.q_j}\right)}{\Re\left(\varrho_{1j.q_j}\right)}\right) \tag{3-7}$$

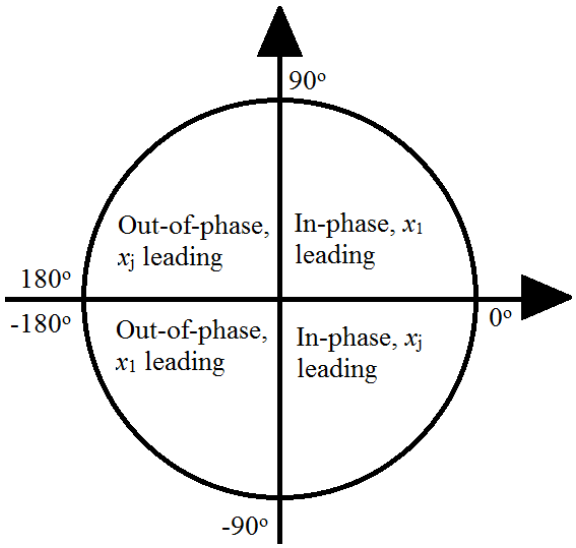

Figure 3.1 Phase Difference Circle

A phase-difference of zero indicates that the time series move together at the specified time-frequency; if $\phi_{x_1x_j}\epsilon(0,90)$, the series move in phase and the time series

of x_1 leads x_j; if $\phi_{x_1 x_j} \epsilon (-90,0)$, then x_j leads x_1. A phase-difference of 180 (or −180) indicates an antiphase relationship; if $\phi_{x_1 x_j} \epsilon (90,180)$, then x_j leads x_1; if $\phi_{x_1 x_j} \epsilon (-180,-90)$, then x_1 leads x_j (see Figure 3.1). Phase difference can be converted into instantaneous time-lag between two-time series by dividing the phase-difference, $\phi_{1j.q_j}$ by the angular frequency corresponding to the scale s, $\omega(s)$

1.1.1 Significance tests

The assessment of the statistical significance of the wavelet power spectrum and the wavelet coherence results is important. Monte Carlo methods were used to assess the statistical significance levels and confidence intervals against red noise backgrounds. Other researchers indicated that there are no good statistical tests for the wavelet phase-difference hence significance tests should not be used for the phase-difference. It was recommended that inspection of the coherence significance should be used to complement phase-difference analysis (Aguiar-Conraria & Soares 2014).

3.3 RESULTS AND DISCUSSION

3.3.1 Analysis of period characteristics using continuous wavelet transform

The analysis variables and their wavelet power spectrum are shown in Figure 3.2 to Figure 3.6. The intensity of the wavelet power shows the time series variance for each moment of time and each frequency of oscillations. Figure 3.2 **(a)** show the salinity flux per unit width at Nakaura Watergate. Positive values indicate flux towards the Japan Sea and negative towards Lake Nakaumi. The CWT coefficient chart for salinity flux (Figure 3.2 **(b)**) has stable period characteristics, with high power oscillations in the 0.5-day and

1-day period bands, as indicated by the white lines. Both the red colour and the black contour indicates that cycles are strong and statistically significant at 95% confidence level (hereinafter statistically significant). Also observed is a relatively strong, though not statistically significant, 2-4-day period cycle that occurs in first week of September. This behaviour coincides with the statistically significant oscillations for tide level shown in Figure 3.3. From mid-June to mid-July and end of August, there was change in salinity flux and this possess an 8-day period.

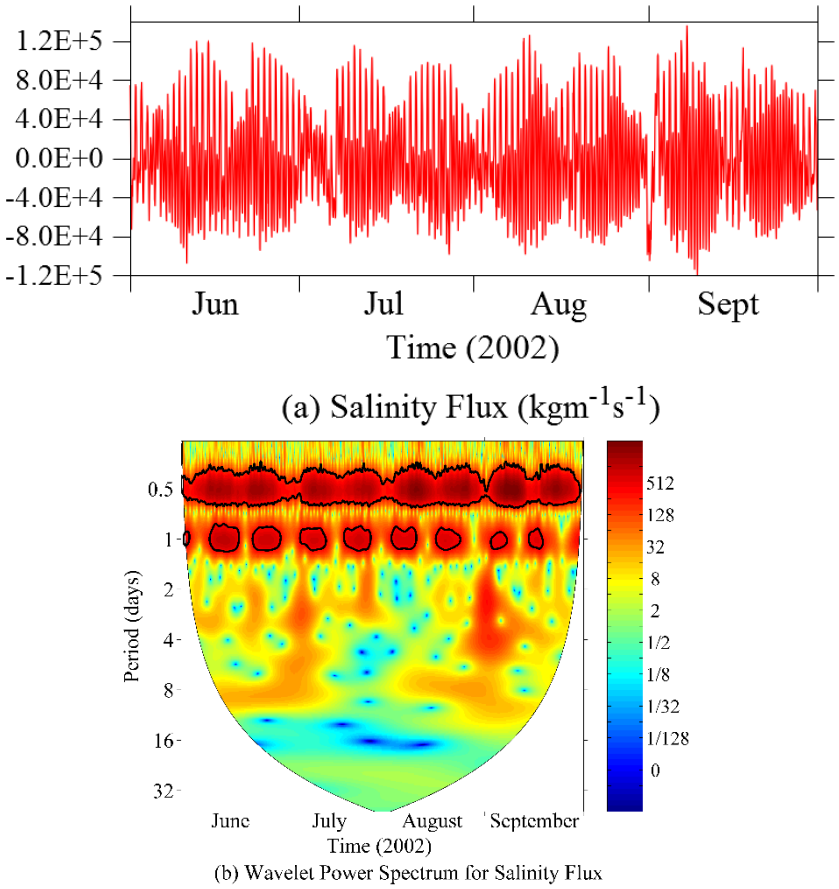

Figure 3.2 The time series of salinity flux and its wavelet power spectrum. The black contour designates 95% confidence level, using red noise as background spectrum. White regions on either end indicate the "cone of influence" where edge effects become important.

Figure 3.3 shows time series plot and CWT coefficient chart for the tide level showing continuous and fluctuating low and medium power oscillations appearing around 0.5 and 1 day periods, respectively. These oscillations appear twice a month, which means spring-neap tide variations. Even for the power with half day or one day variation, phenomenon with longer periodicity and its variations can be visible. The tide level has statistically significant periods of half a day and one day. This implies considerable power spreads throughout the semi-diurnal and diurnal bands in summer.

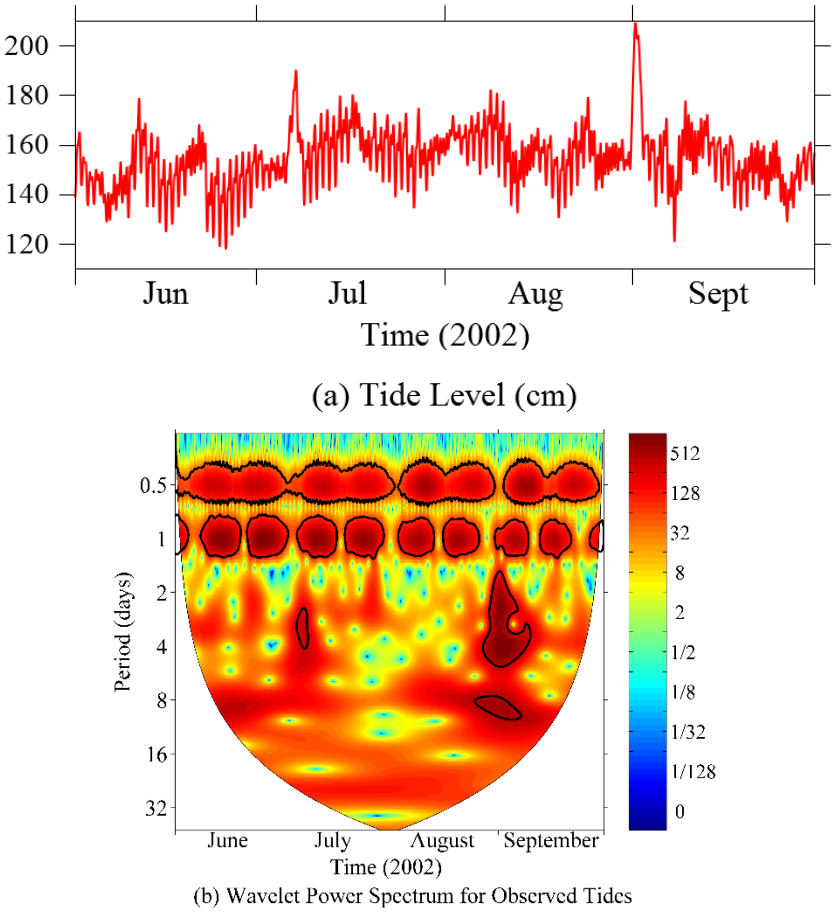

Figure 3.3 Tide Level - time-series plot and time-series wavelet power spectrum.

Figure 3.3 also indicates high power oscillations when the tide level increased and dropped end of August to early September. This increase and drop maybe a result of the

influence of meteorological forcing variables such as wind or atmospheric pressure. Though not statistically significant, time series plot and CWT coefficient chart indicate impulsive increases in tide level appearing several times in mid-June, early July, and the beginning of September. Such changes seem to be corresponding to sudden drop in atmospheric pressure (Figure 3.5). The latter two events seem to be corresponding to increased salinity transport, however, such events which occur at random with shorter duration are not well reproduced by the wavelet analysis. This indicates a possible weakness of the wavelet analysis, a situation whereby intrusion processes are not always fully described.

Figure 3.4 show time series plot and CWT coefficient chart for the river discharge, which shows that the river discharge wavelet coefficients vary from the highest to the lowest indicating a highly irregular river discharge. The chart also shows distinct character that has long vertical peaks like a rain drop which indicate that the period of oscillation varies from high to low almost instantaneously. Each peak of energy corresponds to high river discharge and its slower decrease in flow rate. From the time series plot and CWT coefficient chart, it is evident that highest river flow rate occurs between mid-June and mid-July. The white line indicates a strong and statistically significant 10-day period cycle during this period. There are also discontinuous and regular relatively high river discharges in August and September. The irregularity of Hii River discharge may be attributed to non-stationary rainfall and water releases upstream. The increased river discharge in July resulted in increased sea surface elevation in Sakai Channel (Figure 3.3).

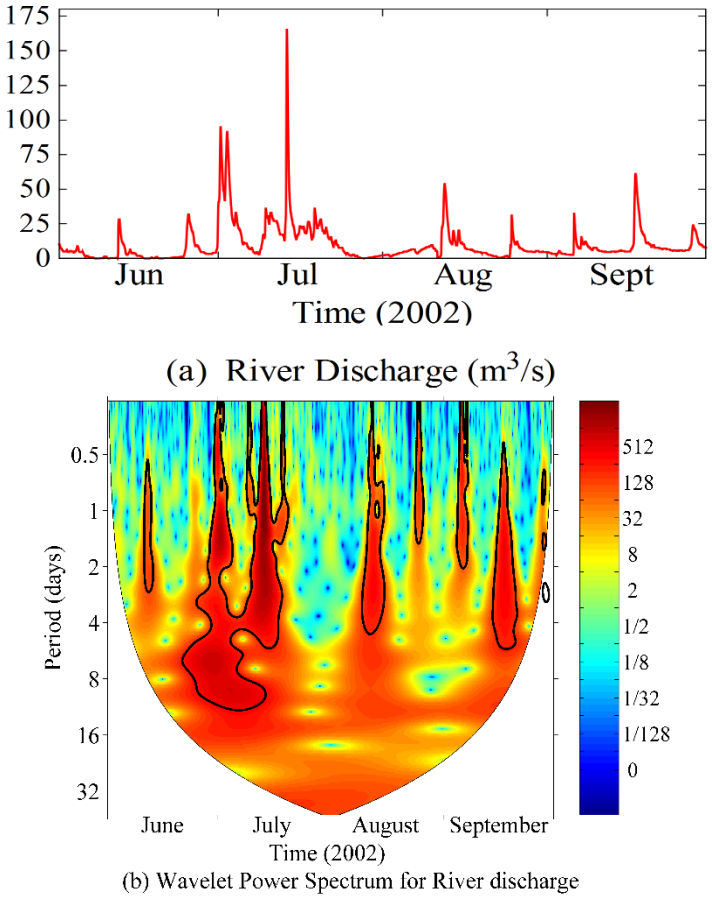

Figure 3.4 River discharge - time-series plot and time-series wavelet power spectrum.

The CWT coefficient chart for the atmospheric pressure (Figure 3.5 **(b)**) shows continuous statistically significant medium power 4 to 8-day period cycles throughout the analysis period. Continuous low power oscillations are observed in the 0.5-day band. There are also discontinuous and irregular medium power oscillations possessing a 1-day period. The time series plot indicates a statistically significant decrease in pressure in mid-June, mid-July and beginning of September. This pressure drop resulted in increased sea surface elevation as shown in Figure 3.3 and increased salinity intrusion into Lake Nakaumi as shown in Figure 3.2. The sharp decrease in pressure is captured as a strong and statistically significant 32-day period cycle. A yellow region is spotted towards end of September capturing the increase pressure during this period.

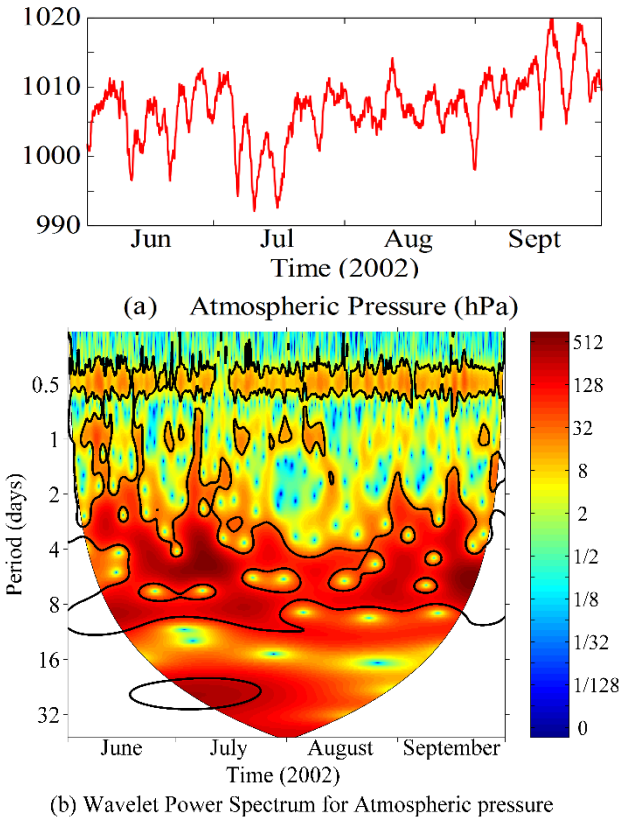

Figure 3.5 Atmospheric pressure - time-series plot and time-series wavelet power spectrum.

The CWT coefficient charts for wind vectors (Figure 3.6) show that stable statistically significant high power oscillations appear at longer periods, 8-32-day period band. The West-East wind component shows irregular fluctuating medium power in the 1-day period band in June, July and August. Strong and statistically significant 8, 16 and 32-day period cycles are observed. The West-East wind component also show a 4-day medium power cycle occurring early June, mid-July and end of August (Figure 3.6**(b)**). The South-North component also show occurrences of medium power oscillations with a 4-day period during mid-June and early of September (Figure 3.6**(c)**). Medium power oscillations are also observed in the 8-day period (mid-June to mid-July, and mid-August to mid-September) and in the 32-day band. Statistically significant high power wind variation occurred in August centred in the 24-day period cycle. Generally, the strong

wind variation was observed mainly in the west-east component during the month of July. From mid-August to early September, the south-north component dominated. From early August to mid-August the variation in both components was strong and statistically significant.

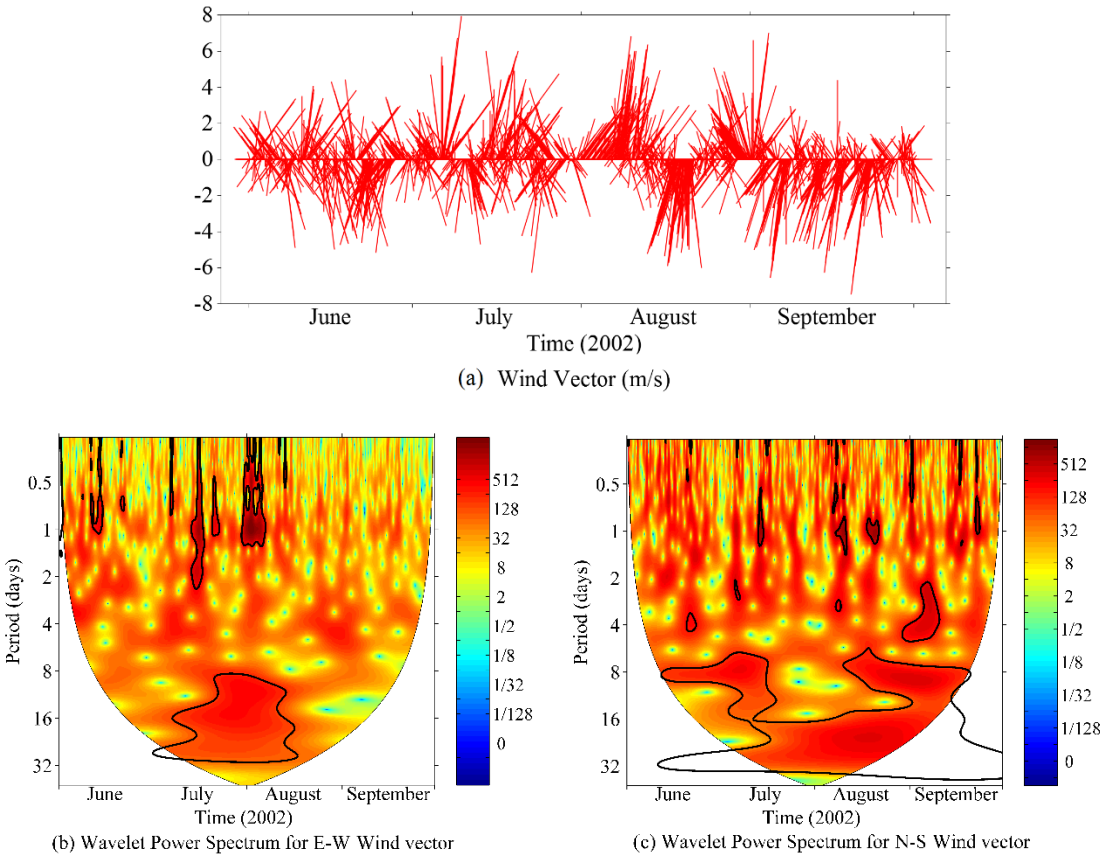

Figure 3.6 Wind vector - time-series plot and time-series wavelet power spectrum.

3.3.2 Analysis of dynamic characteristics using partial wavelet coherence

Partial coherence and partial phase-difference, described above, are used to estimate the interdependence, in the time-frequency domain, between two series after eliminating the influence of other series. Figure 3.7 to Figure 3.11 shows the interdependence, in the time-frequency domain, between salinity flux and each of the forcing variables, after eliminating the effect of other variables. The partial phase difference is the average partial

phase difference for each frequency band. It is possible to calculate the phase difference for each frequency. In this study, three frequency bands (1/2 - 4 day, 5-16 day, and 17-32 day) were chosen because the oscillations of all the variables were almost divided among these frequency bands. Table 3-1 shows mean phase difference and mean lag time with forcing factors leading for both in-phase and out-of-phase situations. Figure 3.8 shows the general ratio of occurrences when tides and river discharge were in-phase or out-of-phase, leading or lagging salinity transport.

3.3.2.1 Correlation between tides and salinity flux

Figure 3.7 shows extensive statistically significant power sections at the 5% level, indicating the existence of correlation between observed tides and salinity transport. The centre of power sections focuses on periods 12 hours and 1-day. Figure 3.7**(b)** shows that relationship between tides and salinity flux is typically between 0° and 180°, indicating that the variables are sometimes in-phase (positive correlation), with tides leading. Sometimes tides and salinity flux are out-of-phase, with tides lagging. Most of the time tides have a positive impact on salinity flux, over the periods 12 hours and 1-day. This implies that short-term salinity transport is highly influenced by tides. Tides also have statistically significant positive correlation with salinity flux in the 15-day period band in June and August, this could be the result of spring tides. In August and September, there positive relationship between salinity flux and tides centred around 20-day period. Almost half the time, salinity flux and tide level are in-phase with salinity flux leading (Figure 3.8**(b)**). Table 3-1 shows that tide level is usually in-phase and earlier than salinity flux by an average of 2.3 days. When salinity flux and tide level are in-phase with salinity flux leading (typically 0.5 and 1-day period bands), the mean time lag is 0.7 days.

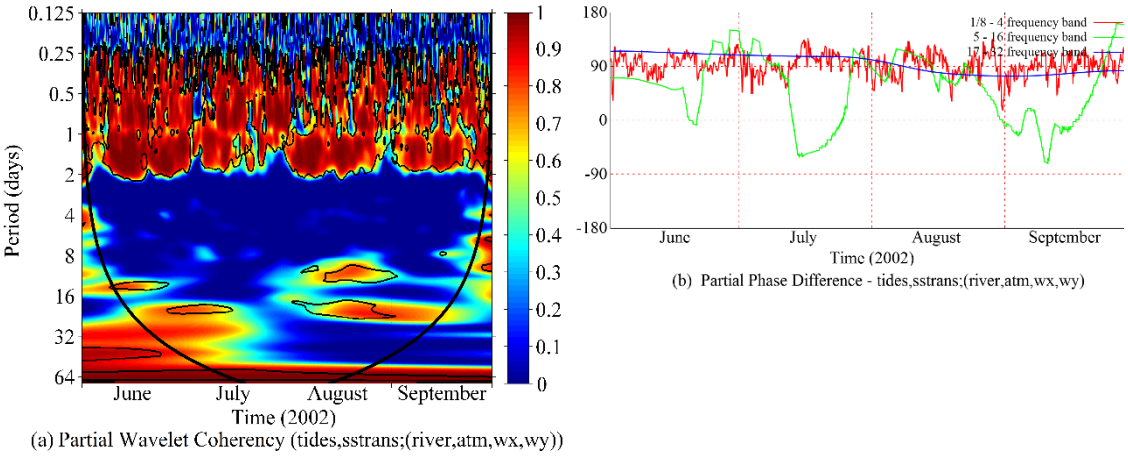

Figure 3.7 Observed tides versus salinity flux partial wavelet coherence and partial phase-differences. Thick black line indicates the cone of influence that delimits the region not influenced by edge effects.

Table 3-1 Mean phase difference and time lags between the forcing variables and the salinity flux

Forcing variable	Mean phase difference	Mean time lag
In-phase		
River discharge (river)	16.6	0.3
Tidal range (tides)	71.8	2.3
Atmospheric pressure (atm)	28.0	0.1
Wind vector (east-west) (wx)	52.4	2.0
Wind vector (north-south) (wy)	43.2	1.5
Out-of-phase		
River discharge (river)	95.5	1.4
Tidal range (tides)	-	-
Atmospheric pressure (atm)	90.4	0.3
Wind vector (east-west) (wx)	92.9	0.3
Wind vector (north-south) (wy)	100.7	0.3

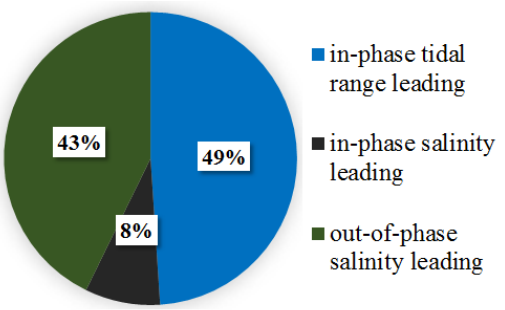

(a) Tide Level vs. Salinity Flux

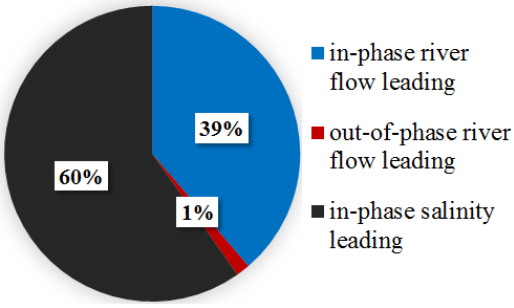

(b) River Discharge vs. Salinity Flux

Figure 3.8 Phase relationships – River discharge and tidal range versus salinity flux

3.3.2.2 Correlation between river discharge and salinity flux

PWC and PPD between river discharge and salinity flux, after controlling for other forcing variables, show statistically significant in-phase relationship in the 5-16-day period from early June to mid-July. This affirms the existence of the correlation between river discharge and salinity flux. Statistically significant high power coherence observed in June and July coincides with increased river discharge. The in-phase relationship means as the river discharge increases salinity being transported also increases. As shown in Figure 3.9**(b)**, the phase lags in the 1-4-day band are mainly in-phase between -90° and 90° and exhibiting very unstable lead-lag relationships between river discharge and salinity flux. The river discharge leads salinity flux and in phase in the 8-16-day period band, around the beginning of September. This can be the effect of increased river flows

due to typhoon events. The increased river flow rate enhances estuarine circulation (increased salinity flux along the bottom layer). For long-term period band (17-32), there is no statistically significant in-phase relationship, though beginning mid-August, river discharge was leading salinity transport. Figure 3.9**(a)** and Table 3-1 indicate that in about 39 % of the time river discharge is in-phase and leads salinity transport by about 0.3 days. Most of the time salinity flux is ahead of river discharge due to other transport mechanisms.

The discharge rate of Hii River, may flush salinity and as well as increasing in bottom salinity of Lake Nakaumi (Nakata et al. 2000). The time scale of this change may be residence time (beyond the scope of this study). A numerical study may be needed to understand the residence time in relation to the phase lag from wavelet analysis.

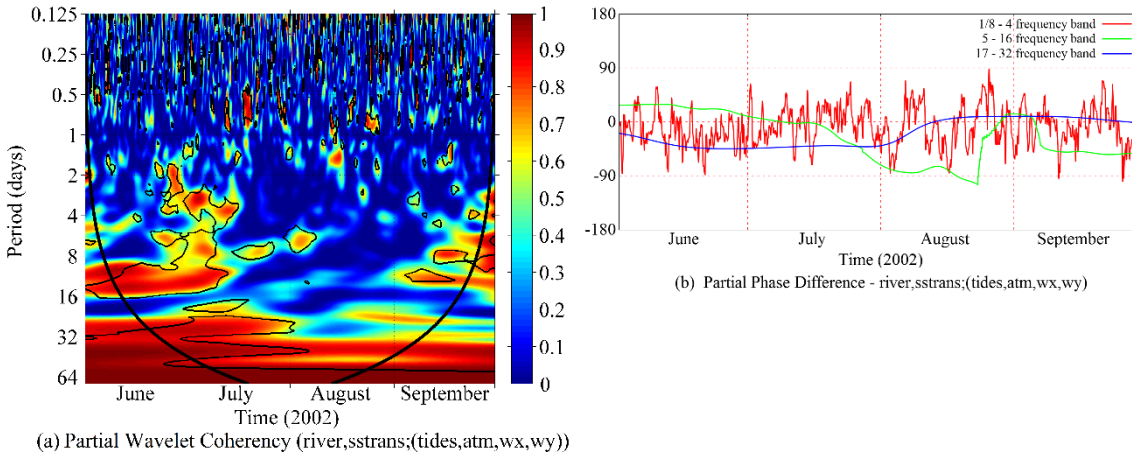

Figure 3.9 River discharge versus salinity flux partial wavelet coherence and partial phase-differences.

3.3.2.3 Correlation between atmospheric pressure and salinity flux

The statistically significant relationship between atmospheric pressure and salinity flux exists, though discontinuous and irregular, indicating the existence of correlation

between tide level and salinity flux. Figure 3.10**(b)** shows that the phase difference is typically between -90° and 90° and exhibiting very unstable lead-lag relationships between atmospheric pressure and salinity flux. Atmospheric pressure leads and in-phase with salinity flux in the 0.5 – 4-day period band. It's influence on the flux of salinity is not stable, implying it is short-lived and weak influence on salinity flux.

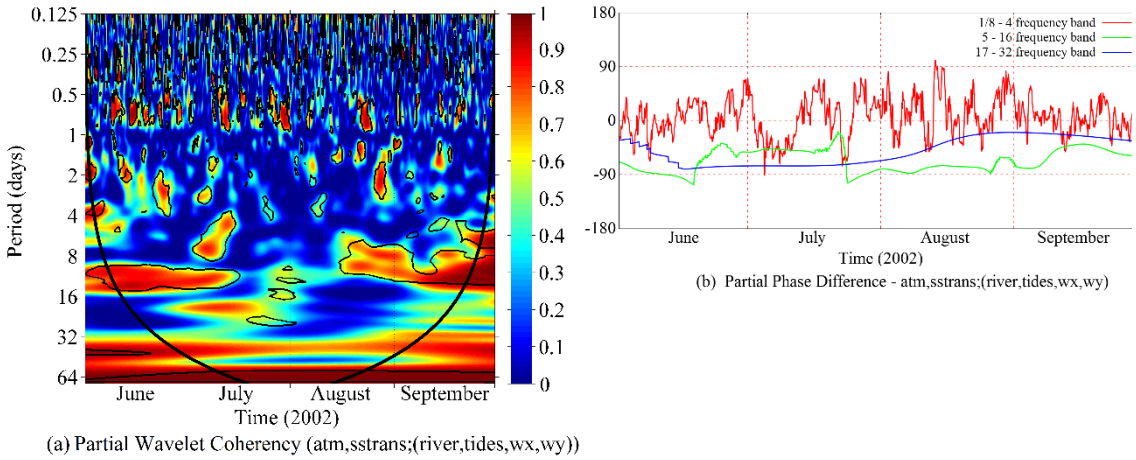

(a) Partial Wavelet Coherency (atm,sstrans;(river,tides,wx,wy))

(b) Partial Phase Difference - atm,sstrans;(river,tides,wx,wy)

Figure 3.10 Atmospheric pressure versus salinity flux partial wavelet coherence and partial phase-differences.

3.3.2.4 Correlation between wind vectors and salinity flux

Figure 3.11 shows that the phase lags in the 3-hour – 4-day band are mainly in-phase between -90° and 90° and exhibiting very unstable lead-lag relationships between wind vectors and salinity flux. However, in this period band salinity flux is mostly leading wind vectors. The west-east wind component and salinity flux are mainly in-phase with wind vector leading in the periods between 5 and 32-day. The statistically significant power sections in the 5 and 32-day period band for the south-north wind component are out-of-phase and lagging salinity flux. The statistically significant correlation between the west-east wind component (*wx*) and salinity flux exist mainly in the 8-16-day period

band, appearing consistently in August (Figure 3.11**(a)**). Short-term oscillations are irregular and short lived. For the south-north wind component (*wy*), they exist in the 2-4-day band mainly in July and August (Figure 3.11**(c)**). Wind vectors usually leads salinity flux by an average of 2 days and 1.5 days for east-west and north-south wind component, respectively (Table 3-1).

3.3.3 Implications of the study results

Astronomical tides being regular were the dominant parameter affecting sea surface elevation. It is also evident from Figure 3.3 and Figure 3.5 that sea surface elevation in Sakai Channel is affected by atmospheric pressure. The pressure drop in mid-June, mid-

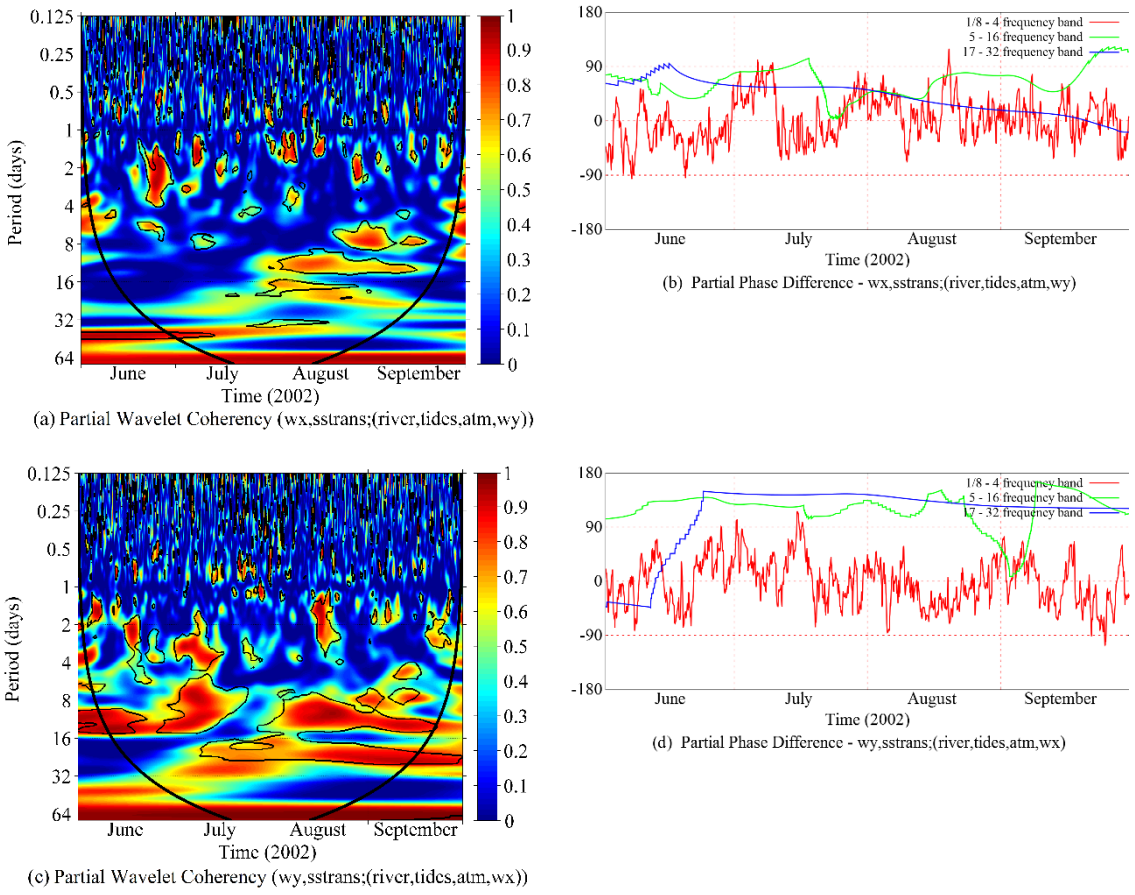

(a) Partial Wavelet Coherency (wx,sstrans;(river,tides,atm,wy))

(b) Partial Phase Difference - wx,sstrans;(river,tides,atm,wy)

(c) Partial Wavelet Coherency (wy,sstrans;(river,tides,atm,wx))

(d) Partial Phase Difference - wy,sstrans;(river,tides,atm,wx)

Figure 3.11 Wind vectors versus salinity flux partial wavelet coherence and partial phase-differences.

July and beginning of August resulted in an unusual increase in sea surface elevation. Salinity transport also responded to this change. River discharge occasionally affect salinity intrusion by diluting salinity and transporting it out of Lake Nakaumi. It also affects sea surface elevation in Sakai Channel and promoting salinity intrusion through the bottom layer. Wind drift has lesser effect but occasional froing winds promote circulation and either enhance or inhibits salinity intrusion.

River discharge is the only forcing parameter that may be controlled through damming upstream. Increased river discharge has the capacity to flush salinity of the lakes, however it also promotes salinity intrusion through the bottom according to previous studies (Nakata et al. 2000). Management of water flow in the Hii River system may be important in the mitigation of the impact of seawater intrusion to lakes ecosystems. To understand the effect of various river discharge scenarios on salinity transport, further studies using numerical models are required. Ministry of Land, Infrastructure, Transport and Tourism (MLIT) is promoting a flood management project, which constitutes construction of new reservoirs in the upper reaches of the Hii River and in the Kando River (Seigel 2012). The project will also construct a diverging channel connecting the Hii River and the Kando River, in conjunction with widening and deepening of Ohashi River. Since the study indicated that river discharge plays an important role in the saltwater intrusion process, the impact of these projects on salinity intrusion processes need to be studied. The widening of Ohashi River has impacts on the flow rate per cross-sectional area which may promote/inhibit seawater intrusion. Hence these projects should be included in models to come up with river system management practices for effective seawater intrusion management. The study attempted to analyse the mechanisms that

drove salinity transport through Nakaura Watergate before it was removed. New studies need to be carried out to understand the effect of the removal of the flood gates.

3.4 CONCLUSION

Salinity intrusion in the coupled coastal lakes (Shinji and Nakaumi) threatens the ecosystems in these lakes. This study elected to use the partial wavelet analysis as it provides an approach to analyse the impact of each forcing variable on the salinity flux in Sakai Channel after controlling the effect of all other forcing variables. The study results may provide a better understanding of the variation of river discharge, tide level, atmospheric pressure, wind vector and salinity flux, and also information that may guide release of water upstream for salinity flushing. The continuous wavelet transform results show that salinity flux mainly has 12-hour and 1-day periods. Hii River discharge does not show any periodical characteristics because of unpredictability of precipitation and controlled release from upstream reservoirs. Tide level shows periodical variation around 0.5 and 1-day period, indicating the dominants of the astronomical tides. Atmospheric pressure exhibits continuous high power with an average 6-day period affecting sea surface elevation occasionally. Wind data shows stable oscillations with periods between 8 and 32-day period. Partial wavelet coherence and partial phase difference revealed the influence of tide level and river discharge on salinity flux. Although the results suggest that atmospheric pressure and south-north wind vector have little influence on the salinity flux at Nakaura Watergate, it is possible for them to indirectly influence salinity transport through their effect on sea surface elevation. High pressure drops occasionally resulted in increased tide level. The geometry of Sakai channel may limit wind to cause changes only in the surface currents, hence weak effect on the overall transport of salinity. The study

quantified the phase lags between salinity flux and tide level; the peak of tide level was an average of 2.3 days ahead of salinity flux. Almost half the time, tide level was leading salinity flux. River discharge was about 0.3 days leading salinity flux. Almost 40% of the time, river discharge was leading salinity flux. This study found that salinity transport in the Sakai Channel increases with the increase of river discharge upstream. Further studies are needed to understand different river discharge regimes and their impacts on salinity intrusion, and the effect of the removal of Nakaura Watergate, taking into consideration the proposed MLIT flood management project.

4 MODELING STUDY OF WATER AND SALT EXCHANGE FOR A COUPLED COASTAL BRACKISH LAKE SYSTEM

4.1 INTRODUCTION

Since it is practically impossible to conduct long term water quality measurements across the entire lakes, this study will use simulation results to as measurements in the analysis of cross sectional salt flux. The hydrodynamic model in the STOC-LT (Ise Bay Simulator) was used (PARI n.d.). A three-dimensional hydrodynamic model was applied to study the dynamics of water and salt exchange through cross-sections in Lakes Shinji and Nakaumi close to Ohashi River. The model was validated with field data. Then the model results were used to study the characteristics of water and salt exchange. The goals of this this section are to examine the mechanisms that drive water and salt transport in Lakes Shinji and Nakaumi, and how they are influenced by different forcing conditions.

4.2 FLOW MODEL DESCRIPTION

4.2.1 Basic equations of flow model

4.2.1.1 Continuity equation

The following equation indicates the continuity equation used in this study. The fluid is assumed incompressible fluid.

$$\frac{\partial u_i}{\partial x_i} = 0 \tag{4-1}$$

Where, u_i is the flow (m/s) in the x_i direction.

4.2.1.2 Equation of motion

The following expression shows the equations of fluid motion. It should be noted that the equation of motion assumes *f*-plane approximation ($x_3 = z$ is positive in the upward vertical direction)

$$\frac{\partial u_i}{\partial t} = -\frac{\partial u_i u_j}{\partial x_j} - \varepsilon_{ijk} f_j u_k - \frac{1}{\rho}\frac{\partial P}{\partial x_i} + g_i + \frac{\partial}{\partial x_i}\left\{\nu_e\left(\frac{\partial u_i}{\partial x_j} + \frac{\partial u_j}{\partial x_i}\right)\right\} \tag{4-2}$$

Where, P is pressure (Pa), ρ is density $[\mathrm{kg\ m^{-3}}]$, $g = (0,0,-g)$ is the gravitational acceleration $[\mathrm{m\ s^{-2}}]$, $f = (0,0,f_0)$, f_0 is Coriolis parameter $[\mathrm{s^{-1}}]$, ν_e is the effective eddy viscosity coefficient $[\mathrm{m^2\ s^{-1}}]$.

Coriolis parameter is calculated by the following equation.

$$f_0 = 2\Omega \sin(\varphi_0) \tag{4-3}$$

Where, φ_0 is latitude, Ω is the rotational speed of the earth $[\mathrm{rad\ s^{-1}}]$, and is given by the following equation.

$$\Omega = \frac{2\pi}{t_{day}} \approx 7.29115858 \times 10^{-5}\ [\mathrm{rad\ s^{-1}}] \tag{4-4}$$

Where, t_{day} is the mean sidereal day (time for earth to make one rotation), 86164.0905 seconds (National Astronomical Observatory of Japan, 2000, p.87 (National Astronomical Observatory 2000)).

Next, consider the separation of the dynamic hydrostatic pressure of the pressure gradient term in the equation of motion. Vertical differential hydrostatic pressure p_h is given by the following equation.

$$\frac{\partial p_h}{\partial z} = -(\rho_0 + \rho')g \tag{4-5}$$

Where, ρ_0 is standard density [kg m^{-3}], ρ' is density deviation [kg m^{-3}], it is expressed by the following equation:

$$\rho'(x, y, z, t) = \rho(x, y, z, t) - \rho_0 \tag{4-6}$$

To determine the hydrostatic pressure at the position of height z, the equation (4-5) is integrated both sides from z to the water surface, η.

$$\begin{aligned} \int_z^\eta \frac{\partial p_h}{\partial z} dz &= -\int_z^\eta (\rho_0 + \rho')g \, dz \\ \therefore \quad p_h(z) &= p_a + \rho_0 g(\eta - z) + \int_z^\eta \rho' g \, dz \end{aligned} \tag{4-7}$$

Where, p_a is the atmospheric pressure [Pa].

Then, application of the Boussinesq approximation (when approximation to changes in fluid density is small enough ($\rho' \ll \rho_0$), the pressure varies independently of the other variables). The pressure *P* is approximated by separating the dynamic pressure p_d, and the hydrostatic pressure p_h, expanding gravity acceleration term and pressure gradient term as in the following equation.

$$
\begin{aligned}
-\frac{1}{\rho}\frac{\partial P}{\partial x_i} + g_i &= -\frac{1}{\rho_0+\rho'}\frac{\partial}{\partial x_i}(p_h + p_d) + g_i \\
&= -\left\{\frac{1}{\rho_0} - \frac{\rho'}{\rho_0^2} + \underbrace{\frac{\rho'\rho'}{\rho_0(\rho_0+\rho')}}_{\text{Disregard}}\right\}\frac{\partial}{\partial x_i}(p_h + p_d) + g_i \\
&= -\left(\frac{1}{\rho_0} - \frac{\rho'}{\rho_0^2}\right)\frac{\partial p_h}{\partial x_i} - \frac{1}{\rho_0}\frac{\partial p_d}{\partial x_i} + \underbrace{\frac{\rho'}{\rho_0^2}\frac{\partial p_d}{\partial x_i}}_{\text{Disregard}} + g_i \\
\therefore\ -\frac{1}{\rho}\frac{\partial P}{\partial x_i} + g_i &= -\left(\frac{1}{\rho_0} - \frac{\rho'}{\rho_0^2}\right)\frac{\partial p_h}{\partial x_i} - \frac{1}{\rho_0}\frac{\partial p_d}{\partial x_i} + g_i
\end{aligned}
\tag{4-8}
$$

By substituting the equation (4-7) into equation (4-8), the following formula in the x, y direction is obtained.

$$
\begin{aligned}
-\frac{1}{\rho}\frac{\partial P}{\partial x_i} &= -g\frac{\partial \eta}{\partial x_i} + \underbrace{\frac{\rho' g}{\rho_0}\frac{\partial \eta}{\partial x_i}}_{\text{Disregard}} - \frac{1}{\rho_0}\frac{\partial p'}{\partial x_i} + \underbrace{\frac{\rho'}{\rho_0^2}\frac{\partial p'}{\partial x_i}}_{\text{Disregard}} - \frac{1}{\rho_0}\frac{\partial p_d}{\partial x_i} \qquad (i = 1,2) \\
\therefore\ -\frac{1}{\rho}\frac{\partial P}{\partial x_i} &= -g\frac{\partial \eta}{\partial x_i} - \frac{1}{\rho_0}\frac{\partial p'}{\partial x_i} - \frac{1}{\rho_0}\frac{\partial p_d}{\partial x_i} \qquad (i = 1,2)
\end{aligned}
\tag{4-9}
$$

Here, p' is defined by the following equation.

$$
p' = p_a + \int_z^\eta \rho' g\, dz \tag{4-10}
$$

in the z −direction is,

$$
-\frac{1}{\rho}\frac{\partial P}{\partial z} - g = -\left(\frac{1}{\rho_0} - \frac{\rho'}{\rho_0^2}\right)(-\rho_0 g) - \frac{1}{\rho_0}\frac{\partial p_d}{\partial z} - g = -\frac{\rho'}{\rho_0}g - \frac{1}{\rho_0}\frac{\partial p_d}{\partial z} \tag{4-11}
$$

To sum up, equations of motion used in this study is derived. The dynamic pressure p_d is denoted by p again, the eddy viscosity ν_e is divided into the horizontal eddy viscosity ν_h, and vertical eddy viscosity ν_v.

$$\frac{\partial u}{\partial t} = -\frac{\partial uu}{\partial x} - \frac{\partial vu}{\partial y} - \frac{\partial wu}{\partial z} + f_0 v - \frac{1}{\rho_0}\frac{\partial p}{\partial x} - g\frac{\partial \eta}{\partial x} - \frac{1}{\rho_0}\frac{\partial p'}{\partial x} + \frac{\partial}{\partial x}\left(2\nu_h \frac{\partial u}{\partial x}\right) + \frac{\partial}{\partial y}\left\{\nu_h\left(\frac{\partial u}{\partial y} + \frac{\partial v}{\partial x}\right)\right\} + \frac{\partial}{\partial z}\left\{\nu_v\left(\frac{\partial u}{\partial z} + \frac{\partial w}{\partial x}\right)\right\} \quad (4\text{-}12)$$

$$\frac{\partial v}{\partial t} = -\frac{\partial uv}{\partial x} - \frac{\partial vv}{\partial y} - \frac{\partial wv}{\partial z} - f_0 u - \frac{1}{\rho_0}\frac{\partial p}{\partial y} - g\frac{\partial \eta}{\partial y} - \frac{1}{\rho_0}\frac{\partial p'}{\partial y} + \frac{\partial}{\partial x}\left\{\nu_h\left(\frac{\partial v}{\partial x} + \frac{\partial u}{\partial y}\right)\right\} + \frac{\partial}{\partial y}\left(2\nu_h \frac{\partial v}{\partial y}\right) + \frac{\partial}{\partial z}\left\{\nu_v\left(\frac{\partial v}{\partial z} + \frac{\partial w}{\partial y}\right)\right\} \quad (4\text{-}13)$$

$$\frac{\partial w}{\partial t} = -\frac{\partial uw}{\partial x} - \frac{\partial vw}{\partial y} - \frac{\partial ww}{\partial z} - \frac{1}{\rho_0}\frac{\partial p}{\partial z} - \frac{\rho'}{\rho_0}g + \frac{\partial}{\partial x}\left\{\nu_h\left(\frac{\partial w}{\partial x} + \frac{\partial u}{\partial z}\right)\right\} + \frac{\partial}{\partial y}\left\{\nu_h\left(\frac{\partial w}{\partial y} + \frac{\partial v}{\partial z}\right)\right\} + \frac{\partial}{\partial z}\left(2\nu_v \frac{\partial w}{\partial z}\right) \quad (4\text{-}14)$$

4.2.1.3 Transport equation of scalar quantities

The following equation show transport equation of scalar quantities (such as temperature and salinity)

$$\frac{\partial C}{\partial t} = -\frac{\partial uC}{\partial x} - \frac{\partial vC}{\partial y} - \frac{\partial wC}{\partial z} - \frac{\partial J_x^C}{\partial x} - \frac{\partial J_y^C}{\partial y} - \frac{\partial J_z^C}{\partial z} + q_C \quad (4\text{-}15)$$

where, C is water quality scalar quantity such as temperature and salinity [unit m^{-3}], J_x^C, J_y^C, J_z^C are flux of C in z x, y, z directions [unit $\mathrm{m}^{-2}\ \mathrm{s}^{-1}$], q_C are source terms of water quality scalar quantity C [unit $\mathrm{m}^{-3}\ \mathrm{s}^{-1}$].

In the water flux J_x^C, J_y^C, J_z^C from Fick's law of diffusion, is expressed by the following equation.

$$J_x^C = -D_h^C \frac{\partial C}{\partial x}, \quad J_y^C = -D_h^C \frac{\partial C}{\partial y}, \quad J_z^C = -D_v^C \frac{\partial C}{\partial z} \quad (4\text{-}16)$$

where, D_h^C is the effective horizontal eddy diffusion coefficient of water quality C [$m^2\ s^{-1}$], D_v^C is the effective vertical eddy diffusion coefficient [$m^2\ s^{-1}$].

4.2.1.4 Equation of the free surface

η[m] is the water surface level, and h[m] is the the bottom surface position. Assuming a one-valued function of the xy plane (not taking into account the breaking waves), continuous, kinematic conditional expression of the bottom and free surface, for both η and h, the equation of the free surface is expressed by the following equation.

$$\frac{\partial \eta}{\partial t} = -\frac{\partial}{\partial x}\left(\int_h^\eta u dz\right) - \frac{\partial}{\partial y}\left(\int_h^\eta v dz\right) \tag{4-17}$$

4.2.1.5 Equation of state

Knudsen equation of state express density as a function of water temperature and salinity (Nobuyuki Tamai 1980). Knudsen equation is represented by equations (4-18) to (4-22) as a function of the amount of chlorine Cl[‰].

$$\frac{\sigma_t}{10^3} = \Sigma_t + (\sigma_0 + 0.1324)\{1 - A_t + B_t(\sigma_0 - 0.1324)\} \tag{4-18}$$

$$\sigma_0 = -0.069 + 1.4708Cl - 1.570 \times 10^{-3}Cl^2 + 3.98 \times 10^{-5}Cl^3 \tag{4-19}$$

$$\Sigma_t = -\frac{(T - 3.98)^2}{503.570}\frac{T + 283}{T + 67.26} \tag{4-20}$$

$$A_t = T(4.7867 - 0.098185T + 0.0010843T^2) \times 10^{-3} \tag{4-21}$$

$$B_t = T(18.030 - 0.8164T + 0.01667T^2) \times 10^{-6} \tag{4-22}$$

Where T is the site water temperature [℃]

Relationship between chlorine content of $Cl[‰]$ and density $\rho[\mathrm{kg\,m^{-3}}]$, field density $\sigma_t[-]$, & salinity $S[-]$ is as follows:

$$\rho = \sigma_t + 1000 \tag{4-23}$$

$$S = 0.030 + 1.8050Cl \tag{4-24}$$

4.2.2 Boundary conditions

4.2.2.1 Boundary conditions of coastline

Conditions of the coastline using the following:

- Water level: zero gradient conditions.
- Flow rate: slip, no-slip selection at a fixed flow rate.
- Temperature and salinity: zero gradient.

4.2.2.2 Boundary conditions of the open ocean

It is possible to consider the following conditions for the boundary conditions of the open sea.

- Water level: select from four types of fixed water level, astronomical tide, the input value, and transparent boundary.
- Flow rate: zero velocity gradient.
- Temperature and salinity: zero gradient during outflow at the open sea boundary value flow, alternatively inflow and outflow zero gradient conditions.

4.2.2.3 Boundary condition of the water surface

Frictional stress $\boldsymbol{\tau}_{surface}$ of the surface of the water using the bulk formula:

$$\boldsymbol{\tau}_{surface} = \rho_a C_D \boldsymbol{W} \|\boldsymbol{W}\| \tag{4-25}$$

$$\|\boldsymbol{W}\| = \sqrt{W_x^2 + W_y^2} \tag{4-26}$$

where, $\boldsymbol{W}$ is the wind velocity vector (10m above the water surface) [m s^{-1}], W_x, W_y are the x, y components of the wind velocity vector, [m s^{-1}], ρ_a is the air density above the water surface [kg m^{-3}], C_D is the sea surface friction coefficient $[-]$.

Sea surface friction coefficient is also selected as a function of wind speed or input values using the model formula below (Honda & Mitsuyasu 1980).

$$C_D = A(1 + B\|\boldsymbol{W}\|) \tag{4-27}$$

$$\begin{cases} A = 1.28 \times 10^{-3}, B = -1.89 \times 10^{-2} & (\|\boldsymbol{W}\| < 8\text{m/s}) \\ A = 5.81 \times 10^{-4}, B = 1.078 \times 10^{-1} & (\|\boldsymbol{W}\| \geq 8\text{m/s}) \end{cases} \tag{4-28}$$

Heat transport in water is described in Section 4.2.3. Boundary conditions of salinity at the surface of the water, is set to zero gradient conditions.

4.2.2.4 Boundary condition on the bottom

Frictional stress of the bottom surface can be selected from the bulk formula or no-slip.

$$\boldsymbol{\tau}_{bottom} = \rho C_B \boldsymbol{u}_b \|\boldsymbol{u}_b\| \tag{4-29}$$

where, $\boldsymbol{u}_b$: friction velocity on the bottom surface [m s^{-1}], C_B: seafloor surface coefficient of friction $[-]$

It should be noted that the boundary conditions of temperature and salinity on the bottom surface are zero gradient conditions.

4.2.3 Heat balance model

4.2.3.1 The heat balance at the water surface

The heat balance elements in the water surface are shortwave radiation $Q_s[\mathrm{W\,m^{-2}}]$, long-wave radiation $Q_l[\mathrm{W\,m^{-2}}]$, latent heat $Q_e[\mathrm{W\,m^{-2}}]$, and the sensible heat flux $Q_c[\mathrm{W\,m^{-2}}]$. Of these, short wave radiation is absorbed by the very thin portion of the surface layer (about 10μm), and may be considered to be absorbed by the infinitesimal thickness (Kondō 1994). The shortwave radiation can penetrate into relatively deep water generating heat.

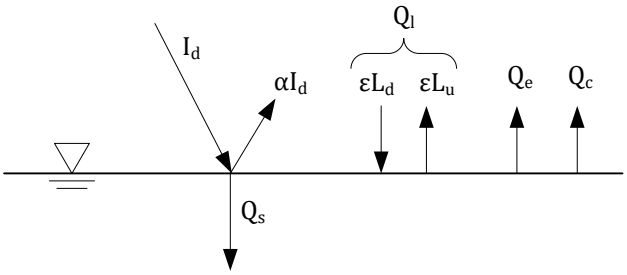

Figure 4.1 Heat balance at the water surface

With long-wave radiation and shortwave radiation assumed positive downwards (sky to water surface), sensible heat and latent heat assumed positive in the upwards (water surface to sky), the heat balance equation at the water surface is expressed by the following equation.

$$Q_n = Q_s + Q_l - Q_e - Q_c \tag{4-30}$$

where, Q_n is the net amount of heating in water $[\mathrm{W\,m^{-2}}]$. Therefore, the boundary conditions at the water surface is expressed by the following equation.

$$\left(\lambda \frac{\partial T}{\partial z}\right)_{z=\eta} = Q_n \tag{4-31}$$

where, T is the temperature [℃], λ is the thermal conductivity $[\mathrm{W\,m^{-1}\,K^{-1}}]$, c_p is specific heat $[\mathrm{J\,kg^{-1}\,K^{-1}}]$, K_T is temperature diffusion coefficient $[\mathrm{m^2\,s^{-1}}]$, $\lambda = \rho c_p K_T$

4.2.3.2 Shortwave radiation amount

Net shortwave radiation Q_s is a measure of the difference between incoming solar shortwave radiation $I_d[\mathrm{W\,m^{-2}}]$ and outgoing/reflected shortwave radiation from the water surface

$$Q_s = (1 - \alpha_s) I_d \tag{4-32}$$

where, α_s is the water surface albedo $[-]$. Practical variation of the α_s value in the low and middle latitudes is 0.06～0.08 (Kondō 1994). Solar radiation measurements from nearby weather stations are used. Alternatively, it is estimated from sunshine duration data of AMeDAS using the methods of (Shimazaki et al. 1996) and (Ninomiya et al. 1997).

The intensity of the light transmitted through water can be described by Lambert–Beer's law.

$$Q_s(z_b) = Q_s(z_t) \cdot \exp\{-k_{ext}(z_t - z_b)\} \tag{4-33}$$

where, $Q_s(z)$ is the amount of shortwave radiation at height z, k_{ext} is extinction coefficient $[\mathrm{m^{-1}}]$, z_t, z_b is height $[\mathrm{m}]$, positive upwards. Therefore, $Q_s(z_t) - Q_s(z_b)$ is the amount of shortwave radiation that is absorbed by water between $z_t \sim z_b$.

4.2.3.3 Long-wave radiation

Long-wave radiation is radiated from the water surface $L_u[\mathrm{W\,m^{-2}}]$, and also reflected by the clouds back to the water surface $L_d[\mathrm{W\,m^{-2}}]$. L_u long-wave radiation reverse amount, L_d is called the amount of atmospheric radiation. Net long-wave radiation at the water surface is obtained by multiplying the emissivity $\varepsilon(\approx 0.96)$ to the difference between the $L_u \; and \; L_d$.

$$Q_u = \varepsilon(L_u - L_d) \tag{4-34}$$

According to the Stefan-Boltzmann law, reverse long-wave radiation is expressed by the following equation.

$$L_u = \sigma(T_w + 273.15)^4 \tag{4-35}$$

where, σ is the Stefan-Boltzmann coefficient $5.67 \times 10^{-8}[\mathrm{W\,m^{-2}\ K^{-4}}]$, T_w is surface water temperature [℃].

If there are observation values of incoming longwave radiation, L_d they can be used, but in practice there are few observations. The method by (Ninomiya et al. 1996) can be used to estimate incoming longwave near the AMeDAS observation data. Another method by (Onuma et al. 2006) which use relative humidity and dew point temperature and is given by the following equation.

$$L_d = \varepsilon_{sky}\sigma(T_a + 273.15)^4 \tag{4-36}$$

$$\varepsilon_{sky} = a + bT_d + c \cdot RH \tag{4-37}$$

where, ε_{sky} is the injection rate of atmosphere $[-]$, T_a is temperature [℃], T_d is dew point temperature [℃], RH is relative humidity [%]. (Onuma et al. 2006) proposed model parameters, *a, b, c* in equation 1.3.8 as $a = 0.635,\ b = 0.00421,\ c = 0.00256$

4.2.3.4 Latent heat flux

Latent heat flux is the flux of heat from the water surface to the atmosphere that is associated with evaporation of water at the surface and subsequent condensation of water vapour in the troposphere. It can be expressed by the following bulk formula.

$$Q_e = LE = \rho_a L C_E (q_w - q_a)\|\boldsymbol{W}\| \tag{4-38}$$

where, L is latent heat associated with the unit amount of evaporation [J kg^{-1}], at 20℃ $L = 2.453 \times 10^6$[J kg^{-1}]. E is evaporation rate [kg m^{-2} s^{-1}]. ρ_a is air density [kg m^{-3}]. C_E is water vapor transport coefficients $[-]$ given in equation (4-41). q_w, q_a are water surface and air specific humidity [kg kg^{-1}] respectively.

Using vapour pressure e[hPa] and atmospheric p_a[hPa], specific humidity q is defined by the following equation.

$$q = \frac{0.622(e/p_a)}{1 - 0.378(e/p_a)} \tag{4-39}$$

Atmospheric pressure and water vapour pressure are recorded in meteorological observatories.

4.2.3.5 Sensible heat flux

Sensible heat flux is the process where heat energy is transferred from the water surface to the atmosphere by conduction and convection. It is expressed by the following bulk formula in the same way as latent heat flux.

$$Q_c = \rho_a c_{ap} C_C (T_w - T_a) \|\boldsymbol{W}\| \tag{4-40}$$

where, c_{ap} is specific heat capacity of air at a constant pressure to 1005 [J kg^{-1} K^{-1}], C_C is sensible heat transport coefficients $[-]$, T_a is sea temperature [℃].

C_E, C_C are bulk transport coefficients calculated by the following equation as a function of wind speed (Kondō 1994).

$$C_E = C_C = \begin{cases} 1.15 \times 10^{-3}, & (1\mathrm{m/s} \leq \|\boldsymbol{W}\| < 5m/s) \\ 1.25 \times 10^{-3}, & (5\mathrm{m/s} \leq \|\boldsymbol{W}\|) \end{cases} \tag{4-41}$$

4.2.4 Turbulence model

In the coastal zone spatial variation in water temperature, salinity, etc., are generally change more in the vertical direction than in the horizontal direction. For example, changes in vertical profile of salinity in 10 ~ 20 m is not uncommon. In view of the water features such as coastal areas, it was decided to use model with different horizontal and vertical turbulence models.

4.2.4.1 Horizontal turbulent model

Horizontal turbulence model used was Smagorinsky model, which is a kind of SGS (Sub-Grid Scale) turbulence model, (Smagorinsky 1963). SGS turbulence model is a model used in the LES (Large Eddy Simulation). Since small eddies have been found to be universally constant regardless of the type of flow, LES models only the small eddies which are expected to be universally constant, large eddies are solved directly, rather than relying on model calculations (Kajishima 1999). Turbulent stress acting in the mesh size = *Grid Scale* (*GS*) or less is called *SGS* stress. To model the *SGS* stress, (Smagorinsky 1963) in the following equation proposed an eddy viscosity approximation model.

$$\nu_e = (C_s\Delta)^2\left(2S_{ij}S_{ij}\right)^{1/2} \tag{4-42}$$

where, C_s is the Smagorinsky constant $[-]$, Δ is the filter width [m], S_{ij} is called velocity strain tensor, rate of strain tensor, or the rate of deformation tensor defined by the following equation.

$$S_{ij} = \frac{1}{2}\left(\frac{\partial u_i}{\partial x_j} + \frac{\partial u_j}{\partial x_i}\right) \tag{4-43}$$

Smagorinsky constant, has the theoretical value, $C_s = 0.173$ in homogeneous isotropic turbulence, but the value is different depending on the turbulence form, therefore it is not a universal constant (Kajishima 1999).

On the other hand, (Nakatsuji et al. 1992) has suggested that horizontal turbulence models use a mesh size of several hundred m ~ several km order, and then interpret the Smagorinsky model as zero equation model using a typical length eddy viscosity coefficient and strain rate.

$$\nu_h = (C_s\Delta)^2\left(2S_{ij}S_{ij}\right)^{1/2} \quad (i,j = 1,2) \tag{4-44}$$

In this case, considering only the two-dimensional horizontal, filter width and the strain rate tensor are expressed by the following equations.

$$S_{ij}S_{ij} = \left(\frac{\partial u}{\partial x}\right)^2 + \frac{1}{2}\left(\frac{\partial u}{\partial y} + \frac{\partial v}{\partial x}\right)^2 + \left(\frac{\partial v}{\partial y}\right)^2 \tag{4-45}$$

$$\Delta = \sqrt{\Delta x \cdot \Delta y} \tag{4-46}$$

Model constant, $C_s = 0.12$ was proposed from the measurements at Uraga channel.

Copying (Nakatsuji et al. 1992) in this model, it was decided to use the Smagorinsky model equations (4-44) ~ (4-46). Note, the eddy diffusion coefficient D_h, and eddy thermal diffusion coefficient K_h, can be expressed by the following equations using the horizontal turbulent Prandtl number Pr_h and horizontal turbulence Schmidt number Sc_h.

$$D_h = \frac{\nu_{eh}}{Sc_h} \tag{4-47}$$

$$K_h = \frac{\nu_{eh}}{Pr_h} \tag{4-48}$$

4.2.4.2 Vertical turbulence model

Modeling incorporating the damping effect of turbulence for vertical turbulent flow model is required when the density stratification is developed. In Ise Bay Simulator, zero equation model of Munk-Anderson type turbulence model is used (Munk & Anderson 1948).

$$\nu_v = \nu_{V0}(1 + \beta_v Ri)^{\alpha_v} \tag{4-49}$$

$$D_v = \frac{\nu_{V0}}{Sc_v}(1 + \beta_d Ri)^{\alpha_d} \tag{4-50}$$

$$K_v = \frac{\nu_{V0}}{Pr_v}(1 + \beta_t Ri)^{\alpha_t} \tag{4-51}$$

where, ν_{V0} is vertical eddy viscosity in a neutral state density [$m^2\ s^{-1}$]. $Sc_v,\ Pr_v$ are the Schmidt number and Prandtl number in vertical direction, respectively. $\alpha_v, \beta_v, \alpha_d, \beta_d, \alpha_t, \beta_t$ are model constants. Ri is the gradient Richardson number, and is defined by the following equation.

$$Ri = \frac{-g\frac{\partial \rho}{\partial z}}{\rho\left\{\left(\frac{\partial u}{\partial z}\right)^2 + \left(\frac{\partial v}{\partial z}\right)^2\right\}} \tag{4-52}$$

(Nakatsuji et al. 1991) promoted the value of less than or equal to the combination of the (Munk & Anderson 1948) and (Webb 1970) models constants.

$$\alpha_v = -1, \quad \beta_v = 5.2, \quad \alpha_d = -3/2, \quad \beta_d = 10/3 \tag{4-53}$$

This model use the model constants values in the equation above (4-53).

4.2.5 Time Development Methods

4.2.5.1 Continuity equation and pressure coupling method

The model uses the staggered grid system in the computational domain, and put variables as shown in Figure 4.2

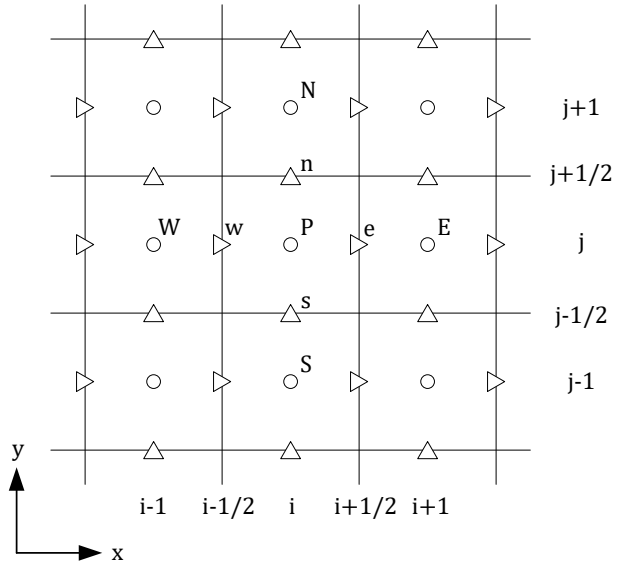

Figure 4.2 Variable positions on the xy coordinate plane (○ defines the position of the water level and pressure, △ defines the position of flow rate)

The pressure calculations are done based on SMAC method (Amsden & Harlow 1970). Equations of motion (4-12) – (4-14), when handled in the implicit method, the diffusion term in the vertical direction and the water level gradient term, are expressed by the following equations.

$$\frac{u^p - u^n}{\Delta t} = -\frac{1}{\rho_0}\frac{\delta p^n}{\delta x} - g\frac{\delta \eta^p}{\delta x} + \frac{\delta}{\delta z}\left(\nu_e \frac{\delta u^p}{\delta z}\right) + F_u(\boldsymbol{u}^n) \tag{4-54}$$

$$\frac{v^p - v^n}{\Delta t} = -\frac{1}{\rho_0}\frac{\delta p^n}{\delta y} - g\frac{\delta \eta^p}{\delta y} + \frac{\delta}{\delta z}\left(\nu_e \frac{\delta v^p}{\delta z}\right) + F_v(\boldsymbol{u}^n) \tag{4-55}$$

$$\frac{w^p - w^n}{\Delta t} = -\frac{1}{\rho_0}\frac{\partial p^n}{\partial z} + \frac{\delta}{\delta z}\left(2\nu_e \frac{\delta w^p}{\delta z}\right) + F_w(\boldsymbol{u}^n) \tag{4-56}$$

where, subscript n is the value of n^{th} step, p refers to the predicted value of $n + 1^{th}$ step. δ represents the differential symbol. F_u, F_v, F_w is a term such as a collection of diffusion term or advection term.

Solution of equations (4-54) – (4-56) are described below, starting with the coupling method of pressure and flow rate. Dynamic pressure is solved implicitly, hence the predicted value of the flow velocity is modified by the following equation.

$$u_i^{n+1} = u_i^p - \frac{\Delta t}{\rho_0}\frac{\delta \phi}{\delta x_i} \quad (i = 1,2,3) \tag{4-57}$$

Here, φ corresponds to the correction amount of the dynamic pressure p^n, p^{n+1} is calculated by the following equation.

$$p^{n+1} = p^n + \phi \tag{4-58}$$

Substituting the above equation (4-58) into the continuity equation, assuming zero divergence u_i^{n+1}, Poisson pressure equation is derived.

$$\frac{\delta^2 \phi}{\delta x^2} + \frac{\delta^2 \phi}{\delta y^2} + \frac{\delta^2 \phi}{\delta z^2} = \frac{\rho_0}{\Delta t}\left(\frac{\delta u^p}{\delta x} + \frac{\delta v^p}{\delta y} + \frac{\delta w^p}{\delta z}\right) \tag{4-59}$$

4.2.5.2 Water level and flow rate coupling method

Discretizing the free surface equation (4-17) and expressed as the following equation.

$$\frac{\eta_P^p - \eta_P^n}{\Delta t} = -\frac{1}{\Delta x_P}\left(\sum_{k=1}^{K} u_{e,k}^p \Delta z_k\right) + \frac{1}{\Delta x_P}\left(\sum_{k=1}^{K} u_{w,k}^p \Delta z_k\right) - \frac{1}{\Delta y_P}\left(\sum_{k=1}^{K} v_{n,k}^p \Delta z_k\right) + \frac{1}{\Delta y_P}\left(\sum_{k=1}^{K} v_{s,k}^p \Delta z_k\right) \tag{4-60}$$

Here, subscript k represents the mesh number in the z-direction.

A discretization of the equations of motion in the x–direction at position $(i + 0.5, j, k)$ (point e in Figure 4.2).

$$\frac{u_{e,k}^p - u_{e,k}^n}{\Delta t} = -\frac{1}{\rho_0}\frac{p_{E,k}^n - p_{P,k}^n}{\Delta x_e} - g\frac{\eta_E^p - \eta_P^p}{\Delta x_e} + \frac{1}{\Delta z_k}\left(\nu_{v,k+0.5}\frac{u_{e,k+1}^p - u_{e,k}^p}{\Delta z_{k+0.5}} - \nu_{v,k-0.5}\frac{u_{e,k}^p - u_{e,k-1}^p}{\Delta z_{k-0.5}}\right) + F_u(\boldsymbol{u}^n) \quad (k = 1, \cdots, K) \tag{4-61}$$

In summary, it can be expressed by the following equation.

$$A_{e,k}^u u_{e,k}^p + A_{eT,k}^u u_{e,k+1}^p + A_{eB,k}^u u_{e,k-1}^p = B_{eE,k}^u \eta_E^p + B_{eP,k}^u \eta_P^p + Q_{e,k}^u \tag{4-62}$$

$$A_{e,k}^u = \frac{1}{\Delta t} + \frac{\nu_{v,k+0.5}}{\Delta z_k \Delta z_{k+0.5}} + \frac{\nu_{v,k-0.5}}{\Delta z_k \Delta z_{k-0.5}}, \quad A_{eT,k}^u = -\frac{\nu_{v,k+0.5}}{\Delta z_k \Delta z_{k+0.5}}, \quad A_{eB,k}^u = -\frac{\nu_{v,k-0.5}}{\Delta z_k \Delta z_{k-0.5}},$$

$$B_{eE,k}^u = -\frac{g}{\Delta x_e}, \quad B_{eP,k}^u = \frac{g}{\Delta x_e}, \quad Q_{e,k}^u = \frac{u_e^n}{\Delta t} - \frac{1}{\rho_0}\frac{p_{E,k}^n - p_{P,k}^n}{\Delta x_e} + F_u(\boldsymbol{u}^n) \tag{4-63}$$

Equation (4-62) can be expressed in matrix form given by the following equation.

$$\begin{pmatrix} A^u_{e,1} & A^u_{eT,1} & 0 & 0 & 0 \\ A^u_{eB,2} & A^u_{e,2} & A^u_{eT,2} & 0 & 0 \\ 0 & A^u_{eB,3} & A^u_{e,3} & A^u_{eT,3} & 0 \\ \vdots & \vdots & \vdots & \vdots & \vdots \\ 0 & 0 & 0 & A^u_{eB,K} & A^u_{e,K} \end{pmatrix} \begin{pmatrix} u^p_{e,1} \\ u^p_{e,2} \\ u^p_{e,3} \\ \vdots \\ u^p_{e,K} \end{pmatrix} = \begin{pmatrix} B^u_{eE,1} & B^u_{eP,1} \\ B^u_{eE,2} & B^u_{eP,2} \\ B^u_{eE,3} & B^u_{eP,3} \\ \vdots & \vdots \\ B^u_{eE,K} & B^u_{eP,K} \end{pmatrix} \begin{pmatrix} \eta^p_E \\ \eta^p_P \end{pmatrix} + \begin{pmatrix} Q^u_{e,1} \\ Q^u_{e,2} \\ Q^u_{e,3} \\ \vdots \\ Q^u_{e,K} \end{pmatrix} \tag{4-64}$$

Since the left side of equation (4-64) has a tri-diagonal matrix, it is possible to solve sequentially by TDMA (Tri-Diagonal Matrix Algorithm) (Sato et al. 1993). As a result of applying the TDMA, equation (4-64) is organized as follows.

$$u^p_{e,k} = b^u_{eE,k}\eta^p_E + b^u_{eP,k}\eta^p_P + q_{e,k} \quad (k = 1, \cdots, K) \tag{4-65}$$

In the same way, discretization of the equations of motion in the *x*–direction (point *w* in Figure 4.2) at position $(i - 0.5, j, k)$ yields the following equation.

$$u^p_{w,k} = b^u_{wP,k}\eta^p_P + b^u_{wW,k}\eta^p_W + q_{w,k} \quad (k = 1, \cdots, K) \tag{4-66}$$

Similarly, discretization for equations of motion in the *y*–direction.

$$v^p_{n,k} = b^v_{nN,k}\eta^p_N + b^v_{nP,k}\eta^p_P + q^v_{n,k} \tag{4-67}$$

$$v^p_{s,k} = b^v_{sP,k}\eta^p_P + b^v_{sS,k}\eta^p_S + q^v_{s,k} \tag{4-68}$$

Substituting equations (4-65) – (4-68) into equation (4-60), yields the following equation.

$$C_P\eta^p_P + C_E\eta^p_E + C_W\eta^p_W + C_N\eta^p_N + C_S\eta^p_S = D_P \tag{4-69}$$

Equation (4-69) is a two-dimensional Poisson equation for the water, it can be determined by iterative computation. Water level η^p is determined, estimated value of the flow velocity, $\boldsymbol{u}^p$ can be calculated from equations (4-65) – (4-68). In addition, the water level, η^{n+1} at the $n+1^{th}$ step is the same as η^p; ($\eta^{n+1} = \eta^p$).

4.2.5.3 Scalar quantity transport equation

After obtaining the scalar quantity flow field, then solve the transport equation. At this time, implicit Euler method stabilize the vertical diffusion term, otherwise use explicit Euler method. That is, the following partial phase method (fractional step method) was done.

$$\frac{C^* - C^n}{\Delta t} = F_C(C^n) \tag{4-70}$$

$$\frac{C^{n+1} - C^*}{\Delta t} = \frac{\delta}{\delta z}\left(D_v^C \frac{\delta C^{n+1}}{\delta z}\right) \tag{4-71}$$

Where, F_C is the diffusion term other than the non-steady-state term and vertical term, C^* is a temporary variable for determining C^{n+1}. Since only the vertical direction is implicit, it is a semi-implicit method, hence it can be solved faster using TDMA.

4.2.5.4 Numerical computational procedure flowchart

The flowchart shows a rough flow of numerical calculation procedure (Figure 4.3).

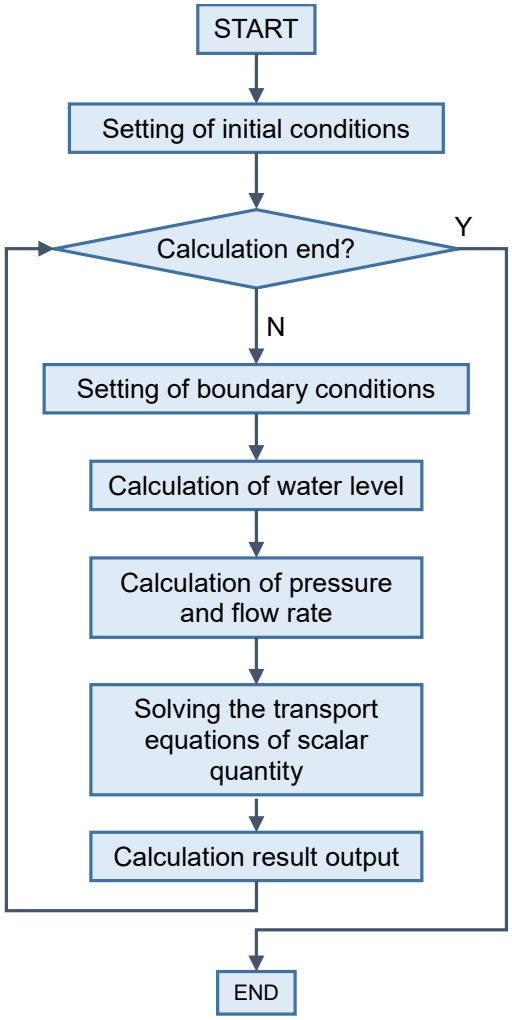

Figure 4.3 Flow chart of the calculation procedure

4.2.6 Finite difference and numerical method

4.2.6.1 Finite difference method

The second-order central (finite) difference of except in the advection term, the advection term is by Total Variation Diminishing (TVD) scheme with MUSCL method. Below, the TVD scheme is shown.

The scalar quantity φ, and the flow velocity u, preserving advection equation in one-dimensional is represented by the following equation.

$$\frac{\partial \phi}{\partial t} + \frac{\partial u\phi}{\partial x} = 0 \tag{4-72}$$

Discretizing using explicit Euler method the above equation is expressed as follows (omitted character above subscript *n*).

$$\phi_P^{n+1} = \phi_p - \frac{\Delta t}{\Delta x_P}\{(u\phi)_e - (u\phi)_w\} \tag{4-73}$$

In the case of staggered grid, the calculation method $(u\phi)_e, (u\phi)_w$ is a problem.

TVD scheme of MUSCL method for 1 parameter is summarized below (Kobayashi 2003).

$$(u\phi)_w = \max(u_w, 0) \cdot \phi_w^+ + \min(u_w, 0) \cdot \phi_w^- \tag{4-74}$$

$$\phi_w^+ = \phi_W + \frac{1+\kappa}{4}\mathrm{minmod}(\delta\phi_w, b\delta\phi_{Ww}) + \frac{1-\kappa}{4}\mathrm{minmod}(\delta\phi_{Ww}, b\delta\phi_w) \tag{4-75}$$

$$\phi_w^- = \phi_P - \frac{1+\kappa}{4}\mathrm{minmod}(\delta\phi_w, b\delta\phi_e) + \frac{1-\kappa}{4}\mathrm{minmod}(\delta\phi_e, b\delta\phi_w) \tag{4-76}$$

$$\delta\phi_w = \phi_P - \phi_W \tag{4-77}$$

$$\mathrm{minmod}(x, y) = \frac{\mathrm{sign}(x) + \mathrm{sign}(y)}{2} \cdot \min(|x|, |y|) \tag{4-78}$$

$$\mathrm{sign}(x) = \begin{cases} +1 & (x \geq 0) \\ -1 & (x < 0) \end{cases} \tag{4-79}$$

$$b = \frac{3-\kappa}{1-\kappa} \tag{4-80}$$

where, κ is a parameter that determines the accuracy $|\kappa| \leq 1$. It is possible to select the accuracy of κ value as follows.

$$\kappa = \begin{cases} 1 & 2nd\ order\ central\ difference \\ 1/3 & 3rd\ order\ upstream\ difference \\ 1/2 & QUICK\ Scheme \\ -1 & 2nd\ order\ upwind\ scheme \end{cases} \tag{4-81}$$

4.2.6.2 Free-surface treatment

When water level fluctuation is calculated with only the surface layer mesh, top layer becomes too thick and calculation accuracy falls. Therefore, it should be able to accommodate the fluctuating water levels across the mesh (Figure 4.4).

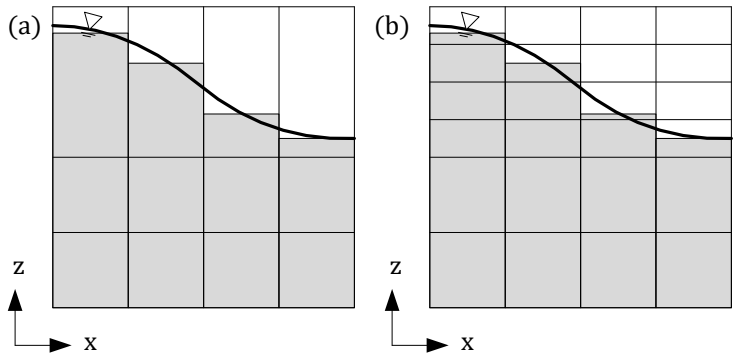

Figure 4.4 Mesh cases; (a) water level fluctuations occur only in the surface mesh, (b) if the water surface position crosses the mesh

4.2.7 Modeling domain, grid system, and model setup

The model domain is Lakes Shinji and Nakaumi with Sakai Channel as the open boundary and Hii River as the freshwater input boundary (Figure 4.6). The modelling domain is 42 km× 14 km in the east–west and north–south directions, respectively. The grid system has 3,675 surface water cells with the grid size of 400 m and 57 vertical z-coordinate layers, with the grid size of varying from 20 cm to 1 m.

The time step varies from 1 s to 60 s with a safety factor of 0.6. The model was set to calculate the flow field, temperature, salinity and full 3D non-hydrostatic. Although the model has ecosystem model, it was not switched in this simulation. The open boundary conditions were read from open boundary files. The horizontal turbulence model was set to Sub-Grid Scale (SGS) and the vertical Mellor-Yamada. Other vertical turbulence models are available for selection.

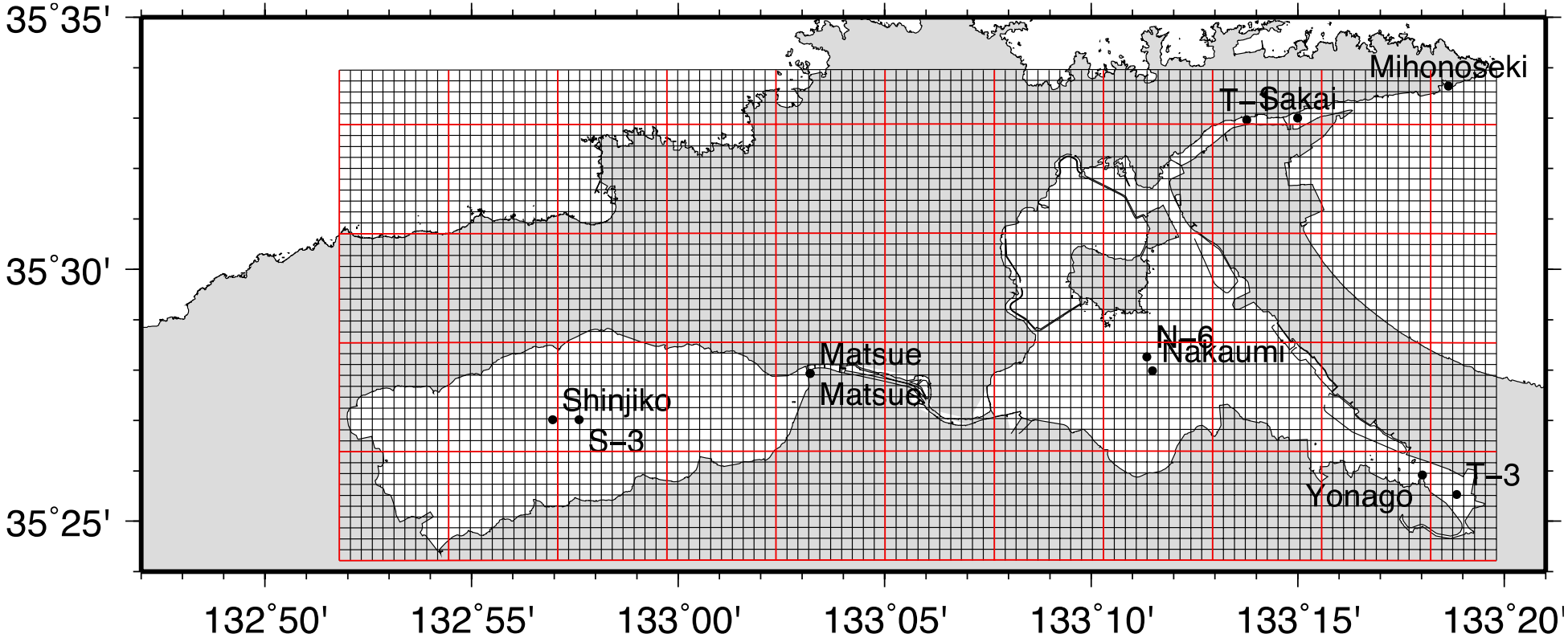

Figure 4.5 Simulation domain mesh diagram

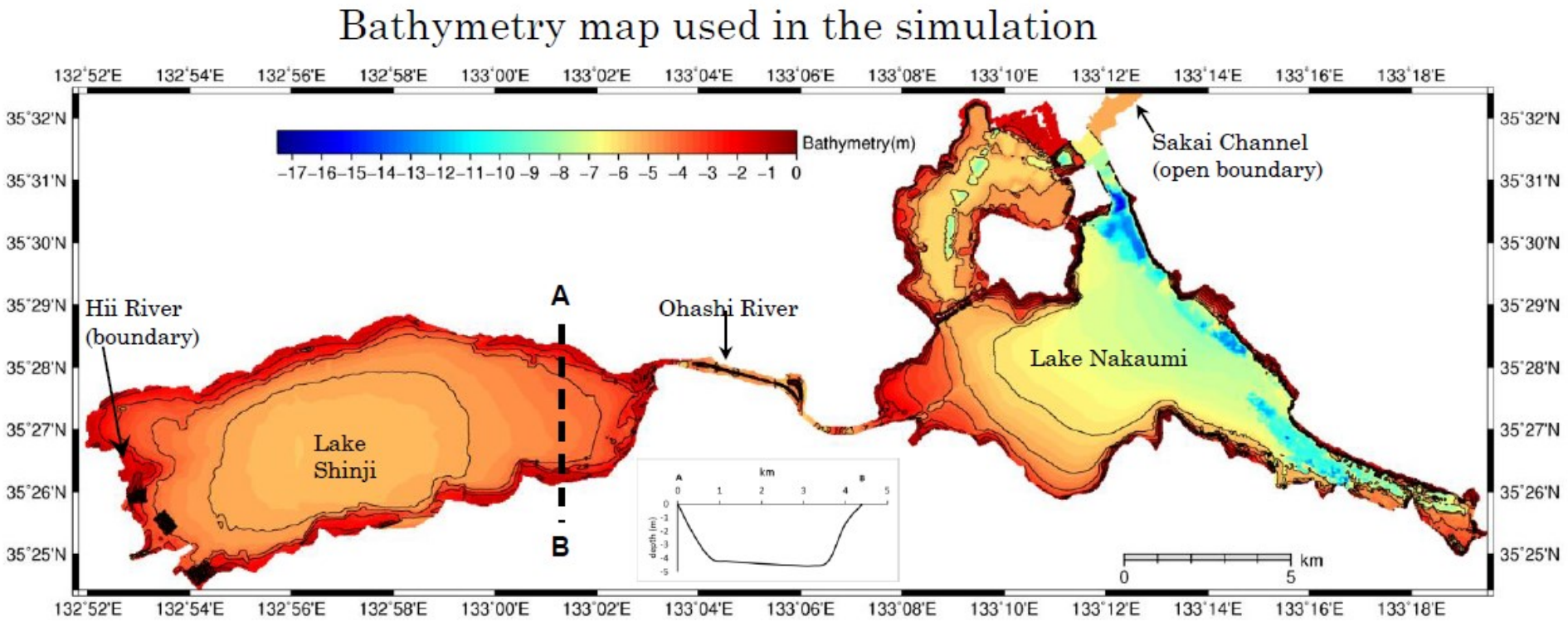

Figure 4.6 The bathymetry of the simulation domain

Figure 4.7 Location of stations used in the data – model comparison

4.2.8 Simulation initial and boundary conditions

The application of the model requires the specification of input parameters for initial conditions, input river and surface boundary conditions, and open boundary conditions. Input parameters for initial conditions are surface elevation, velocity, water temperature and salinity. Input parameters for input river boundary conditions are river discharge, and water temperature. Solar radiation, atmospheric pressure, air temperature, wind, water vapour pressure and precipitation are the input parameters for the surface boundary conditions. Those for the open boundary conditions are surface elevation, water temperature, velocity and salinity.

With cold start, i.e., setting initial condition of zero for velocity, the model becomes stabilized within a month. The initial conditions for salinity, water temperature and surface elevation are set arbitrarily based on the observed data. The model was allowed a month of initial warming up from the cold start. Hourly freshwater discharge data from Kamishima gauging station, in Hii River, are obtained from the MILT and PARI. Hourly wind data at Matsue Meteorological Station and Lake Shinji mid-lake station are obtained from JMA and PARI, respectively and are used for the surface boundary conditions. The data at Sakai Tide Station was used for the open boundary condition for water level. The data at Nakaura Watergate are used for all open boundary cells in the Sakai Channel. The model results agreed well with the observed surface elevation throughout the modelling domain, no correction was made for the water level open boundary condition. The observed salinity data at Nakaura Watergate are used as open boundary condition.

Vertical salinity profiles for four layers are constructed using observed values assuming homogeneity within the respective layers.

Table 4-1 Data for model validation

	Station	Time period	Depth	Source
Surface elevation	10 water level stations	2002-2003	–	
Current velocity	Nakaura Watergate	2003	Surface	SPIPHES
		2003	Middle	
		2003	Bottom	
	Ohashi River Downstream	2003	Surface	PARI
		2003	Middle	
		2003	Bottom	
	Ohashi River Upstream	2003	Surface	PARI
		2003	Middle	
		2003	Bottom	
Salinity	Nakaumi mid-lake station (N6)	2003	Surface	MILT
		2003	Middle	
		2003	Bottom	
	Matsue	2003	Surface	PARI
		2003	Middle	
		2003	Bottom	
	Lake Shinji mid-lake station (S3)	2003	Surface	PARI
		2003	Middle	
		2003	Bottom	
Water temperature	Nakaumi mid-lake station (N6)	2003	Surface	MILT
		2003	Middle	
		2003	Bottom	
	Matsue	2003	Surface	PARI
		2003	Middle	
		2003	Bottom	
	Lake Shinji mid-lake station (S3)	2003	Surface	PARI
		2003	Middle	
		2003	Bottom	

4.3 MODEL-DATA COMPARISON

The validation of the model was done using the data summarised in Table 4-1, with location of the stations shown in Figure 4.7. A simulation run was conducted for 1.5 years (January 1, 2003 and March 31, 2004), and the simulation results were compared with hourly surface elevation data at fourteen water level monitoring stations. The model

results were also compared with hourly water temperature and salinity data at Lake Nakaumi mid-lake station, Matsue station and Lake Shinji mid-lake station. Current velocity data at Nakaura Watergate station, Ohashi River upstream and downstream station was compared with model results. The simulation results were compared with the observed data for both total and subtidal (33-hour low-pass filtered) components.

The mean error (ME), mean absolute error (MAE), and predictive skill (Skill) are used as quantitative assessments for the comparison simulation results – observed data, and given in Table 4-3. They are defined as (Kim & Park 2012):

$$ME = \frac{\sum(M_n - O_n)}{N} \tag{4-82}$$

$$MAE = \frac{\sum|M_n - O_n|}{N} \tag{4-83}$$

$$Skill = 1 - \frac{\sum(M_n - O_n)^2}{\sum(|M_n - \bar{O}| + |O_n - \bar{O}|)^2} \tag{4-84}$$

where M_n and O_n are the n^{th} simulation result and observation, respectively, $\bar{O}$ is the time mean data, and N is the number of observations. On average positive *ME* (negative *ME*) indicates over-prediction (under prediction). The average deviation between simulation results and observed data is indicated by the magnitude of *MAE*. *Skill* indicates the ability for the model to reproduce observed data; a skill of one (zero) indicates perfect agreement (complete disagreement).

4.3.1 Surface elevation

The model application reproduced the observed surface elevation well, with an average ME of -6.89 cm, MAE of 7.68 cm, and model skill of 93% (Table 4-2). The simulation results have good agreement with both the total, tidal and subtidal components at the ten stations throughout the computational domain. The model managed to reproduce the tidal variations well (Figure 4.8). The model also successfully reproduced surface elevation response to river discharge, atmospheric pressure and wind (Figure 4.9). Both observed data and simulation results show that increased river discharge affects surface elevation in Lake Shinji and Ohashi River, resulting in an increase in water level slope between Lake Shinji and Lake Nakaumi, particularly in June, July and September. The influence of the river discharge is mostly confined to Lake Shinji and Ohashi River resulting in the flushing out of freshwater through Ohashi River.

Table 4-2 Error estimates for simulation - observation surface elevation results comparison

Variables	**Station**	**Total component**			
		ME	MAE	Skill	N
Surface elevation (cm)	Higashi	-6.64	8.06	90%	19704
	Kimachi	-9.52	10.29	86%	19704
	Shinji S3	-6.77	7.90	91%	19704
	Sada	-3.64	6.70	93%	19704
	Matsue	-7.97	8.63	89%	19704
	Yata S5	-7.64	7.68	94%	19704
	Yahata	-7.44	7.51	95%	19704
	Nakaumi N6	-5.50	5.50	97%	19704
	Ejima	-10.29	10.29	92%	19704
	Yonago	-3.46	4.21	98%	19704

Atmospheric pressure and wind has been considered important for modifying water level slope and thus the subtidal response of Ohashi River, Lake Shinji and Lake Nakaumi

(Nakata et al. 2000). The prevailing east–west wind directly alters water level slope in Lake Shinji and along Ohashi River, consequently producing barotropic circulation within Lake Shinji at periods of 2-8 days. Both observed data and simulations results show that relatively strong westerly wind causes surface rise e.g. in 2003 on June 13, 20, 25 and 28; and September 13, and relatively strong easterly wind causes surface fall on e.g. June 8, August 16 and September 21 (Figure 4.9). The water surface rise and fall occurs at all the ten stations, and the surface fluctuation spreads in the direction of wind. Atmospheric pressure directly alters the water surface elevation. Both observed data and simulations results show the response of water surface elevation to atmospheric pressure fluctuation. Relatively strong atmospheric pressure causes water surface rise e.g. in 2003 on June 12, 19, 24, 28; July 29; August 9, 28 and September 13. The drop in atmospheric pressure generally coincides or slightly leads increased westerly winds. The degree of water surface rise increases towards Lake Nakaumi, probably due to pressure drop which coincides with increased westerly wind. The model reproduced well the variation in surface elevation and the resulting water level slope in the two lakes and Ohashi River. This indicates the model's capability to provide a good simulation of tidal and subtidal response of the coupled lake system to variations in meteorological and hydrological forcing.

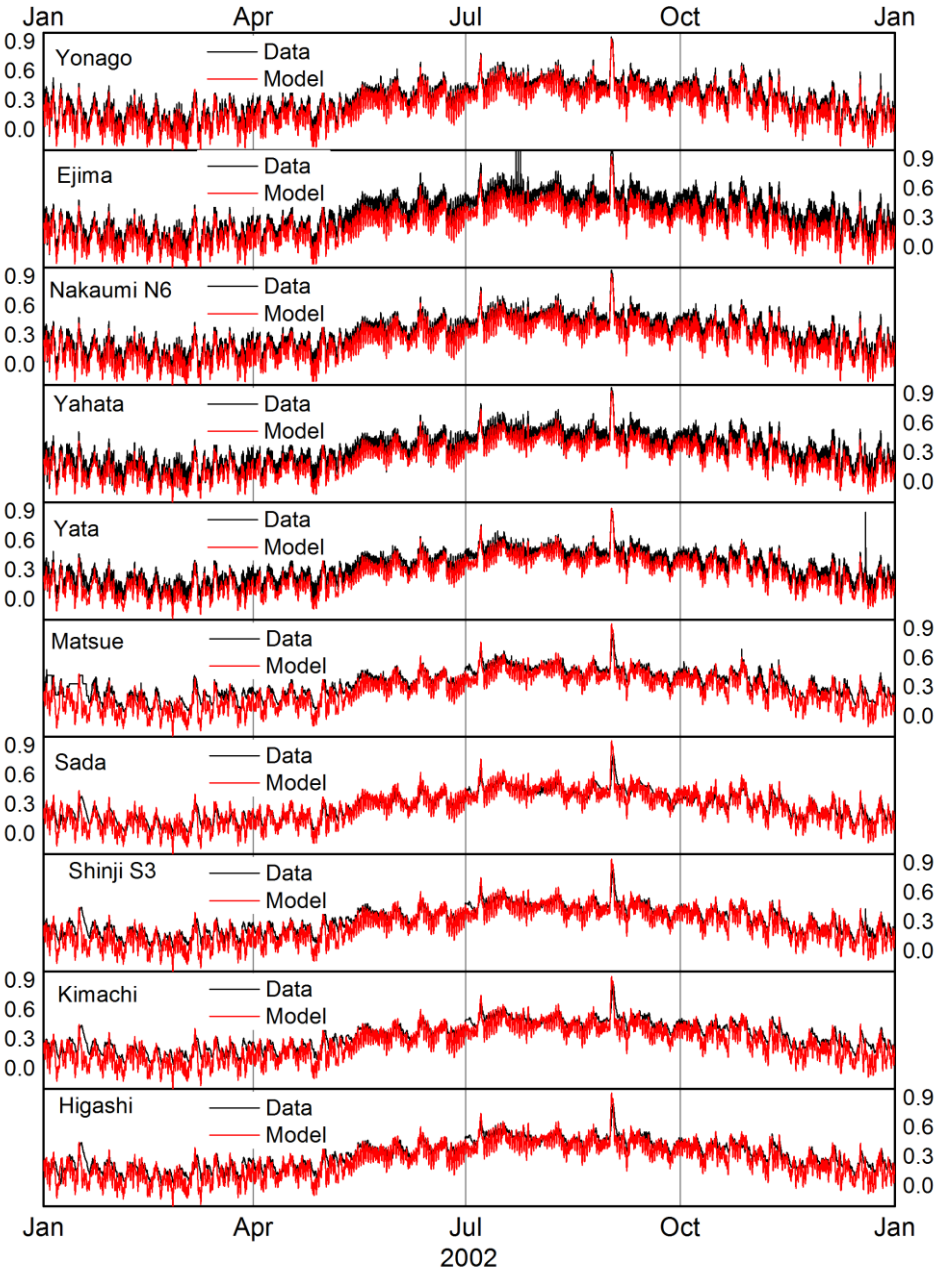

Figure 4.8 Comparison simulation results and observed data for surface elevation at ten water level stations.

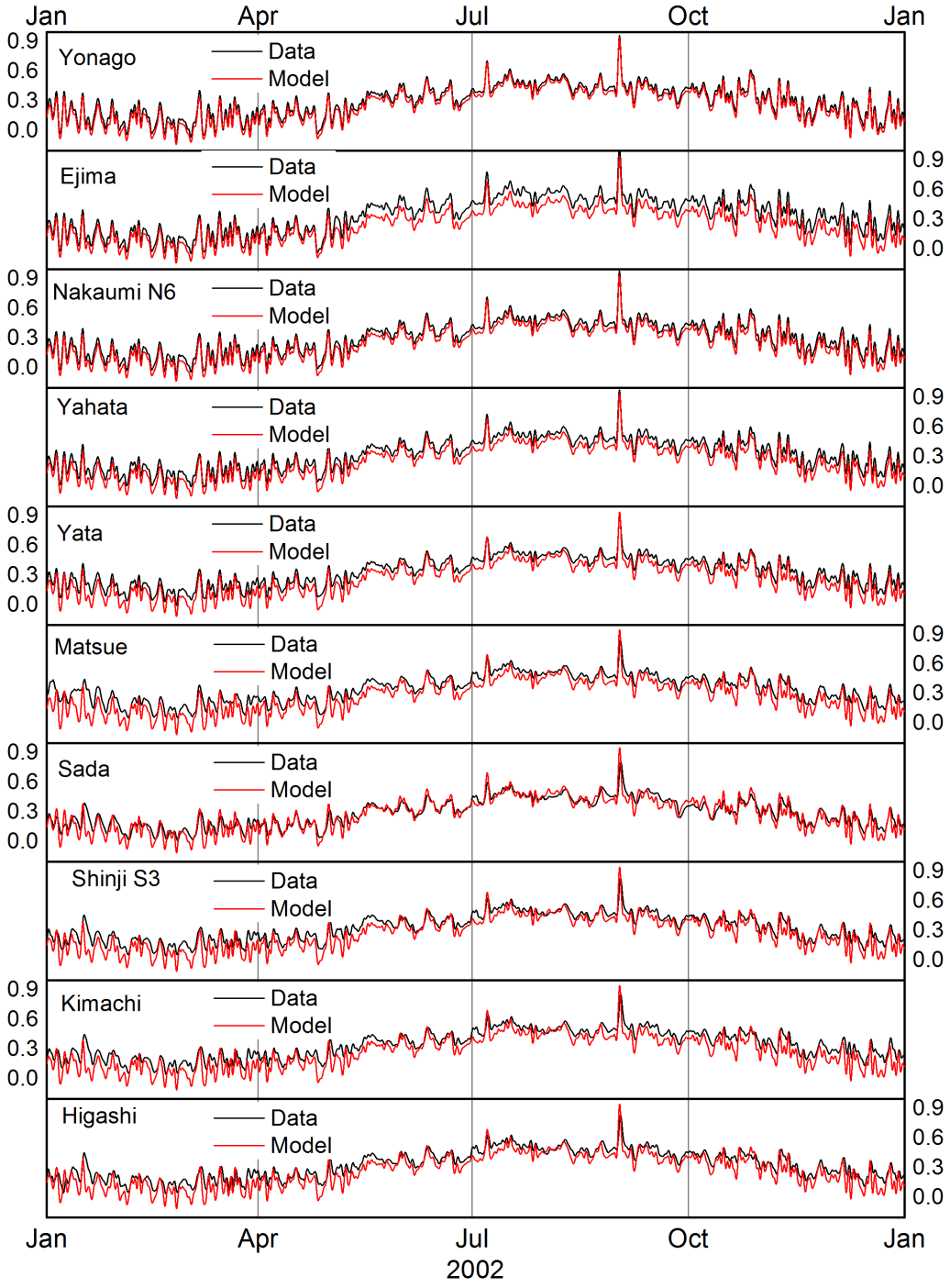

Figure 4.9 Low-pass filtered atmospheric pressure (b) and wind speed (c), Hourly river discharge (a), and simulation result – observed data comparison for subtidal component of surface elevation at seven tide stations (d).

4.3.2 Current velocity

The model managed to reproduce variations in current velocity well (Figure 4.10, Figure 4.11, and Figure 4.12). For the total velocity components, mean error (ME) is large ranging from -13.5 to 3.6 cm/s and mean absolute error (MAE) ranges from 15.9 to 21.6 cm/s (Table 4-3). Both observed data and simulation results show that the *u*-velocity component is comparable in Ohashi River and *v*-velocity component is comparable near the bottom at Nakaura Watergate. The model has medium predictive skills of at least 66% in simulating the *v*-velocities at Nakaura Watergate. The model, however, generally under-predicts surface layer *v*-velocities Nakaura Watergate and over estimates the middle and bottom layer *v*-velocities. In Ohashi River, the model has high predictive skills of at least 75% for the *u*-velocities, however, it tends to under predict. Simulation results show that north-south direction is the principal axis at Nakaura Water and east-west direction is the principal axis at upstream and downstream stations in Ohashi River. This is due to the orientation of the channels at these stations. The current in Ohashi River and at Nakaura Watergate is highly sheared. The velocity shear is as strong as either the surface layer or bottom layer velocity. The simulated and the observed strong velocity shear are in good agreement (Figure 4.10d, Figure 4.11d, and Figure 4.12d). The model generally under-estimated the variations in the subtidal velocity (Figure 4.10e, Figure 4.11e, and Figure 4.12e), with ME ranging from −13.5 to 3.6 cm/s and MAE ranging from 6.2 to 15.3 cm/s (Table 4-3). Most of the time, the modelled and the observed subtidal currents flows in the same direction with the predictive skills of 73% – 78% for middle and bottom *v* velocities at Nakaura Watergate and bottom *u* velocities at Matsue. The

simulation skill is slightly low between 55% and 67% for surface *u* velocity at Matsue and *u* velocities at Yahata. At Nakaura Watergate the skill is low at 47%.

Table 4-3 Error estimates for simulation - observation current velocity results comparison

Variables	**Station**	**Total component**			
		ME	MAE	Skill	N
Current velocity (cm/s)	Nakaura - Surface layer	-10.50	20.24	66%	28464
	Nakaura - Middle layer	1.12	17.77	77%	28464
	Nakaura - Bottom layer	3.63	15.86	80%	28464
	Yahata - surface layer	-7.88	21.18	81%	10189
	Yahata - middle layer	-13.08	21.61	80%	10189
	Yahata - bottom layer	-13.54	21.15	75%	10189
	Matsue - surface layer	-9.19	20.14	77%	10200
	Matsue - middle layer	-10.80	17.85	82%	10200
	Matsue - bottom layer	-3.01	16.77	80%	10200
Subtidal current velocity (cm/s)	Nakaura - Surface layer	-10.49	11.89	47%	28464
	Nakaura - Middle layer	1.13	6.60	73%	28464
	Nakaura - Bottom layer	3.63	6.28	78%	28464
	Yahata - surface layer	-7.88	13.23	66%	10189
	Yahata - middle layer	-13.08	15.25	63%	10189
	Yahata - bottom layer	-13.54	14.45	57%	10189
	Matsue - surface layer	-9.16	12.23	55%	10200
	Matsue - middle layer	-10.78	12.44	67%	10200
	Matsue - bottom layer	-2.99	8.33	77%	10200

The study also endeavoured to analyse the response patterns of current velocity to river discharge in Hii River, wind and atmospheric pressure. A weak to moderate river discharge may drive downstream current in the surface layer but not in the bottom layer, thus increasing velocity shear. This is more evident at Nakaura Watergate than in Ohashi River. River discharges greater than 100 m^3/s can produce downstream current in the bottom layer making a unidirectional currents flow downstream. Both data and model show these two response patterns (Figure 4.10e, Figure 4.11e, and Figure 4.12e). When

river discharge is less than 100 m^3/s (e.g. June 5–July 5), downstream flow (i.e., positive velocity) is more apparent in the surface layer than in the bottom layer. When river discharge is greater than 100 m^3/s (May 31–June 1, July 5–14, and September 6 & 11), downstream flow is apparent in both surface and bottom layers. Sheared current velocity driven by wind and atmospheric pressure is also noted mainly at Nakaura Watergate. The wind-induced and atmospheric pressure-induced current pattern is highly sheared with oppositely directed surface and bottom currents. In Ohashi River the pressure drop coinciding with north-easterly wind results in current flow towards Lake Shinji throughout the water column (June 28, August 10, and September 9). At Nakaura Watergate, north-easterly wind forced current flow towards Lake Nakaumi in the surface layer and towards the Miho Bay in the bottom layer. Both simulation and observed data show that westerly wind of at least 4m/s on June 20–July 5 drives eastward current in Ohashi River and northward current at Nakaura Watergate (i.e., positive velocity) in the water column. Reverse current flow direction is observed with easterly wind. At NW north-easterly wind of almost 5 m/s around September 20 results in the northward current in the bottom layer and southward current in the surface layer.

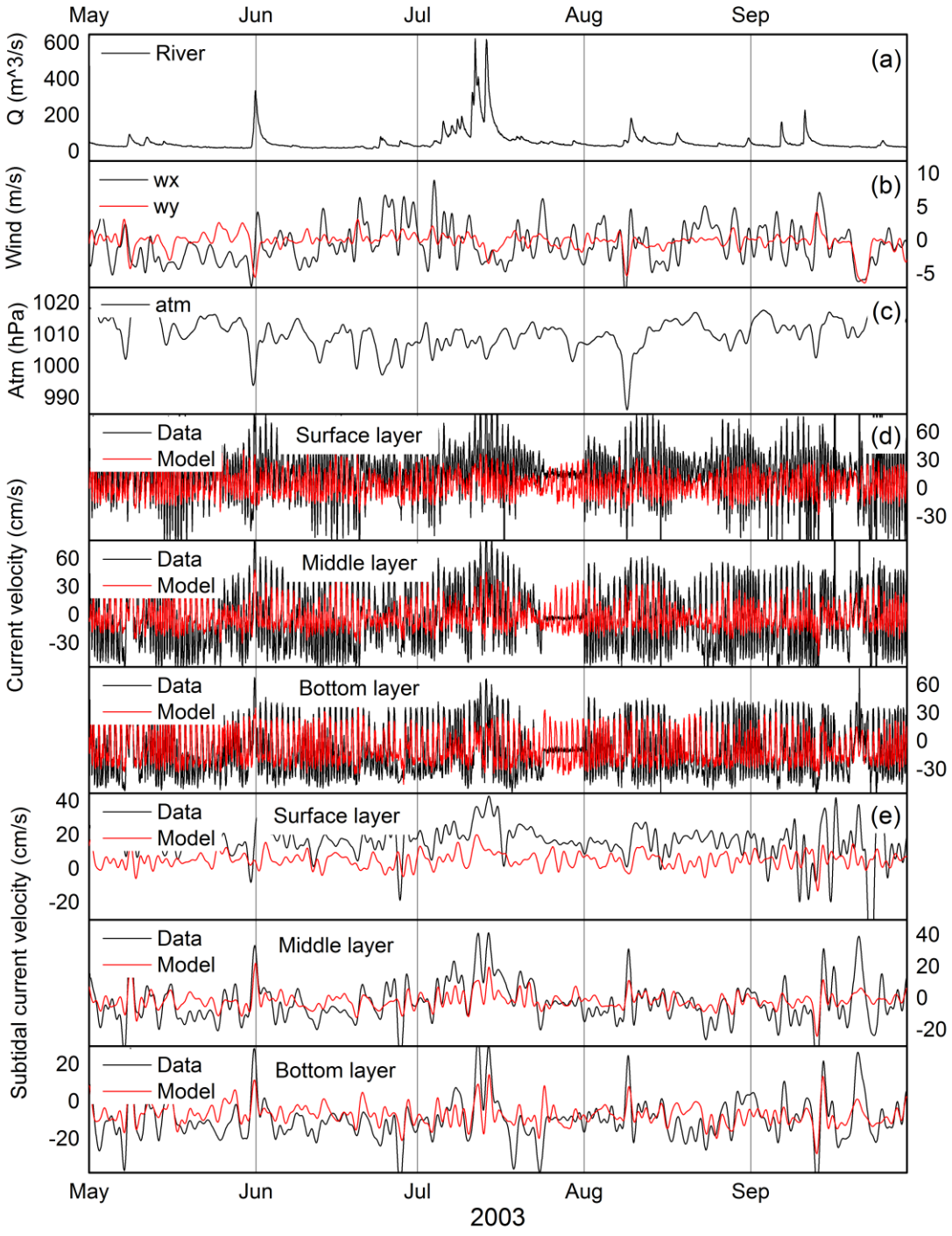

Figure 4.10 Hourly river discharge (a), wind speed (b), and, low-pass filtered atmospheric pressure (c) and simulation – data comparison for current velocity (d), and for subtidal current velocity (e) at Nakaura Watergate.

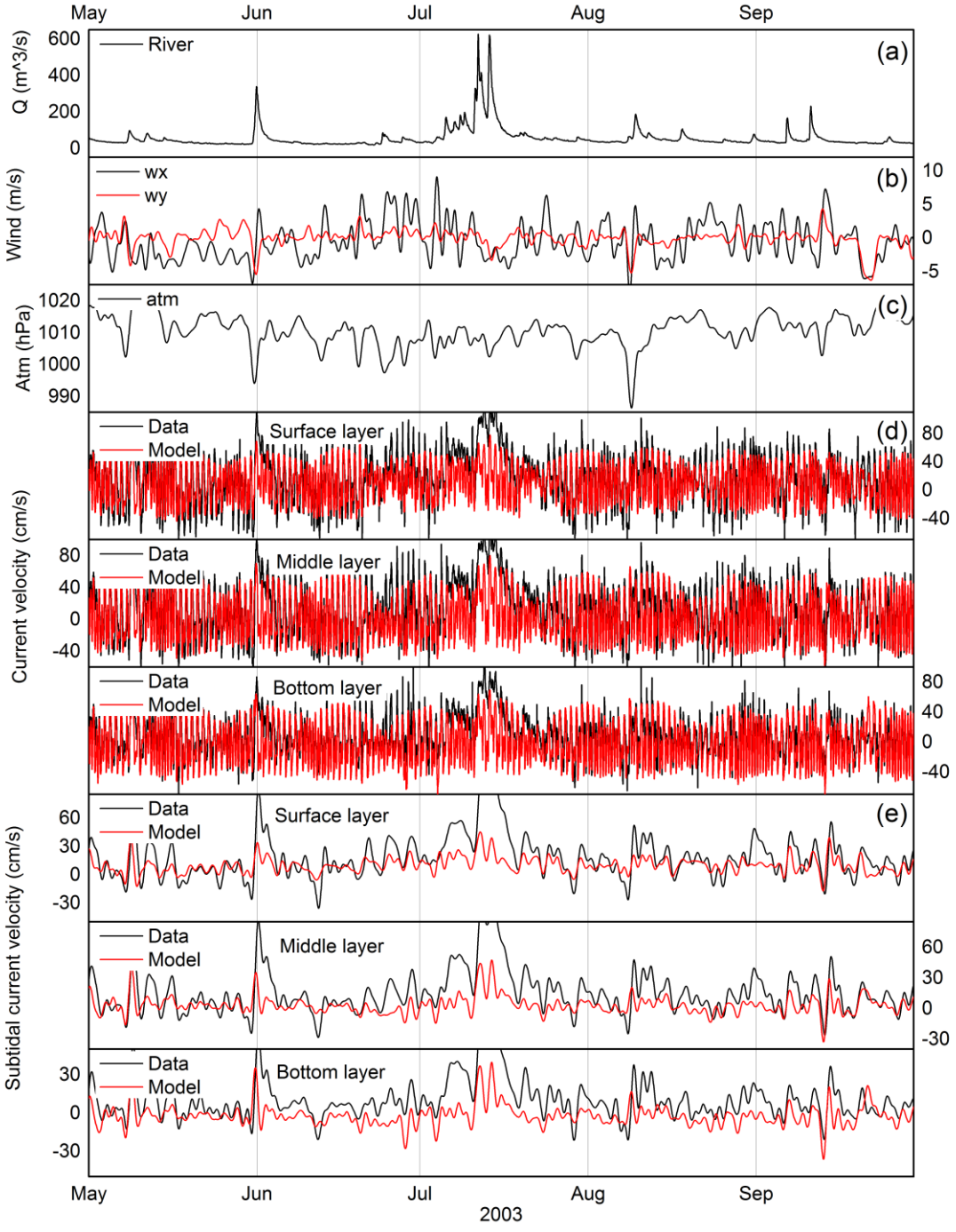

Figure 4.11 Hourly river discharge (a), low-pass filtered wind speed (b), and, atmospheric pressure (c) and simulation – data comparison for current velocity (d), and for subtidal current velocity (e) at Yahata (Ohashi River downstream).

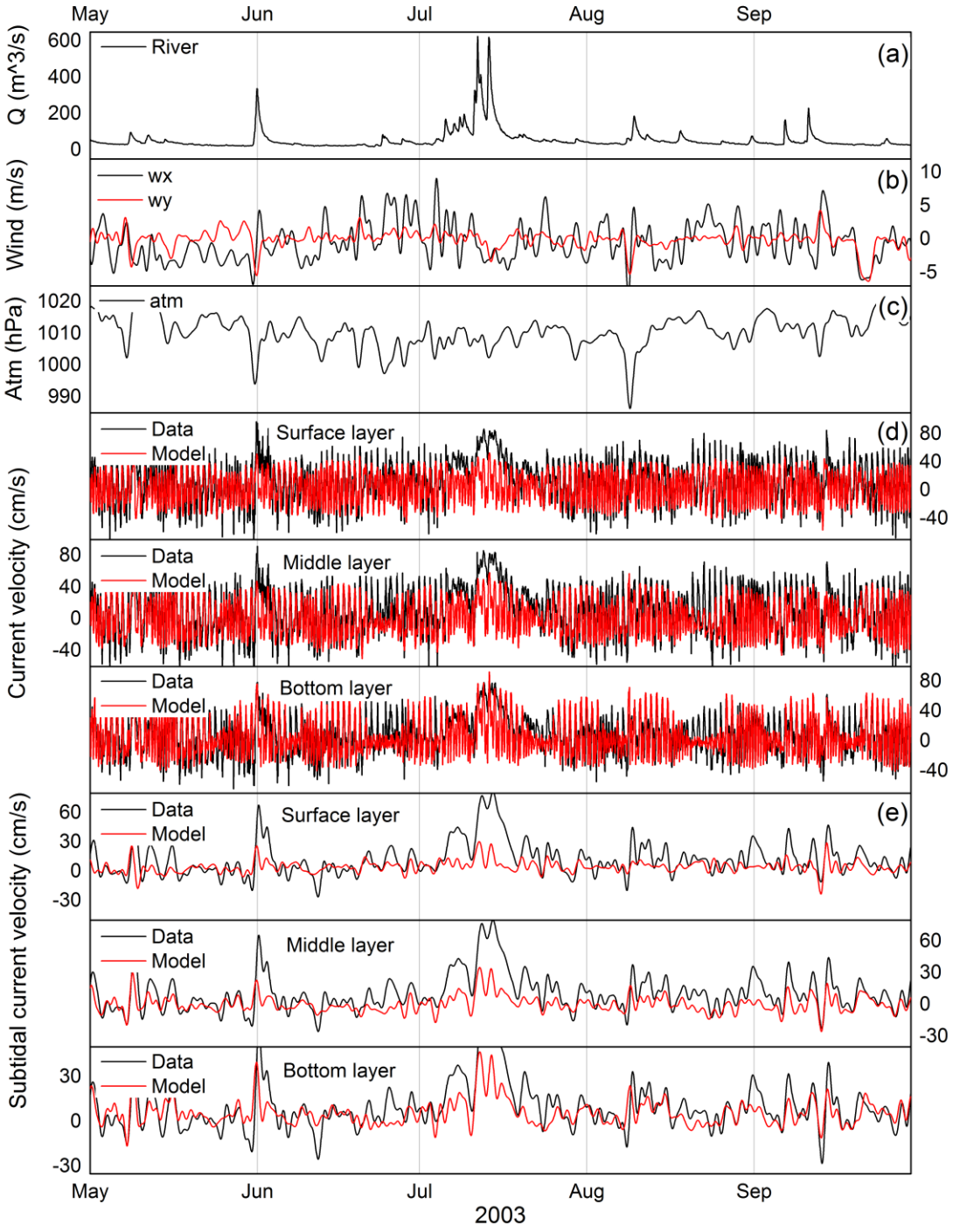

Figure 4.12 Hourly river discharge (a), low-pass filtered wind speed (b), and, atmospheric pressure (c) and simulation – data comparison for current velocity (d), and for subtidal current velocity (e) at Matsue (Ohashi River upstream).

4.3.3 Salinity

The simulations results are somewhat in good agreement with observed salinity. However, the model under-estimate the bottom salinity and over-estimate the surface salinity at Lake Nakaumi mid-lake station (N6) (Figure 4.13a and Figure 4.14d). The under-estimation may be attributed to the salinity open boundary conditions. The model employed a temporally varying open boundary condition for salinity with data collected at Nakaura Watergate (NW), which may not be representative of salinity in Sakai Channel (SC). Thereby not allowing the model to reproduce intrusions of high salinity water from the Japan Sea. The over-estimation of the surface salinity could be result of somewhat inadequate representation of input freshwater as contribution of minor rivers and tributaries was not considered. Both data and model show high bottom salinity virtually constant and surface salinity with distinct variations, indicative of intrusion of high salinity water along the bottom (Figure 4.13a). The model reproduces the observed salinity trend well for both the total and subtidal components. Both data and model show that tidal fluctuation in surface salinity and in bottom salinity is almost the same and river-discharge modulation in subtidal fluctuation of salinity. ME (2.5 psu & -2.9 psu) and MAE (3 psu) are somewhat small, and the model skills are between 64% and 79% for both the total and subtidal components (Table 4-4). The model over-estimated the surface salinity at Matsue (Figure 4.13b and Figure 4.14e). ME (1 psu) and MAE (2 psu) are small, and high model skills are 77% and 82% for the total and subtidal components, respectively (Table 4-4). The surface and middle salinity at Lake Shinji mid-lake station (S3) is over-estimated, starting June 2003 (Figure 4.13c and Figure 4.14f). The over-estimation of salinity at Matsue and S3 may be attributed to the inability of the model to

simulate well the effect of freshwater input from Hii River. The increased river discharge leads to salinity dilution in Lakes Shinji and Nakaumi. Although both the model and data show this dilution, it is weak in the model. The under-estimation of the bottom salinity at S3 is a result of the model not able to simulated acute variations in salinity. For S3, ME (<|1| psu) and MAE (≤2 psu) are small, and high model skills are between 72% and 84% for both the total and subtidal components (Table 4-4).

Table 4-4 Error estimates for simulation - observation salinity results comparison

Variables	**Station**	**Total component**			
		ME	MAE	Skill	N
Salinity (PSU)	Nakaumi N6 - Surface layer	2.46	3.14	77%	8760
	Nakaumi N6 - Bottom layer	-2.94	3.26	66%	8760
	Nakaumi N6 - salinity gradient	-5.40	5.82	70%	8760
	Matsue	1.02	2.21	77%	8760
	Shinji S3 - surface layer	0.71	0.90	83%	8760
	Shinji S3 - middle layer	0.88	1.04	79%	8760
	Shinji S3 - bottom layer	-0.45	2.14	72%	8760
	Shinji S3 - salinity gradient	-1.16	2.06	50%	8760
Subtidal Salinity (PSU)	Nakaumi N6 - Surface layer	2.46	2.96	79%	8760
	Nakaumi N6 - Bottom layer	-2.90	3.20	66%	8760
	Nakaumi N6 - salinity gradient	-5.36	5.60	71%	8760
	Matsue	1.02	1.63	82%	8760
	Shinji S3 - surface layer	0.71	0.88	84%	8760
	Shinji S3 - middle layer	0.88	1.02	79%	8760
	Shinji S3 - bottom layer	-0.45	2.03	74%	8760
	Shinji S3 - salinity gradient	-1.16	1.98	51%	8760

The model reproduces the general trend of bottom-surface salinity difference well for both the total and subtidal components at N6 and S3 (Figure 4.13a(iii), c(iv) and Figure 4.14d(iii), f(iv)) with a ME of -5.4 psu, MAE of 5.6-8 psu, the model skills of 70-71% and ME of -1.2 psu, MAE of 2 psu, the model skills of 50-51%, respectively (Table

4-4). The relatively high predictive skill in the simulation of stratification is encouraging since density stratification in the water column is an important factor influencing salt exchange and circulation. Both observed data and simulation results show strong stratification with maximum salinity difference of about 20 psu at N6, as has been frequently observed in Lake Nakaumi (Nakata et al. 2000; Mizoyama et al. 2011; Okuda 2004; Kishi 2000; Ichikawa et al. 2007; Nomura et al. 2004; Kurokawa & Fukuoka 2003). Huge variation in river discharge during the rainy month of July affects stratification. Relatively strong river flow weakens stratification, sometimes resulting in almost homogeneous water column at both N6 and S3 (e.g., June 1, July 5-14). Complete destruction of stratification is often observed in Lake Shinji. When there is little river discharge variation, stratification is mainly affected by wind conditions. Relatively strong wind weakens and/or strengthens stratification, sometimes resulting in a homogeneous/heterogeneous water column dependent on the location. For example, a strong north-easterly wind observed around September 20 resulted in the destruction of stratification in Lake Nakaumi (Figure 4.13a(iii) and Figure 4.14d(iii)). In Lake Shinji relatively strong south-westerly wind resulted in the evolution of stratification around September 15 (Figure 4.13c(iv) and Figure 4.14f(iv)). Persistent relatively strong westerly wind from June 26 to July 10 results in the weakening of stratification in Lake Nakaumi and Lake Shinji. On the subtidal time scale, both data and model show that stratification is rarely less than 10 psu in Lake Nakaumi and rarely more than 5 psu in Lake Shinji. Vertical mixing has the potential to redistribute solutes and passive particulate materials, altering their net horizontal transport and distribution (Kim & Park 2012). Baroclinic circulation, and thus mass transport may be modified by vertical mixing variation (Kim & Park 2012). Although a good reproduction of stratification and vertical

mixing in Lakes Shinji and Nakaumi has not been achieved, the results obtained are encouraging.

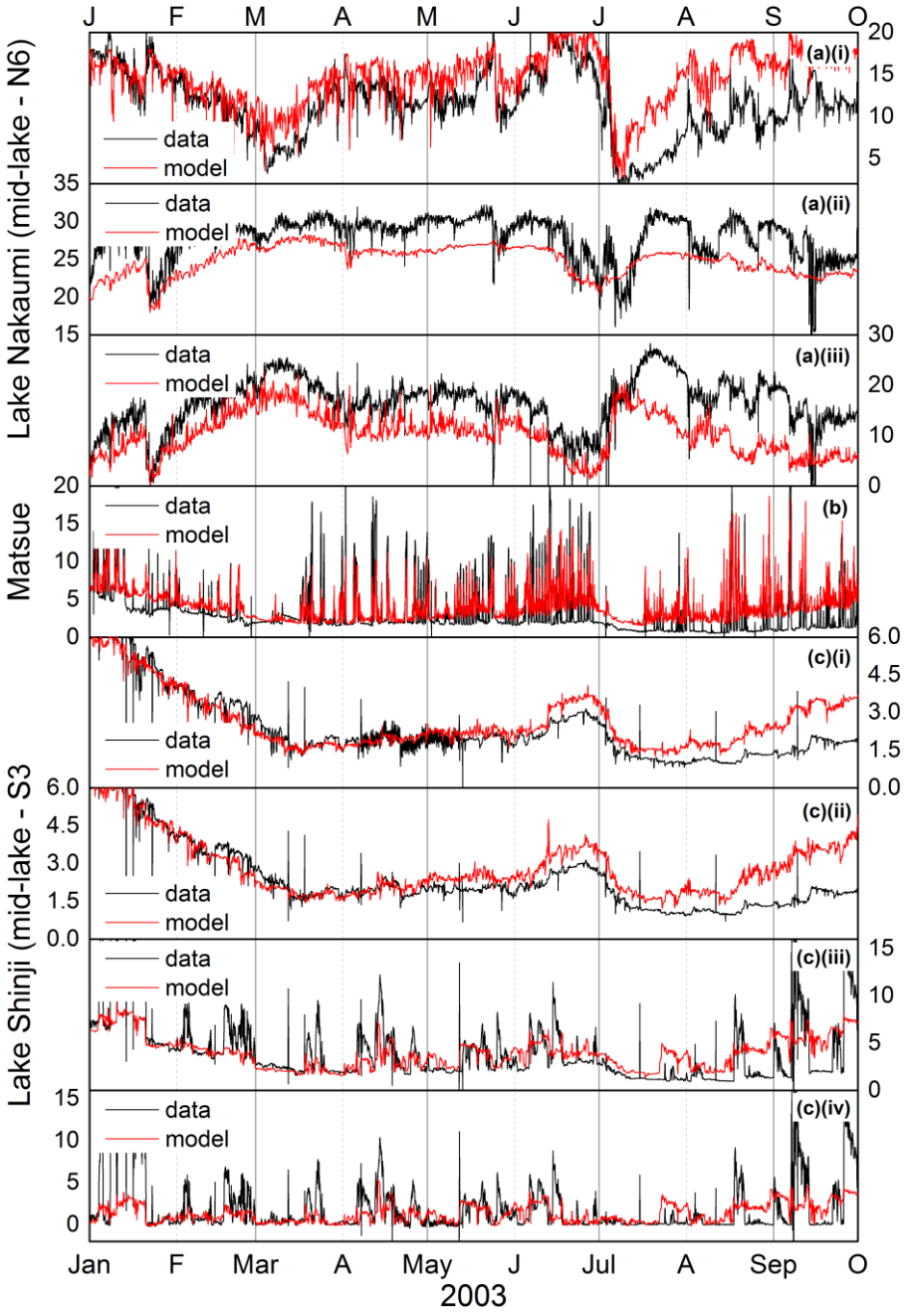

Figure 4.13 Simulation – data comparison for salinity at mid-lake stations in Lake Nakaumi (a), and Lake Shinji (c) and at Matsue (b).

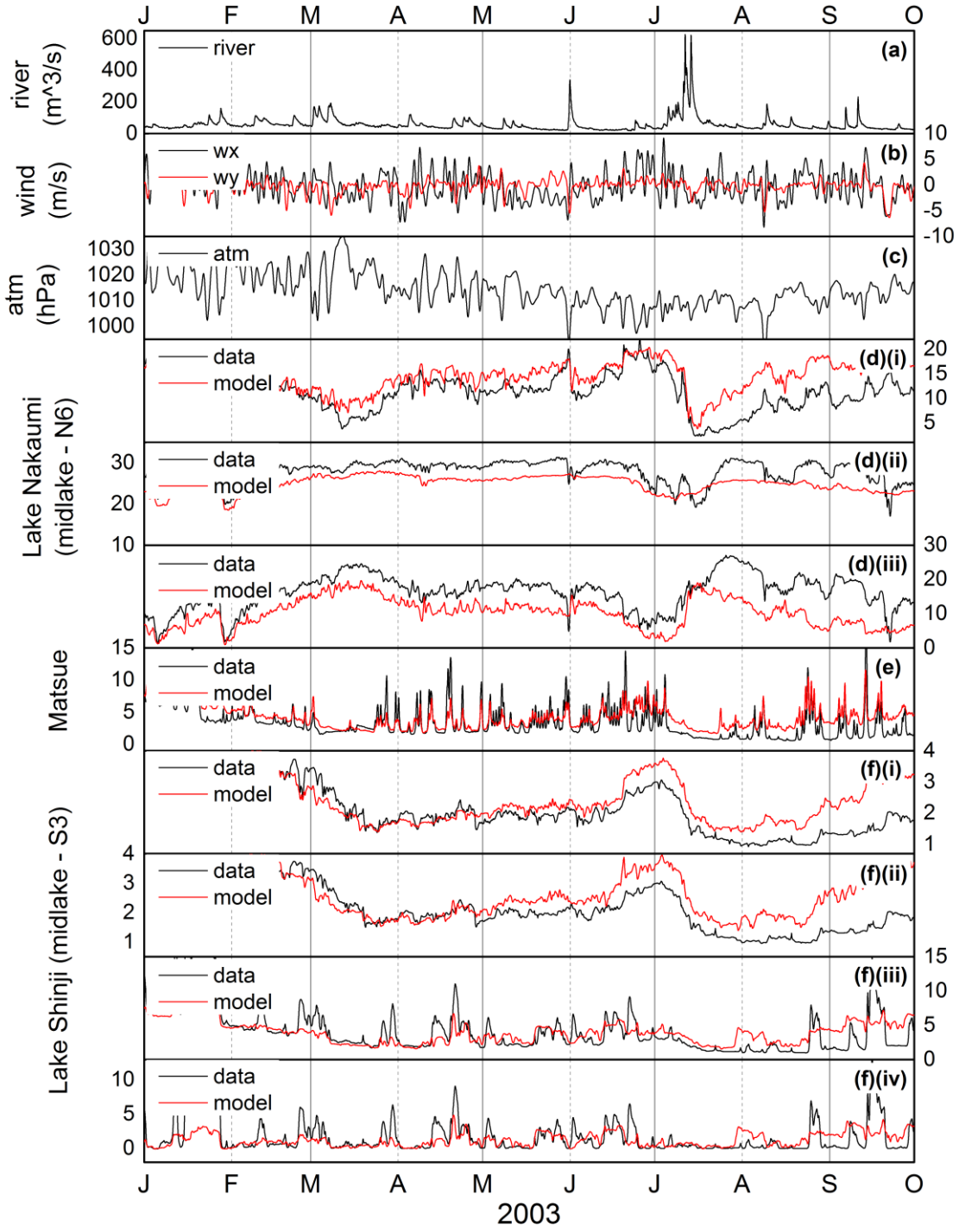

Figure 4.14 Hourly river discharge (a), low-pass filtered wind speed (b), and, atmospheric pressure (c) and simulation – data comparison for subtidal salinity at mid-lake stations in Lake Nakaumi (d) and Lake Shinji (f) and at Matsue (e)

4.4 FORMULATION OF THE EQUATIONS FOR SALT FLUXES

4.4.1 Fluxes Across a Vertical Cross Section

The equations originally derived by Hansen (1965) were used in conducting the analysis of the processes governing the flux of materials along the west-east direction in Lakes Shinji and Nakaumi (hereinafter referred to as longitudinal direction) (Hughes 1968). Many studies have applied these equations to analyse of the longitudinal flux of materials (Hughes 1968; Hughes & Rattray 1980; Hansen 1965; Dyer 1974; Dyer et al. 1992).

The mean velocity or, mean value of any variable over the cross section is given by

$$\bar{u}(x,t) = \frac{1}{A}\iint u(x,y,z,t)dA \tag{4-85}$$

where A is the cross-sectional area at time t, $u(x,y,z,t)$ is the instantaneous seaward component of velocity at any point on a cross section normal to the longitudinal axis of the Lake. Denoting $u_d(x,y,z,t)$ as the local deviation from sectional mean,

$$u(x,y,z,t) = \bar{u}(x,t) + u_d(x,y,z,t) \tag{4-86}$$

and the water flux through the section is

$$F_w(x,t) = \iint u(x,y,z,t)dA = A\bar{u}(x,t) \tag{4-87}$$

Since the all quantities change with time, their variations can be defined in terms of three time scales which can be recognized from the data. These are tidal mean, tidal fluctuation and turbulent fluctuation. The variations can then be expressed as follows:

$$\bar{u} = \langle \bar{u} \rangle + \bar{u}_p + \bar{u}' \qquad A = \langle A \rangle + A_p + A' \tag{4-88}$$

where subscript p denotes the major harmonic variations, and primes denote turbulent fluctuations, the angle brackets denote mean values over the tidal period T, i.e.,

$$\langle \bar{u} \rangle = \frac{1}{T} \int_0^T \bar{u}\, dt \qquad \langle A \rangle = \frac{1}{T} \int_0^T A\, dt \tag{4-89}$$

The mean water flux through the cross section during the tidal cycle is

$$\langle F_w \rangle = \langle A \bar{u} \rangle \tag{4-90}$$

substituting equation (4-88) into equation (4-90) gives

$$\langle F_w \rangle = \langle \big(\langle A \rangle + A_p + A' \big) \big(\langle \bar{u} \rangle + \bar{u}_p + \bar{u}' \big) \rangle \tag{4-91}$$

Simplification after the expansion and assuming that turbulent fluctuations and tidal fluctuations are uncorrelated gives:

$$\langle F_w \rangle = \langle A \rangle \langle \bar{u} \rangle + \langle A_p \bar{u}_p \rangle + \langle A' \bar{u}' \rangle \tag{4-92}$$

The term $\langle A \rangle \langle \bar{u} \rangle$ is the seaward water flux through the mean cross-sectional area carried by the mean flow, usually referred to as the non-tidal drift. The flux $\langle A_p \bar{u}_p \rangle$ is due

to tides and is generally landward. The turbulent flux, $\langle A'\overline{u}'\rangle$, represent water transport by motions of less than semidiurnal period, is generally negligible.

With molecular diffusion disregarded, the instantaneous salt flux through a vertical cross section normal to the mean flow is given by

$$F_s(t) = \iint usdA = A(\bar{u}\bar{s} + \overline{u_d s_d}) \tag{4-93}$$

with the quantities defined as before.

The term $A\bar{u}\bar{s}$ expresses the instantaneous salt flux due to the sectional mean current and salinity. This term, therefore, reverses direction in the presence of a strong tidal current, but, in strictly stationary conditions, it represent the seaward salt advection by the freshwater discharge mode of circulation. The term $A\overline{u_d s_d}$ is due to a correlation between the local deviations of salinity and current from their respective means. Under strictly stationary conditions, this term represents an upstream salt flux due to gravitational convection currents. It has been called the "shear effect" and is a result primarily of density currents and velocity shear induced in tidal currents by bottom friction.

Instantaneous salt fluxes are a sum of cross sectional average and deviations therefrom. Assuming non-stationary conditions, the mean salt flux over a tidal cycle is

$$\langle F_s\rangle = \frac{1}{T}\int_0^T F_s(t)\,dt = \langle A\bar{u}\bar{s}\rangle + \langle A\overline{u_d s_d}\rangle \tag{4-94}$$

The cross-sectional salinity averages, and deviations from the mean salt flux can also be considered as the sum of a tidal mean, a tidal fluctuation and a turbulent fluctuation. The velocity, salinity, mean deviation product of velocity and salinity, and cross-sectional area vary with in time. The shear effect can be separated into lateral and vertical components (Dyer 1974; Dyer et al. 1992). Further, considering three dimensional profiles the deviations of velocity and salinity from the cross-sectional mean, can be separated into variations in the vertical transverse directions. Thus

$$u_d = \langle u_d \rangle + (u_d)_p \qquad \langle u_d \rangle = \langle u_{dt} \rangle + \langle u_{dv} \rangle \qquad (u_d)_p = u_t + u_v \quad (4\text{-}95)$$

where u_{dt} is the deviation of the depth averaged velocity at any position from the cross sectional mean velocity, and u_{dv}, is the deviation of the mean velocity at any depth from the depth averaged velocity value u_{dt}. The same procedure applies for salinity. Thus the mean salt flux over a tidal cycle through a cross section is given by:

$$\begin{aligned}\langle F_s \rangle = & \underbrace{\langle A \rangle \langle \bar{u} \rangle \langle \bar{s} \rangle}_{1} + \underbrace{\langle A_p \bar{u}_p \rangle \langle \bar{s} \rangle}_{2} + \underbrace{\langle A_p \bar{s}_p \rangle \langle \bar{u} \rangle}_{3} + \underbrace{\langle A \rangle \langle \bar{u}_p \bar{s}_p \rangle}_{4} + \underbrace{\langle A_p \bar{u}_p \bar{s}_p \rangle}_{5} \\ & + \underbrace{\langle A \rangle \overline{\langle u_{dt} \rangle \langle s_{dt} \rangle}}_{6} + \underbrace{\langle A \rangle \overline{\langle u_{dv} \rangle \langle s_{dv} \rangle}}_{7} + \underbrace{\langle A \rangle \overline{\langle u_t s_t \rangle}}_{8} + \underbrace{\langle A \rangle \overline{\langle u_v s_v \rangle}}_{9} \\ & + \underbrace{\langle \overline{A_p u_t s_t} \rangle}_{10} + \underbrace{\langle \overline{A_p u_v s_v} \rangle}_{11}\end{aligned} \quad (4\text{-}96)$$

where the bars indicate cross-sectional averages and angle brackets indicate a time-average. Terms 1-5 quantify advection, and terms 6-11 quantify the shear effect associated with the variation in salinity and velocity within the cross section. Terms 1 and 2 provide the flux on the “non-tidal” drift. Terms 2-5 account for what is called “tidal pumping”, associated fluxes due to phase differences in the cross sectional averages of

the tidal variations in velocity, salinity and cross sectional area (Dyer et al. 1992). Physical processes related with the terms of equation (4-96) are listed in Table 4-5.

Table 4-5 Physical processes related with the terms of equation (4-96)

Term	Physical processes
1.	The flux associated with the river discharge
2.	The compensating flow for the inward transport on the partially progressive tidal wave, the stokes drift
3.	The correlation of tidal period variation of tidal height and salinity
4.	The correlation of tidal period variations of salinity and current
5.	The third order correlation of tidal period variations in salinity, velocity and cross-sectional area
6.	The contribution of the net transverse circulation
7.	The net vertical circulation
8.	The transverse oscillatory shear
9.	The vertical oscillatory shear
10.	The covariance of tidal fluctuations in cross-sectional area and the transverse oscillatory shear.
11.	The covariance of tidal fluctuations in cross-sectional area and the vertical oscillatory shear.

The shear effect term $A\overline{u_d s_d}$ in equation (4-93) is due to both density currents and to velocity shear induced in the tidal currents by bottom friction. Hence, equation (4-96) does not completely separate the advective processes from the tidal processes. Under strictly stationary conditions, the term $A\bar{u}\bar{s}$ in equation (4-93) represents the seaward salt advection by the freshwater discharge mode of circulation whilst the shear effect term $A\overline{u_d s_d}$, represents an upstream salt flux due to gravitational convection currents. Assuming that stationary conditions exist for averages over a complete tidal cycle, a method of estimating the magnitude of the density currents is available (Hughes 1968).

Cross sectional measurements in terms of equation (4-96) can be analysed by assuming that the primary variation is either in the transverse direction or in the vertical direction. With the first option the transverse deviations are evaluated first and with the second option it is the vertical deviations that are evaluated first.

4.4.2 Effective Coefficient of Horizontal Eddy Diffusion

The effective coefficient of horizontal eddy diffusion can be estimated assuming that the salt transport required to balance the net advective salt flux is due to the longitudinal eddy diffusion. The tidally averaged conditions are also assumed not to vary with time. Integration of the local flux ($\langle u\rangle\langle s\rangle$), and the incremental area dA through which this local flux is taking place can be used to calculate the total net advective salt flux. Under steady-state net salt flux, the coefficient of horizontal eddy diffusion is given by:

$$K_x = \frac{\iint \langle u\rangle\langle s\rangle \, dA}{\langle A\rangle \frac{d\bar{s}}{dx}} \tag{4-97}$$

The coefficient obtained from equation (4-97) is not the mean value of the diffusion coefficient. It is a function which, can describe the distribution of the mean salt content in time and space (Hughes 1968).

Assuming a steady state situation, the dispersive upstream flux is defined by the total contribution of terms 6-9 in equation (4-96), should balance the downstream flux due to river discharge (Dyer et al. 1992; Dyer 1974). The effective coefficient of horizontal eddy diffusion, K_x is:

$$K_x = \frac{\sum terms\ 6-9}{\langle A \rangle \frac{d\bar{s}}{dx}} \tag{4-98}$$

Neglecting transport by mixing is compared with advective transport, then longitudinal salinity gradient (Uncles et al. 1990):

$$\frac{\partial \bar{s}}{\partial t} = -\bar{u}\frac{\partial \bar{s}}{\partial x} \qquad \frac{\partial \langle \bar{s} \rangle}{\partial t} = -\langle \bar{u} \rangle \frac{\partial \bar{s}}{\partial x} \tag{4-99}$$

$$\frac{\partial \bar{s}}{\partial x} = \frac{\frac{\partial \bar{s}}{\partial t} - \frac{\partial \langle \bar{s} \rangle}{\partial t}}{\langle \bar{u} \rangle - \bar{u}} \tag{4-100}$$

where *t* is time and *x* is distance along the lake.

4.4.3 Effective Coefficient of Vertical Eddy Diffusion

The effective coefficient of vertical eddy diffusion is given by: (Hughes 1968)

$$K_z(z) = \frac{\langle \bar{w}_y \rangle \langle \bar{s}_y \rangle + \int_0^z \frac{1}{w}\frac{\partial}{\partial x}\left(w\langle \overline{us}_y \rangle\right)dz}{\frac{d\bar{s}_y}{dz}} \tag{4-101}$$

where *w* is the width of the estuary at depth *z*. The subscript *y* denotes that the average is taken over the lateral coordinate. This equation assumes steady state transfer of salt across the entire cross section.

4.5 RESULTS

4.5.1 Cross Sectional Salt Fluxes Results

4.5.1.1 General

Table 4-6 Mean tidally averaged cross sectional area, velocity and salinity

	Mean
Mean Area (m^2)	15717.77±646.40
Mean Velocity (cm/s)	0.09±0.73
Mean Salinity (PSU)	4.65±2.59

Tidally averaged cross sectional salinity ((Figure 4.17 and Figure 4.18) shows that salinity is higher during the winter season than during the summer season. This may be due to reduced river discharge during the winter period. The river discharge, wind and atmospheric pressure regulates salinity levels during both periods. An increase in river discharge ($100m^3/s$) tends to dilute surface salinity and promote intrusion along the bottom layer e.g. around December 18, 2002 (Figure 4.17). At the same time, north-westerly wind (5m/s) and pressure drop (15hPa) tends to drive surface water out of Lake Shinji and bottom water into the lake. The maximum response of the lake to westerly winds occurred in the deep water at the centre of the cross section at Stations 3 and 4 during winter time, e.g. December 10, 2002 and January 5, 2003 (Figure 4.17). Nearly all deep water stations responded to alternating westerly and easterly winds during 2003 summer time, from June 22 to July 13 (Figure 4.18). The bottom salinity during the summer time dropped by about 6 PSU in response to westerly winds and increased by the same amount under the influence of the easterly winds. The surface salinity reduced only gradually by about 2 PSU.

Stratification is more stable during the winter time than during summer. Maximum stratification occurred around high water and minimum stratification around low water. This results from vertical shear, whereby, during high river discharge and low pressure, low salinity water advection down estuary is faster in the surface layers, maximising stratification at high water.

The mean cross sectional area was 15,718 m^2. The calculated cross sectional area showed a fluctuation of about ±4%. There was evidence that the cross sectional area increased in response to increased river discharge and atmospheric pressure drop events. The mean velocities $\langle \bar{u} \rangle$ showed a very large variation at in response to river discharge, wind and atmospheric pressure (Figure 4.15 and Figure 4.16).

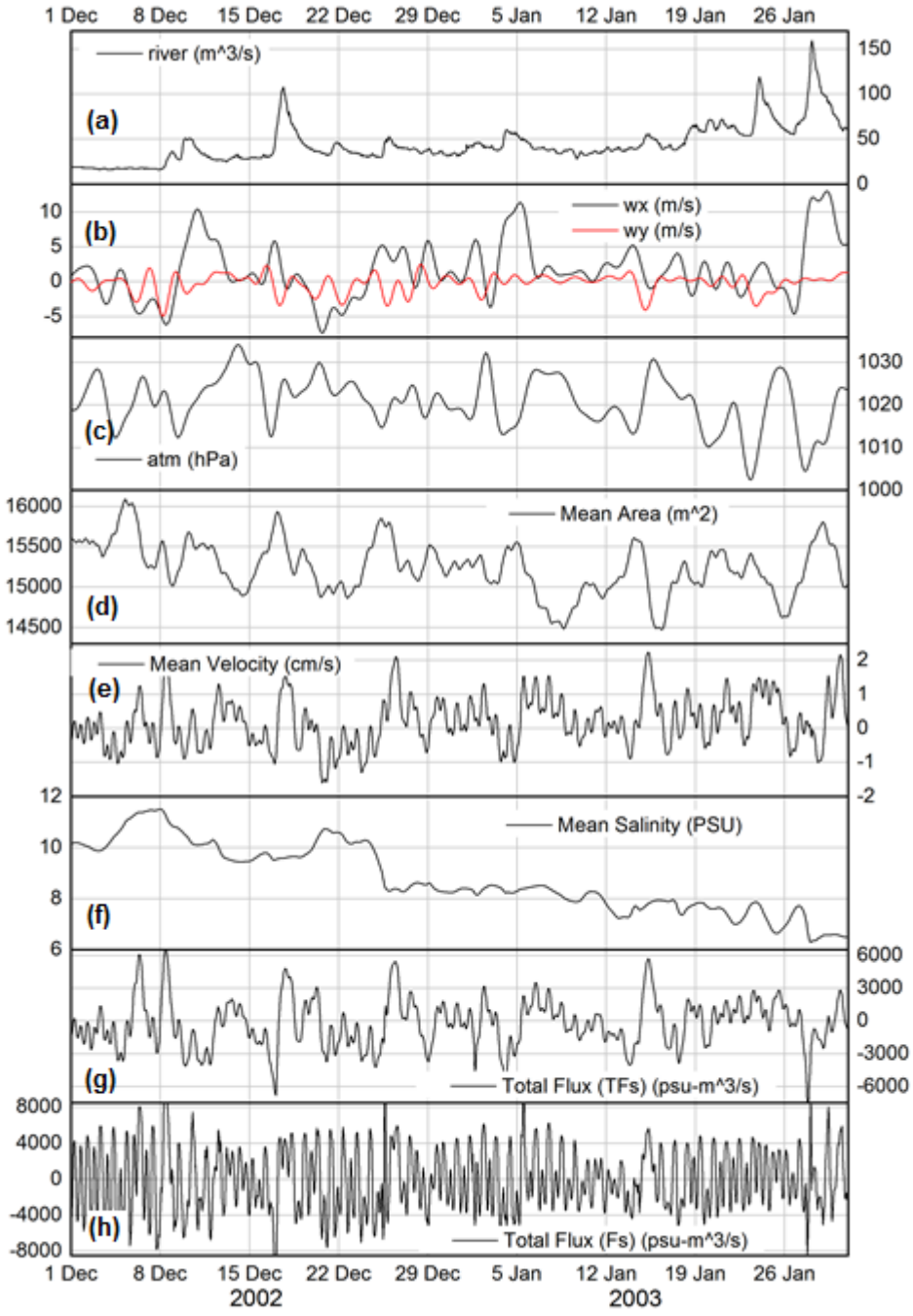

Figure 4.15 Time series of river discharge (a), low-pass filtered wind speed (b), and, atmospheric pressure (c) and tidally averaged cross sectional area (d), mean velocity (e), mean salinity (f), total salinity flux (g) and tidally averaged instantaneuous salinity flux (h) for the winter period December 2002 – January 2003 in Lake Shinji

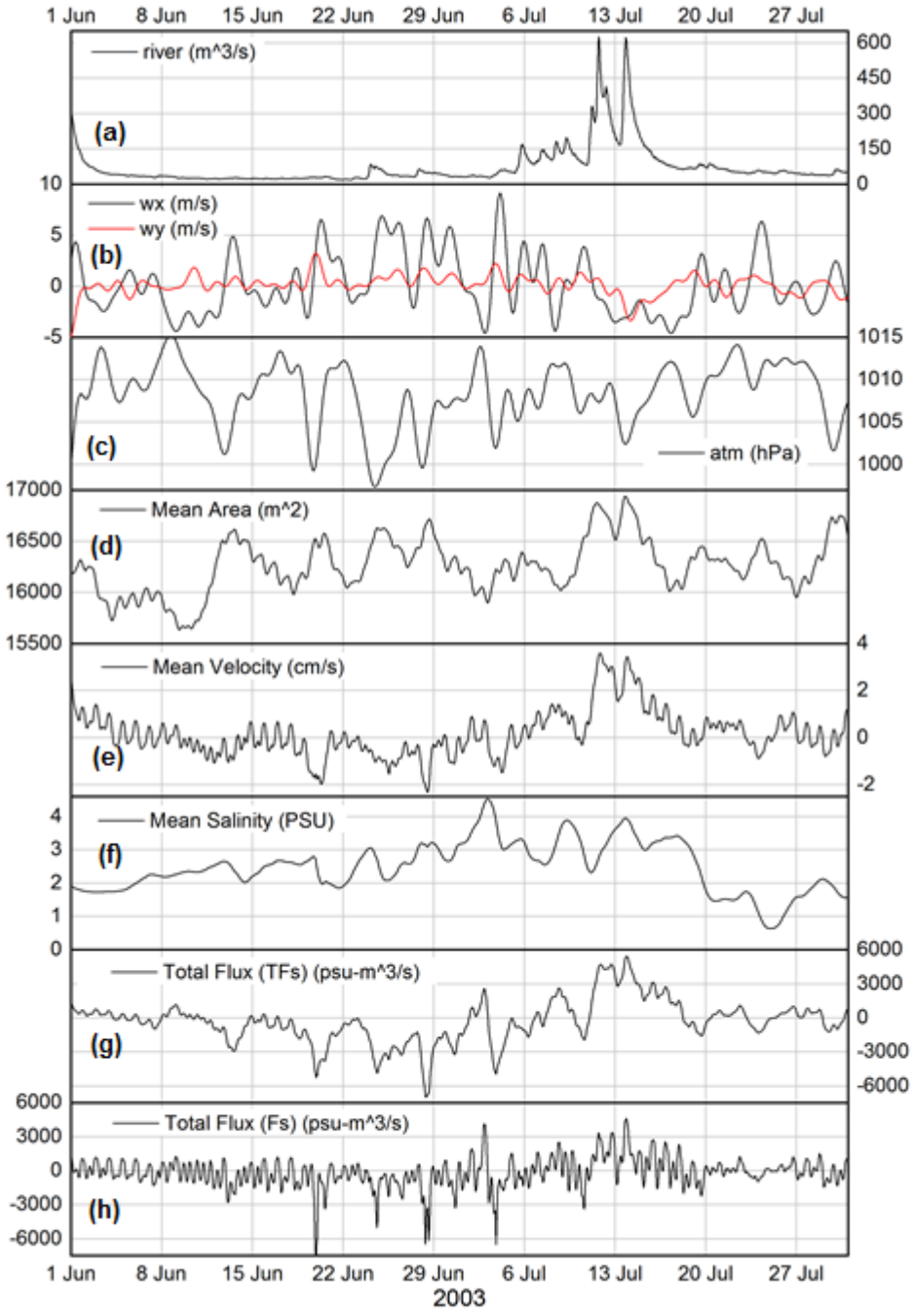

Figure 4.16 Time series of river discharge (a), low-pass filtered wind speed (b), and, atmospheric pressure (c) and tidally averaged cross sectional area (d), mean velocity (d), mean salinity (e), total salinity flux (f) and tidally averaged instantaneuous salinity flux (g) for the summer period June – July 2003 in Lake Shinji

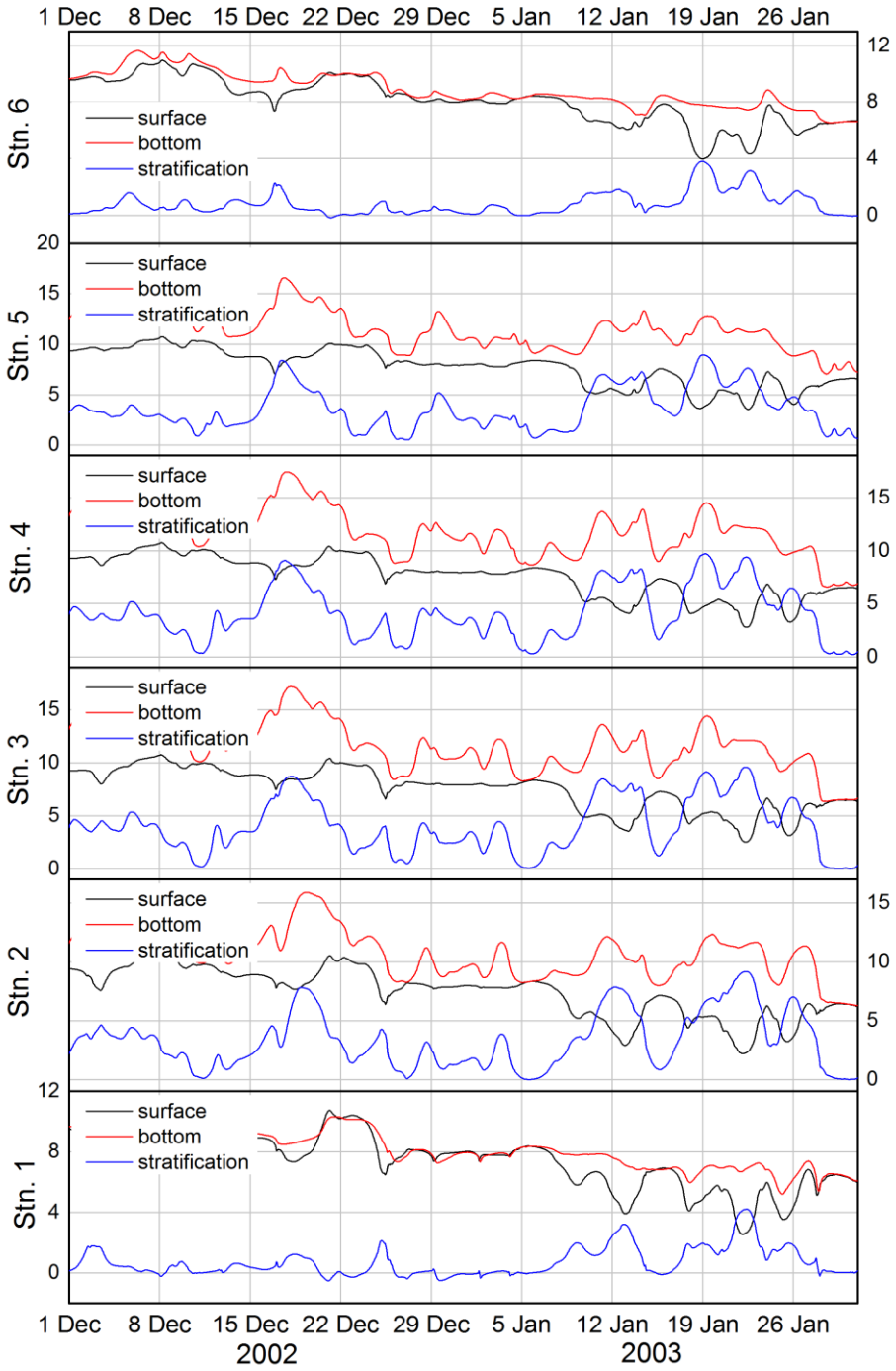

Figure 4.17 Time series of the surface (black line), and bottom (red line) salinity variation and salinity stratification, (the difference between the surface and bottom salinities) (blue line) along section ***A-B*** (Figure 4.6) for the winter period December 2002 – January 2003 in Lake Shinji. Station 1 (station 6) is on the south (north) bank.

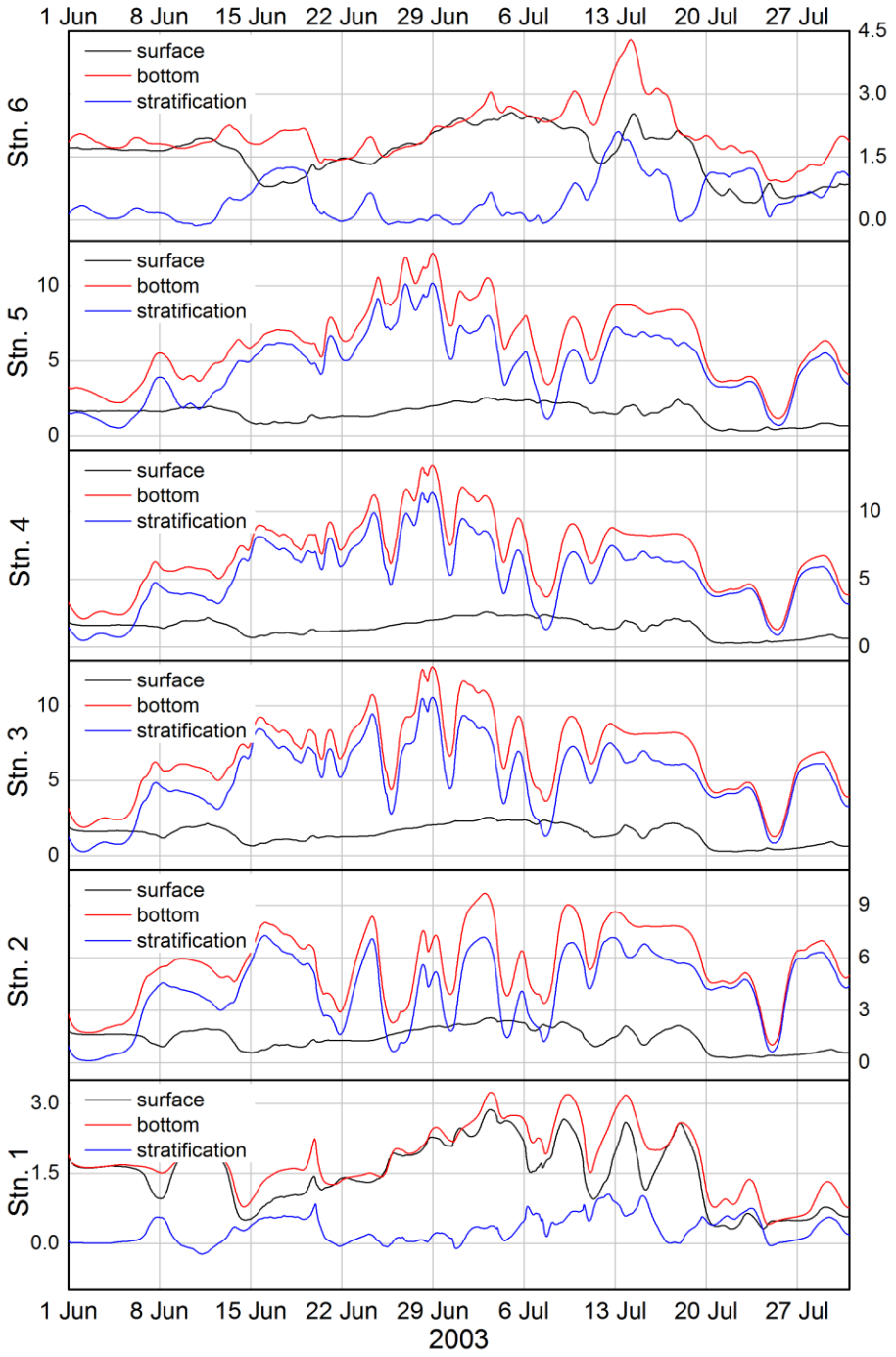

Figure 4.18 Time series of the surface (black line), and bottom (red line) salinity variation and salinity stratification, (the difference between the surface and bottom salinities) (blue line) along section ***A-B*** (Figure 4.6) for the summer period June – July 2003 in Lake Shinji. Station 1 (station 6) is on the south (north) bank.

4.5.1.2 Salt balance

The contributions to the salt flux as given in equation (4-96) were evaluated and are shown in Table 4-7.

Table 4-7 Mean cross sectional salt flux

	Formulae	Mean	Total	outflow	inflow
Term 1 (‰m³/s)	$\langle A\rangle\langle\bar{u}\rangle\langle\bar{s}\rangle$	31.61±610.55	9.00E+05	34.9%	17.6%
Term 2 (‰m³/s)	$\langle A_p\bar{u}_p\rangle\langle\bar{s}\rangle$	-0.99±3.50	-2.82E+04	0.1%	0.1%
Term 3 (‰m³/s)	$\langle A_p\bar{s}_p\rangle\langle\bar{u}\rangle$	11.60±23.94	3.30E+05	2.2%	0.2%
Term 4 (‰m³/s)	$\langle A\rangle\langle\bar{u}_p\bar{s}_p\rangle$	-0.01±0.37	-2.06E+02	-	-
Term 5 (‰m³/s)	$\langle A_p\bar{u}_p\bar{s}_p\rangle$	0.05±0.35	1.37E+03	-	-
Term 6 (‰m³/s)	$\langle A\rangle\overline{\langle u_{dt}\rangle\langle s_{dt}\rangle}$	-104.01±220.61	-2.96E+06	5.4%	13.1%
Term 7 (‰m³/s)	$\langle A\rangle\overline{\langle u_{dv}\rangle\langle s_{dv}\rangle}$	-416.02±882.42	-1.18E+07	21.8%	52.5%
Term 8 (‰m³/s)	$\langle A\rangle\overline{\langle u_t s_t\rangle}$	-0.01±32.04	-2.69E+02	1.2%	0.7%
Term 9 (‰m³/s)	$\langle A\rangle\overline{\langle u_v s_v\rangle}$	48.11±574.03	1.37E+06	34.3%	15.6%
Term 10 (‰m³/s)	$\langle\overline{A_p u_t s_t}\rangle$	-0.06±0.46	-1.62E+03	-	-
Term 11 (‰m³/s)	$\langle\overline{A_p u_v s_v}\rangle$	-1.33±5.87	-3.80E+04	0.1%	0.2%
Total (‰m³/s)	$\sum terms\ 1-11$	-431.07±1852.17	-1.23E+07		
Total (Fs) (‰m³/s)	$A(\bar{u}\bar{s}+\overline{u_d s_d})$	-231.89±2131.54	-6.60E+06		

The sum of the fluxes given by Table 4-7 must equal the difference between the change in salt storage upstream of the section during the period and the flux through the section due to the turbulent fluctuation terms which are shown in equation (4-96). From Table 4-7 it is evident that the average contribution of Terms 2, 4, 5, 8, 10 and 11 is negligible.

The overall mean value corresponding to a net salt discharge from Lake Shinji was 31.61‰m³/s with a standard deviation of 610.55‰m³/s. The net advection (Term 1) follows very closely the variation in river discharge, wind and atmospheric pressure

(Figure 4.19 and Figure 4.20). Westerly wind drive "Term 1" salinity flux upstream and easterly the opposite direction.

4.5.1.3 The tidal terms

The flux on the Stokes Drift (Term 2) is small with a maximum of ±52‰m^3/s. Although it is of an order much less than the net advection term, during summer, it is in phase with it such that both terms give outflow and inflow peaks at the same time. During winter they are out of phase, the outflow peak of one occur at the same time as the inflow peak of the other. The overall average of term 2 gives a small inflow of 1.0±3.5‰m^3/s. Therefore, Stokes Drift is a significant process in Sake Shinji in opposing the advective flow, and its contribution to salinity flux is negligible.

Term 3 is also small with a maximum of ±352‰m^3/s. Its overall average is 11.6±23.9‰m^3/s. During summer, it is in phase with Term 1 such that both terms give outflow and inflow peaks at the same time. During winter they are out of phase, the outflow peak of one occur at the same time as the inflow peak of the other. Term 3 contributes about 2% of outflow salinity flux. Terms 4, and 5 are very small throughout the period. Although they show some distinct relationships to wind and atmospheric pressure, their magnitudes are insignificant with overall averages of less than 1‰m^3/s (Table 4-7).

4.5.1.4 Mean shear terms

For the analysis of shear terms (Terms 6 and 7), this study used method 2 which emphasises the vertical effects. Method 1 emphasises the transverse effects. Applying method 1 to term 6 gives the same as those of using method 2 applied to term 7.

The selection of method 2 over method 1 was based on the analysis of lake response and recommendations from previous studies (Dyer et al. 1992; Rattray & Dworski 1980). From 22 June to 13 July 2003, there were drastic fluctuations in bottom salinity, whose magnitudes were almost uniform across all the stations, except for the shallow areas. At this time the stratification across the stations was also almost uniform. Accordingly, it is possible that there was much more salt transfer on the vertical term than on the transverse term, making method 2 a more reasonable decomposition of the fluxes.

Term 6 responds to wind and atmospheric pressure events more than river discharge (Figure 4.19 and Figure 4.20). From 22 June to 13 July 2003, the negative flux shows that there was a net inflow of salt resulting from a low salinity water outflow on the left hand side, together with a high salinity water inflow on the right-hand side. Equal volumes of unequal salt contents were exchanged. Hence regardless of the overall decrease in salinity, salt was being drawn into the lake. There were large variations, which had maximum negative flux values associated with low atmospheric pressure and westerly winds. These fluxes were also associated with negative cross sectional mean velocity $\langle \bar{u} \rangle$. Salt outflow was associated with easterly winds.

Magnitudes for the mean vertical fluxes (Term 7) are four time those of the mean transverse fluxes (Term 6) and their trend is exactly the same (Figure 4.19 and Figure

4.20). During the river discharge, wind and atmospheric pressure events, large negative flux indicates a developed gravitational circulation which was drawing in saline water near the bottom, and discharging an equal volume of freshwater near the surface. This was evident when river discharge was about 100 m^3/s, e.g. around December 18, 2002, January 23 & 29, 2003. During the summer months of June and July, there was a strong oscillation indicating that the vertical shear between the surface and bottom layers varied significantly with wind. However, during a very large river discharge event e.g. around July 13, 2003, both the vertical and the transverse contributions was heavily suppressed (positive flux). A possible explanation is that the whole water column was moving in the same direction, out of Lake Shinji. During this event, the both gravitational circulation and transverse effects had ceased for about a week.

Generally, when the mean cross sectional velocity $\langle \bar{u} \rangle$ is large and positive stratification is enhanced. When $\langle \bar{u} \rangle$ is large and negative stratification is reduced as the surface layer salinity increases. Small mean velocity is generally associated with high stratification. This suggests that stratification is an important factor in the generation of mean shear salt fluxes, and may act as an amplifier of variations by separating the low and high salinity layers.

4.5.1.5 Tidal shear terms

The maximum effect of the tidal terms is most likely with the largest phase differences of the tidal oscillations of velocity and salinity between the two layers (Dyer et al. 1992). This is possible when there is separation of the surface brackish layer from the saline bottom layer through increased stratification. Large positive fluxes coincide with the time

of maximum stratification. It is observed that greatest negative fluxes and decrease in positive fluxes occurred when the stratification was diminishing, rather than when it was at its maximum. Hence once the stratification was established, the inflow oscillation fluxes diminished as the vertical mean circulation adjusted.

Term 8 fluxes are very low during both summer and winter periods (Figure 4.19 and Figure 4.20). During summer period, reasonable almost alternating inflow and outflow from June 20 to July 13, 2003. During winter period, the reasonable inflow and outflow fluxes are at least 5 times larger than those during summer. The largest outflow occurred around 25 December, 2002. Reasonable fluxes coincided with the time when the transverse mean shear fluxes are also large, either inflow or outflow.

Term 9 (Figure 4.19 and Figure 4.20). As detailed above, highest inflows happened when the stratification was fast diminishing. Highest outflows coincided with increased river discharge and strong stratification, especially during summer. During summer the oscillatory vertical shear inflow fluxes were smaller than those during winter. However, outflow fluxes were comparable. Oscillations are more pronounced during winter due to decreased river discharge. Generally, though there was considerable variation, this term carried the much of the dispersive salt out-flux (34%) and influx (16%). Terms 10 and 11 are negligible.

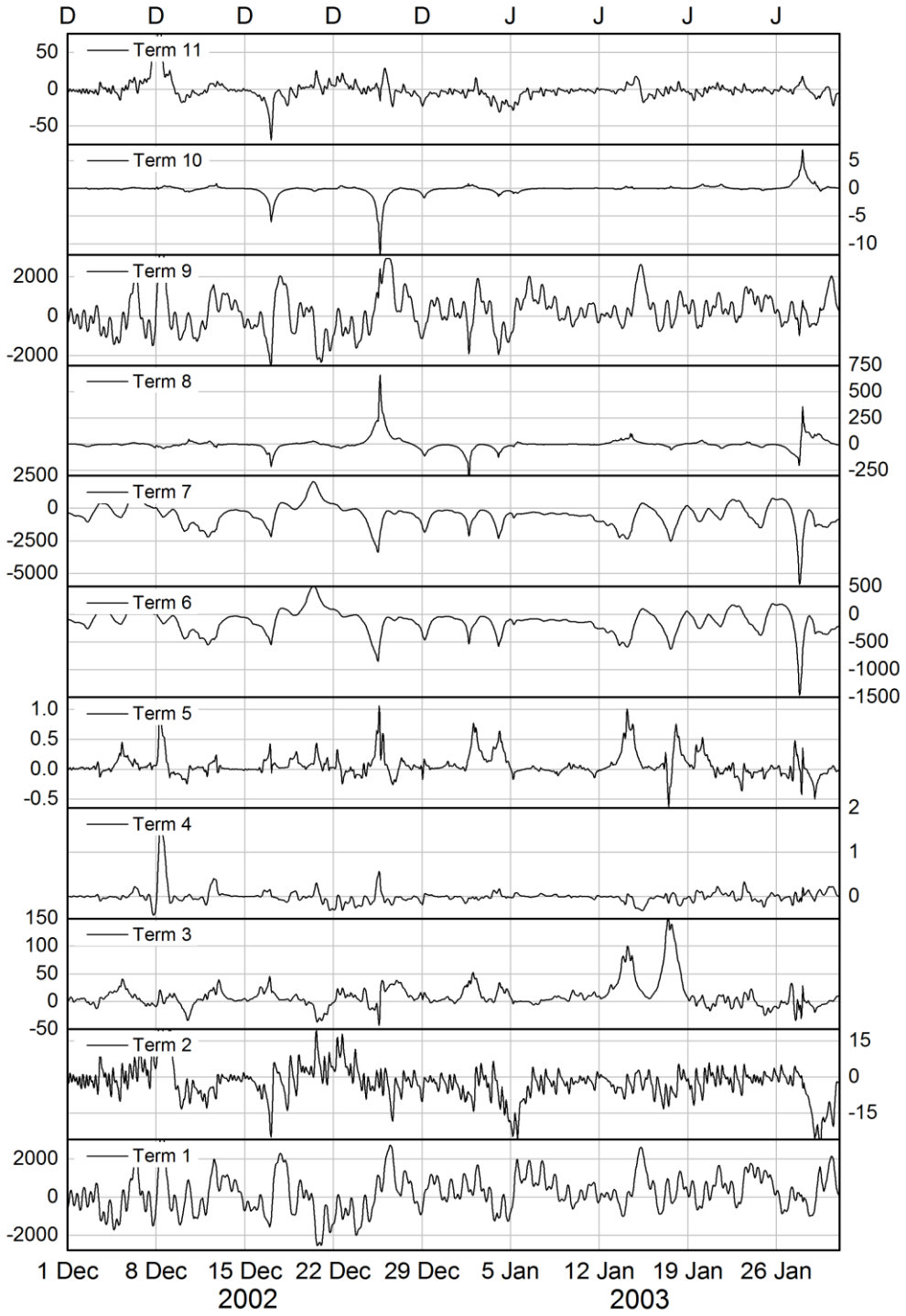

Figure 4.19 Cross sectional salinity flux (terms 1 – 11) for the winter period December 2002 – January 2003 in Lake Shinji

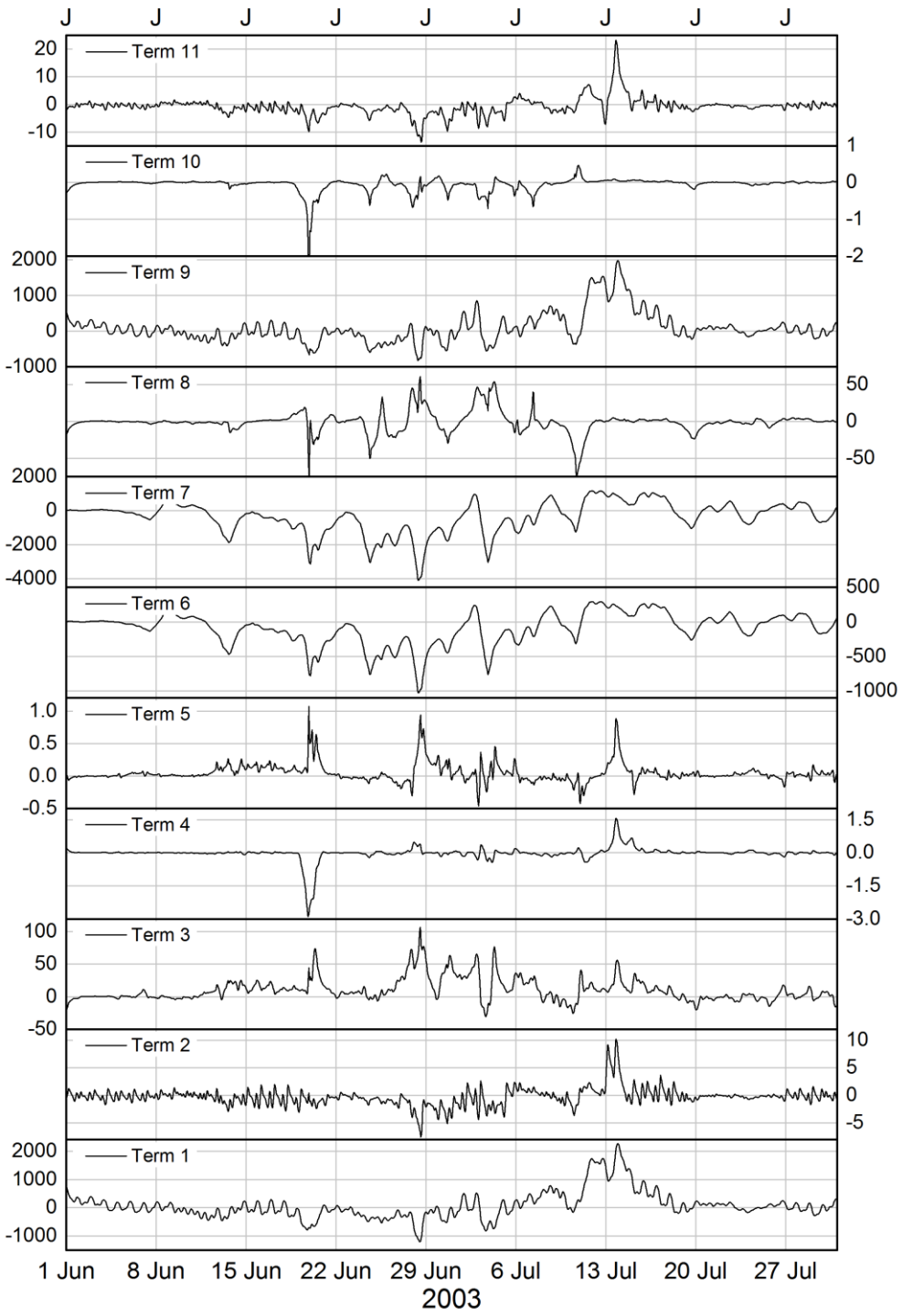

Figure 4.20 Cross sectional salinity flux (terms 1 – 11) for the summer period June – July 2003 in Lake Shinji

4.5.1.6 Dispersive salt flux

The total contribution of terms 6-9 define the dispersive upstream flux that, in a steady state situation, should balance the downstream flux due to the river discharge (Dyer et al. 1992). The sum of the dispersive terms is shown in Figure 4.21. The values show an overall dispersive inward flux of salt. During very large river discharge events when the lake is likely to be in an unsteady state, hence dispersive outward flux of salt dominates. Dispersive outward flux of salt also dominates when relatively strong easterly winds prevailed. When there are moderate river discharges (<200 m^3/s) and/or strong westerly winds, dispersive inward flux of salt dominates. During the January 27, 2003 discharge event (about 175 m^3/s) and strong westerly winds (>10 m/s), the inward dispersion peaked at 8000‰ m^3/s. Generally, dispersive flux of salt is higher during winter than during summer due to reduced river discharge in winter which promotes gravitational circulation.

The longitudinal gradient of mean salinity was calculated as the difference between depth averaged salinity at Matsue and cross sectional average of the section under review. The average longitudinal gradient of mean salinity was 7.7×10^{-4} psu/m. For the largest inward dispersion, this gives a value K_x of about 600 m^2/s.

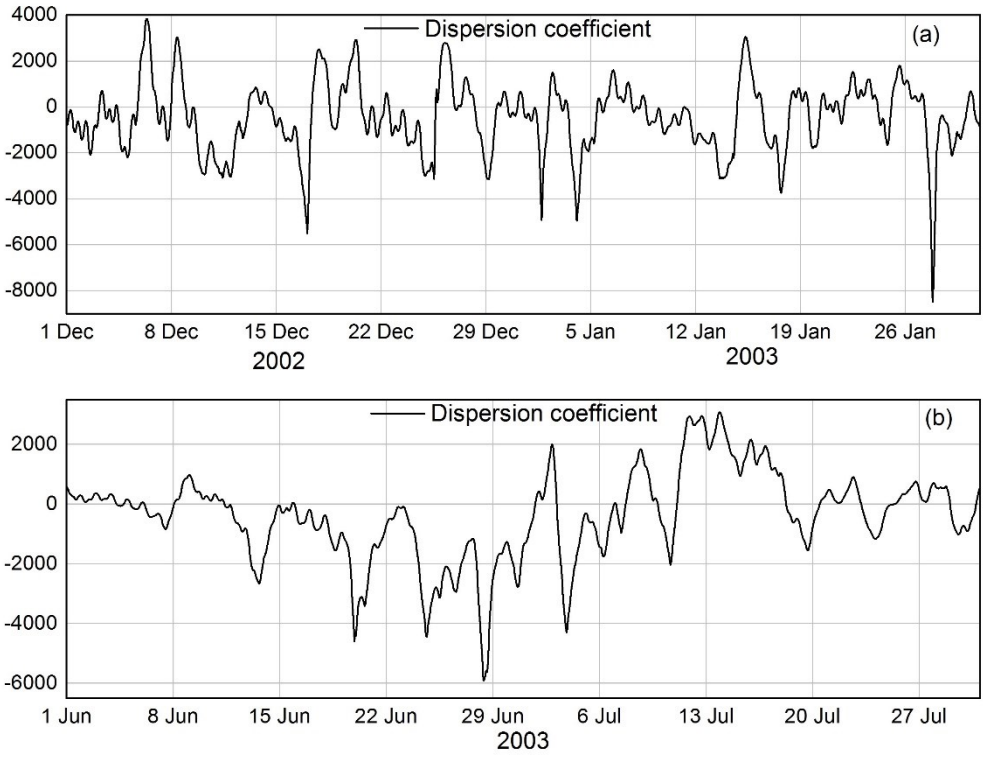

Figure 4.21 Time series of the dispersive upstream salt flux determined as the sum of Terms 6 to 9 for winter (a) and summer (b) in Lake Shinji

4.6 DISCUSSION

Analysis over the entire period reveals that the terms are not balance. The outward flux of salt averaged 91‰ m^3/s, and this is much less than the average inward flux of -522‰ m^3/s. Furthermore, the discharge of salt on the mean flow averaged 32‰ m3/s, and this is very small compared to the sum of the other terms with an average of -463‰ m3/s. This implies an overall increase of salinity within Lake Shinji.

The tidal oscillatory shear and the tidal mean shear effect have an interesting interaction with each other during discharge and wind variation events. The fluctuating cross sectional distributions of velocity and salinity results dynamic exchange between the

contributions by various terms. The first effect of the river discharge is apparent on every high river flow, the surface salinity decrease across the whole lake, and the bottom salinity increase. This change in salinity produced an outflow of salt associated with the vertical tidal oscillatory shear. From June 22 to July 10, 2003 there were abrupt fluctuations in bottom salinity in response to changing wind direction and speed. There were also abrupt changes in salinity in winter in response to increased river flow, e.g. December 17, 2002. At this stage the gravitational circulation responded, with a large inward flux of salt occurring on the vertical mean shear. The inward fluxes due to the mean shear terms was high except around July 13, 2003 when the inward fluxes by vertical mean shear was suppressed, and the fluxes effected by the vertical oscillatory term enhanced. This was due to very high river discharge of about 600 m^3/s. At this time there was a marked outflow associated with the vertical oscillatory shear term and mean shear terms. During this period the gravitational circulation had diminished until July 18, 2003 when the bottom salinity and subsequently stratification were reduced. Thus it appears that a very high river discharge event can stop bottom layer inflow and even reverse the flow direction. It takes about a week before the bottom layer salinity is diluted, mean shear terms adjust, and the vertical gravitational circulation develops. Generally, the river discharge and westerly winds increases the stratification. This results in surface and lower layers with different tidal variation phases, allowing a seaward oscillatory flux of salt. The phase difference is reduced by velocity shear between the two layers, resulting in mixing increasing the mean gravitational circulation.

As the river discharge weakens and/or easterly winds dominates, the gravitational circulation strength is reduced by the mixing. To ensure a seaward flux due to the

oscillatory vertical shear term, the phase differences need to increase. The decreased river discharge in winter enhances the contribution of the oscillatory vertical shear term, with vertical gravitational circulation mainly being destroyed by change in wind direction. Generally, in Lake Shinji de-stratification is abrupt and often associated with an abrupt reduction in gravitational circulation.

The mean velocities change dramatically throughout the winter period and mid-July 2003. This does not have a noticeable effect on the gravitational circulation (term 7), but in winter period and mid-July 2003 it appears to strengthen the vertical oscillation shear flux (term 9). Accordingly, it appears time is insufficient for the mean terms to respond to the oscillatory processes before they are reversed.

5 SUMMARY DISCUSSION

5.1 SUMMARY

Lake Shinji is identified as a valued fisheries ground especially for *Corbicula japonica* in the Shimane Prefecture, Japan, which suffers from salinity intrusion from the Japan Sea. Lakes Shinji and Nakaumi have been the focus of extensive data collection and modelling efforts aimed at understanding and developing ecosystem recovery scenarios to benefit shellfish farming. Previous studies have not computed salinity flux and qualified the extent to which each of the possible forcing mechanisms influence salt transport. To understand salinity intrusion processes and water circulation in Lakes Shinji and Nakaumi, this study investigated water exchange and salt transport at Nakaura Watergate, Lake Nakaumi and in Lake Shinji using observed salinity and meteorological data, and numerical model. The study attempted to address the mechanisms and variability of salt transport in coupled coastal lakes and implications for the mixing and circulation processes.

In Section 1, an analysis of water level and current measurements was done in an attempt to understand the mechanisms driving water exchange in Sakai Channel. Data measurements made at Nakaura Watergate was used in the analysis. Water level controlled tidal flows and the ebbing currents dominated the flows in Sakai Channel. Subtidal flows were mainly stratified indicating the effect of density gradients. Unidirectional flows sometimes occur coinciding with increased river discharge. Freshwater discharge or residual velocity transport almost all salt out of Lake Nakaumi and a significant quantity into the lake. Gravitational circulation, bathymetric tidal

pumping, steady wind effect is responsible for more than half of the salt being transported into Lake Nakaumi.

Section 3 analysed the dynamic characteristics of seawater intrusion using wavelet analysis. Salinity flux at Nakaura Watergate was analysed. Effects of river discharge, tide level, and meteorological forcing variables makes the seawater intrusion non-linear. To account for the non-linear characteristics, partial wavelet coherence (PWC) was used to analyse the impact of river discharge, tide level, and meteorological forcing variables on salinity flux after controlling the effect of all other forcing variables. PWC results show that tide level has impact on salinity flux over short cycles (limited to less than 4 days) throughout the analysis period with an average time lag of about 2 days. This suggests that astronomical tides are the dominant factor in the salinity intrusion processes. The river discharge largely influences salinity flux over medium cycles (5~16 days) during the months of June and July with an average time lag of 0.3 days. Atmospheric pressure occasional affect tide level, indirectly driving salinity transport. The study findings provide guidance for factors affecting salinity intrusion processes and further research.

An application of 3D hydrodynamics model to study salt flux and mixing was done in Section 4. The model demonstrated to be robust under wide variety of forcing, e.g., tides, hydrology, density currents, and wind. However, the salinity simulation results were not quite in agreement with observed results. The simulation results can be improved applying spatially varying friction coefficients, diffusivity coefficients and meteorological forcing in the grid domain to match the observed characteristics of the lakes.

Model results were then used to study the characteristics of water, and salt transport. The section examined the primary mechanisms that drive water, and salt transport within Lakes Shinji and Nakaumi, between Lake Shinji and Lake Nakaumi and between Lake Nakaumi and Miho Bay. Increase in stratification produces an outflow of salt associated with the vertical tidal oscillatory shear (mean rate of 48‰m^3/s). Huge river discharge suppresses vertical mean shear and gravitational circulation diminishes, resulting in a total salt outflow of about 5000‰m^3/s in around July 13. Tidal influence of salt flux is greater in winter. There is a net influx of salt at a mean rate of 431‰m^3/s. Gravitational circulation strengthen on moderate river flows or westerly winds.

The results of the research reveals that river discharge, wind and atmospheric pressure are all important forcing mechanisms for circulation in Lakes Shinji and Nakaumi. River discharges of at least 100 m^3/s have a positive impact on outward flux of salt at Nakaura but promotes influx into Lake Shinji. Westerly winds of at least 5 m/s and pressure drop of about 10 hPa promotes overall influx of salt. Generally, the peaks of river flow, wind and atm. pressure coincide with each other and wavelet analysis can be used to determine the most significant forcing mechanism at any given time. Optimisation simulations are necessary to establish river discharges which will counter the negative effects westerly winds and atmospheric pressure drop, to maintain favourable salinity levels.

5.2 IMPLICATIONS OF THE STUDY

It is important to optimal salinity levels in Lake Shinji for the development and survival of *Corbicula japonica*. High salinity leads to the depletion of oxygen, release of

hydrogen sulphide which results in the death of shellfish. Almost zero salinity and high salinity levels inhibits spawning of *Corbicula japonica*. On the other hand, low salinity levels affect larva development. The model study results reveal that westerly winds and atmospheric pressure drop leads to salt transport into Lake Shinji, increasing salinity levels. This phenomenon is bad for the shellfish if it is not countered by a substantial river discharge. Countering the negative meteorological effects with timely upstream water release may help maintain optimal salinity levels. A large river discharge causes the salinity to become too low for the *Corbicula japonica* reproduction. After a large river discharge, westerly winds and atmospheric pressure drop can help mitigate the effects of low salinity.

The analytical methods and numerical simulation used in this study, and the results can be applied to other locations where the recovery of the coastal lake ecosystems is dependent on the hydrological and meteorological conditions. The prevailing wind has influence on the salt transport in and out a coastal lake. If the prevailing wind is along the length of the lake (fetch), it can promote influx or outward flux of salt. For Lake Shinji, the length of the is from west (landside) to east (seaside) and westerly winds prevails. The westerly winds promote salinity intrusion into Lake Shinji. The westerly winds push the surface water to the east resulting in dense water intruding into Lake Shinji along the bottom.

Future efforts to understand the biogeochemical response to physical processes in Lakes Shinji and Nakaumi, there is need for coupled hydrodynamic, water quality and ecological model combined with optimisation model. Thus, the next step in the study processes in these two lakes is to employ a simulation model with optimisation

capabilities. Combined simulation-optimisation model can be used to determine discharge rates to help maintain optimal salinity levels in the two lakes especially, Lake Shinji.

REFERENCES

Aguiar-Conraria, L. & Soares, M.J., 2014. The continuous wavelet transform: Moving beyond uni- and bivariate analysis. *Journal of Economic Surveys*, 28(2), pp.344–375.

Amsden, A.A. & Harlow, F.H., 1970. A simplified MAC technique for incompressible fluid flow calculations. *Journal of Computational Physics*, 6(2), pp.322–325.

Baba, K., 2006. Ecological study on spawning and early life stage of the brackish water bivalve Corbicula japonica in Lake Abashiri. *Scientific Reports of Hokkaido Fisheries Experimental Station*, 71, pp.1–41.

Baba, K. et al., 1999. Effects of temperature and salinity on spawning of the brackish water bivalve Corbicula japonica. *Marine Ecology Progress Series*, 180, pp.213–221.

Briciu, A.-E., 2014. Wavelet analysis of lunar semidiurnal tidal influence on selected inland rivers across the globe. *Scientific reports*, 4, p.4193.

Dyer, K.R., 1974. The salt balance in stratified estuaries. *Estuarine and Coastal Marine Science*, 2(3), pp.273–281.

Dyer, K.R., Gong, W.K. & Ong, J.E., 1992. The cross sectional salt balance in a tropical estuary during a lunar tide and a discharge event. *Estuarine, Coastal and Shelf Science*, 34(6), pp.579–591.

Fujii, T. & Okuda, S., 2004. The Relationship between Internal Waves and the Movement of Anoxic Water in two Connected Brackish Water Bodies – Lake Nakaumi and the Ohashi River. In *International Seminar on Restoration of Damaged Lagoon Environments*. Matsue, Japan, p. 1.

Grinsted, A., Moore, J.C. & Jevrejeva, S., 2004. Application of the cross wavelet transform and wavelet coherence to geophysical time series. *Nonlinear processes in geophysics*, 11(5/6), pp.561–566.

Hansen, D. V, 1965. Currents and mixing in the Columbia River estuary. *Ocean Science and Ocean Engineering*, 2, pp.943–955.

Hiratsuka, J., Yamamuro, M. & Ishitobi, Y., 2007. Long-term change in water transparency before and after the loss of eelgrass beds in an estuarine lagoon , Lake Nakaumi , Japan. *Limnology*, 8(1), pp.53–58.

Honda, T. & Mitsuyasu, T., 1980. 水面に及ぼす風の作用に関する実験的研究. 海岸工学講演会論文集, 27, pp.90–93.

Hughes, F.W., 1968. *Salt flux and mixing processes in the Columbia River estuary during high discharge.* M.S. thesis. Seattle: University of Washington.

Hughes, F.W. & Rattray, M., 1980. Salt flux and mixing in the Columbia River Estuary. *Estuarine and Coastal Marine Science*, 10(5), pp.479–493.

Hunkins, K., 1981. Salt Dispersion in the Hudson Estuary. *Journal of Physical Oceanography*, 11(5), pp.729–738.

Ichikawa, T., Aizaki, M. & Takeshita, M., 2007. Numerical study on amelioration of water quality in Lakes Shinji and Nakaumi: a coastal brackish lagoon system. *Limnology*, 8(3), pp.281–294.

Ideião, S.M.A. & Santos, C.A.G., 2005. Analysis of precipitation time series using the wavelet transform. *Sociedade & Natureza, Uberlandia*, (Special Issue), pp.736–745.

Kajishima, T., 1999. 乱流の数値シミュレーション, 養賢堂.

Kim, C.K. & Park, K., 2012. A modeling study of water and salt exchange for a micro-tidal, stratified northern Gulf of Mexico estuary. *Journal of Marine Systems*, 96–97, pp.103–115.

Kishi, M.J., 2000. Coastal lagoon ecosystems: a case study in lakes Nakaumi and Shinji, Japan. *Journal of Marine Systems*, 26(2), pp.115–116.

Klinger, B.A., Density of Seawater. , p.4. Available at: http://mason.gmu.edu/~bklinger/seawater.pdf.

Kobayashi, T. ed., 2003. *Handbook of Numerical Fluid Dynamics*, Maruzen.

Kondō, J., 1994. 水環境の気象学, 朝倉書店.

Kurokawa, T. & Fukuoka, S., 2003. Flow and Water Quality Change in Brackish Lake Depending On the Change in Meteorological Conditions. In J. Ganoulis & P. Prinos, eds. *Proceedings of the 30th Congress of IAHR*. Thessaloniki, Greece, pp. 77–84.

Lessa, G. & Masselink, G., 1995. Morphodynamic evolution of a macrotidal barrier estuary. *Marine Geology*, 129, pp.25–46.

Liu, B. et al., 2014. Wavelet analysis of the dynamic characteristics of saltwater intrusion – A case study in the Pearl River Estuary of China. *Ocean & Coastal Management*, 95, pp.81–92.

Mizoyama, I., Ohya, Y. & Fukuoka, S., 2011. Flow Mechanism in a Connected Brackish Lake and Numerical Flow Computation over a Long Period. *Journal of Japan Society of Civil Engineers, Ser. B1 (Hydraulic Engineering)*, 67(3), pp.101–120.

Moser, G.A.O. et al., 2005. Instantaneous Transport of Salt, Nutrients, Suspended Matter and Chlorophyll-a in the Tropical Estuarine System of Santos. *Brazilian Journal of Oceanography*, 53 (3/4), pp.115–127.

Munk, W.H. & Anderson, E.R., 1948. Notes on a theory of the thermocline. *Journal of Marine Research*, 7(3), pp.276–295.

Nakamura, Y. et al., 1997. Diurnal cycle of water temperature and water quality in a littoral zone of a eutrophic lake. *Hydraulic Engineering*, 41, pp.469–474.

Nakamura, Y. & Kerciku, F., 2000. Effects of filter-feeding bivalves on the distribution of water quality and nutrient cycling in a eutrophic coastal lagoon. *Journal of Marine Systems*, 26(2), pp.209–221.

Nakata, K., Horiguchi, F. & Yamamuro, M., 2000. Model study of Lakes Shinji and Nakaumi – a coupled coastal lagoon system. *Journal of Marine Systems*, 26(2), pp.145–169.

Nakatsuji, K., Huh, J.-Y. & Murota, A., 1991. Numerical experiments of three-dimensional buoyant surface discharges. *Doboku Gakkai Ronbunshu*, (434), pp.19–28.

Nakatsuji, K., Karino, S. & Kurita, H., 1992. Finite Element Analysis of Tidal Flow in the Osaka Bay with Subgrid Scale Eddy Coefficient. In *PROCEEDINGS OF HYDRAULIC ENGINEERING*. pp. 693–696.

National Astronomical Observatory ed., 2000. *2000 Chronological Scientific Tables (desktop version)*, Maruzen.

Ng, E.K.W. & Chan, J.C.L., 2012. Geophysical applications of partial wavelet coherence and multiple wavelet coherence. *Journal of Atmospheric and Oceanic Technology*, 29(12), pp.1845–1853.

Nidzieko, N.J., 2010. Tidal asymmetry in estuaries with mixed semidiurnal/diurnal tides. *Journal of Geophysical Research: Oceans*, 115(8), pp.1–13.

Ninomiya, S. et al., 1997. AMeDASのデータを用いた時刻別日射量の推定法 第2報 一回転式日照計および改良型太陽電池式日照計への適用. 空気調和・衛生工学論文集, 65, pp.53–65.

Ninomiya, S., Akasaka, H. & Matsuo, Y., 1996. AMeDASのデータを用いた時刻別大気放射量の推定法. 空気調和・衛生工学論文集, 60, pp.133–144.

Nobuyuki Tamai, 1980. 密度流の水理, 技報堂出版.

Nomura, R. et al., 2004. PB-02 Acoustic signals of the aquatic environment of Lake

Nakaumi. In *International Seminar on Restoration of Damaged Lagoon Environments*. Matsue, Japan, p. 1.

Okuda, S., 2004. Water movement and physical environments in brackish lakes - Shinjiko and Nakaumi. In *International Seminar on Restoration of Damaged Lagoon Environments*. Matsue, Japan, pp. 1–6.

Onuma, M. et al., 2006. 舗装温度計測サイトの観測データを用いた大気放射モデルの検証. 土木学会舗装工学論文集, 11, pp.59–66.

PARI, Ise Bay simulator. Available at: http://www.pari.go.jp/unit/kaikj/is/.

Parmar, K.S. & Bhardwaj, R., 2013. Wavelet and statistical analysis of river water quality parameters. *Applied Mathematics and Computation*, 219(20), pp.10172–10182.

Pawlowicz, R., Beardsley, B. & Lentz, S., 2002. Classical tidal harmonic analysis including error estimates in MATLAB using TDE. *Computers and Geosciences*, 28(8), pp.929–937.

Pereira, M.A.G. & Lessa, G.C., 2009. Varying Patterns of water circulation in Canal de Cotegipe, Baía de Todos os Santos. *Revista Brasileira de Geofísica*, 27(1), pp.103–119.

Rattray, M. & Dworski, J.G., 1980. Comparison of methods for analysis of the transverse and vertical circulation contributions to the longitudinal advective salt flux in estuaries. *Estuarine and Coastal Marine Science*, 11(5), pp.515–536.

Sakai, S. et al., 2012. Hydrogen sulfide and organic carbon at the sediment–water interface in coastal brackish Lake Nakaumi, SW Japan. *Environmental Earth Sciences*, 68(7), pp.1999–2006.

Sakai, S., Nakaya, M. & Takayasu, K., 2004. Hydrogen sulfide distribution in bottom and pore waters during an anoxic period in Lake Nakaumi , Japan. *LAGUNA（Research for Coastal Lagoon Environments）*, 11, pp.65–68.

Sato, K., Matsuoka, M. & Kobayashi, K., 1993. Efficient 3 dimensional flow calculation method and its applicability. *Proceedings of Coastal Engineering, JSCE*, 40, pp.221–225.

Seigel, M.T., 2012. Consensus building revisited: The Experience and Approach of Toshio Kuwako. *Centre for Dialogue Working Paper Series*, (2012/2), p.54.

Shimazaki, G., Riku, M. & Hayakawa, N., 1996. AMeDAS日照時間データを用いた総合的な時間日射量推定手法. *水文・水資源学会1996年研究発表会要旨集*, pp.108–109.

Shinjiko Fisheries Cooperative Association, Fishing industry in Lake Shinji. Available at: http://shinjiko.jp/publics/index/8/ [Accessed February 27, 2017].

Smagorinsky, J., 1963. General Circulation Experiments With the Primitive Equations. *Monthly Weather Review*, 91(3), pp.99–164.

Somoza, R.D. et al., 2013. A water level relationship between consecutive gauge stations along Solimoes/Amazonas main channel: a wavelet approach.

Sousa, R.M.D. de, 2014. *Carbon Prices. Dynamic analysis of European and Californian markets*. Doctoral Dissertation. Maio: Universidade Nova de Lisboa.

Sovi, A. et al., 2012. Wavelet analysis of hydrological signals on an example of the River Sava. In *MIPRO, 2012 Proceedings of the 35th International Convention*. Opatija, Croatia: IEEE, pp. 1223–1228.

Torrence, C. & Compo, G.P., 1998. A Practical Guide to Wavelet Analysis. *Bulletin of the American Meteorological Society*, 79(1), pp.61–78.

Uncles, R.J., Ong, J.E. & Gong, W.K., 1990. Observations and analysis of a stratification-destratification event in a tropical estuary. *Estuarine, Coastal and Shelf Science*, 31(5), pp.651–665.

Uye, S. et al., 2000. Geographical and seasonal variations in mesozooplankton abundance and biomass in relation to environmental parameters in Lake Shinji–Ohashi River–Lake Nakaumi brackish-water system, Japan. *Journal of Marine Systems*, 26(2), pp.193–207.

Vaz, N., Lencart e Silva, J.D. & Dias, J.M., 2012. Salt Fluxes in a Complex River Mouth System of Portugal J. Kurths, ed. *PLoS ONE*, 7(10), p.e47349.

Webb, E.K., 1970. Profile relationships: The log-linear range, and extension to strong stability. *Quarterly Journal of the Royal Meteorological Society*, 96(407), pp.67–90.

Yamamuro, M. et al., 2006. Ecosystem Shift Resulting from Loss of Eelgrass and Other Submerged Aquatic Vegetation in Two Estuarine Lagoons , Lake Nakaumi and Lake Shinji , Japan. *Journal of Oceanography*, 62(4), pp.551–558.

Yamamuro, M., Kamiya, H. & Ishitobi, Y., 2011. Relationship between Hypoxia Due to Stratification and COD (Mn) at Brackish Lagoon, Lake Shinji. *Journal of Japan Society on Water Environment*, 34(4), pp.57–64.

Yamamuro, M. & Koike, I., 1994. Diel changes of nitrogen species in surface and overlying water of an estuarine lake in summer : Evidence for benthic-pelagic coupling. *Limnology and Oceanography*, 39(7), pp.1726–1733.

Yamamuro, M. & Koike, I., 1993. Nitrogen metabolism of the filter-feeding bivalve

Corbicula japonica and its significance in primary production of a brackish lake in Japan. *Limnology and Oceanography*, 38(5), pp.997–1007.

Yamamuro, M., Nakamura, M. & Nishimura, M., 1990. A method for detecting and identifying the lethal environmental factor on a dominant macrobenthos and its application to Lake Shinji, Japan. *Marine Biology*, 107(3), pp.479–483.

Zhang, Q., Xu, C.-Y. & Chen, Y.D., 2009. Wavelet-based characterization of water level behaviors in the Pearl River estuary, China. *Stochastic Environmental Research and Risk Assessment*, 24(1), pp.81–92.